Tobias Tänzer, B.Sc.

Efficient Implementation and Analysis of Different Phase Noise Generation Methods for DVB-S2X Waveforms

MASTER'S THESIS

to achieve the university degree of

Diplom-Ingenieur

Master's degree programme: Space Sciences and Earth from Space

submitted to

Graz University of Technology

Supervisor

Assoc.Prof. Dipl.-Ing. Dr.techn. Wilfried Gappmair

Institute of Communication Networks and Satellite Communications

Dipl.-Ing. Harald Schlemmer
JOANNEUM RESEARCH

Graz, September 2018

AFFIDAVIT

I declare that I have authored this thesis independently, that I have not used other than the declared sources/resources, and that I have explicitly indicated all material which has been quoted either literally or by content from the sources used. The text document uploaded to TUGRAZonline is identical to the present master's thesis.

_____
Date

_____
Signature

I. Acknowledgements

I would like to express my gratitude to JOANNEUM RESEARCH's Digital branch, especially to my supervisor DI Harald Schlemmer for the practical guidance in using and improving the existing simulation environment, the constructive discussions of research topics and results and the feedback on the contents of the thesis. Further, I would like to thank Dr. Johannes Ebert for the introduction to the subject and continued assistance, and the rest of the satellite communications work group, especially Dr. Michael Schönhuber, for their support throughout the creation of this thesis.

On the side of TU Graz, my gratitude goes to Assoc.Prof. Wilfried Gappmair for the introduction to the topic and establishment of ties with the aforementioned individuals, the feedback and support on theoretical topics throughout the creation of this thesis, and the helpful advice in formal matters.

II. Abstract

This thesis explores the impairment of phase noise (PN) in its statistical and spectral properties as well as its influence on different waveforms in the context of the Digital Video Broadcasting – Second Generation Extended (DVB-S2X) standard.

A PN generation method based on the Inverse Fast Fourier Transform (IFFT) is the focal point of the present thesis.

Four different application cases of DVB-S2X are taken into account via different PN masks. The first of these is a Direct-to-Home broadcast scenario, where PN of critical levels is induced into the system from mass-produced low noise blocks at the receiver. The second scenario is an interactive link using a very small aperture terminal (VSAT), e.g. internet access in remote regions via satellite. Furthermore, the PN contribution of an on-board satellite transponder is regarded, as well as the PN contribution that is expected in precoding or multiple-spot beam scenarios of modern satellites.

Methods to analyze the PN impairment are presented and subsequently applied to the simulation. The first of these is a statistical analysis of the raw PN samples in the time domain. Secondly, a spectral analysis in the frequency domain through a Fast-Fourier Transform (FFT) using a PN impaired sine waveform is performed and compared to the corresponding phase noise mask. Thirdly, the performance of a Viterbi-Viterbi phase tracker is shown in the case of PN-affected modulated signals. Finally, the frame error rate (FER) of several DVB-S2X waveforms impaired by different levels of PN is simulated. The impact of different frequencies specified in the PN masks on the FER results is highlighted in particular, showing that small differences in PN masks can lead to performance gains or losses in the range of several dB with respect to the FER curve.

Furthermore, a comparison between different PN creation methods is presented in terms of their computational complexity, result accuracy, and application cases. In order to do that, the newly implemented IFFT-based PN generation method is compared to an already existing method based on creating PN samples with subsequent filter banks of low-pass infinite impulse response (IIR) filters and up-sampling filters. It is concluded that the IFFT-based PN generation method yields more desirable results in simulations with a high-performance simulation environment such as the one used in this thesis. However, the filter-based method lends itself more readily to an implementation in hardware if limited computational resources are available.

III. Zusammenfassung

Diese Masterarbeit analysiert die Beeinträchtigung, die durch Phasenrauschen verursacht wird, in Form seiner statistischen und spektralen Eigenschaften. Weiterhin wird der Einfluss, den Phasenrauschen auf ein modernes Kommunikationssystem ausübt, anhand des Digital Video Broadcasting – Second Generation Extended (DVB-S2X)-Standards quantifiziert.

Der Schwerpunkt der vorliegenden Arbeit liegt auf der Implementierung einer Methode, die die Inverse Fast Fourier Transformation (IFFT) nutzt, um unter Zuhilfenahme einer Rauschmaske einen zufälligen Phasenrausch-Prozess zu erzeugen.

Vier verschiedene Anwendungsszenarien werden in Form verschiedener Phasenrausch-Masken berücksichtigt. Das erste Szenario ist ein Direct-to-Home (DTH) Rundfunk-Szenario, bei dem durch den Einfluss von massenproduzierten Komponenten im rauscharmen Signalumsetzer (LNB) des Empfängers ein kritisches Phasenrauschen erzeugt wird. Der zweite Anwendungsfall ist eine interaktive Übertragung mit Hilfe von Very Small Aperture Terminals (VSAT), wie zum Beispiel eine Internetverbindung in einer abgelegenen Region über Satellit. Weiterhin wird der Einfluss von Phasenrauschen, das in einzelnen Komponenten der Übertragungskette erzeugt wird, analysiert, indem der Transponder des Kommunikationssatelliten näher betrachtet wird. Außerdem wird das Phasenrauschen für Multibeam-Szenarien in Form einer Maske diskutiert.

Die Analysewerkzeuge für die Betrachtung von Phasenrauschen werden präsentiert und im Folgenden auf die Simulationen angewandt. Sie umfassen erstens im Zeitbereich eine statistische Analyse der Rohwerte des Phasenrauschens ohne den Einfluss eines Trägers. Zweitens wird der Frequenzbereich untersucht, wo durch eine FFT das Phasenrauschen auf einem reinen Sinus-Träger mit der Rauschmaske verglichen wird. Drittens wird ein Viterbi-Viterbi Phasenschätzer auf seine Leistungsfähigkeit dahingehend untersucht, dem verrauschten modulierten Signal zu folgen und so den Einfluss des Phasenrauschens zu minimieren. Als letztes werden die Frame Error Raten (FER) von verschiedenen DVB-S2X-Signalen unter Einfluss von verschiedenen Phasenrausch-Szenarien untersucht. Der Einfluss der verschiedenen Frequenzen in Rauschmasken auf die FER wird aufgezeigt. Speziell wird der Umstand thematisiert, dass kleine Änderungen der Rauschmasken großen Einfluss im Rahmen mehrerer dB auf der FER-Kurve und somit auf die Leistungsfähigkeit des Systems haben.

Ein weiterer Schwerpunkt der Arbeit liegt im Vergleich zwischen zwei verschiedenen Methoden zur Erzeugung von Phasenrauschen, vor allem im Hinblick auf die Komplexität der Berechnung, die Genauigkeit der Resultate und mögliche Anwendungsfälle. Um das zu erreichen, wird die neu implementierte IFFT-basierte Methode mit einer schon existierenden Filter-basierenden Methode verglichen, bei der das Phasenrauschen mit mehreren Filterbänken von Tiefpass-Filtern mit unendlicher Impulsantwort (IIR) und Upsampling-Filtern erzeugt wird. Dabei zeigt sich, dass die IFFT-basierte Methode die besseren Resultate liefert, insofern eine ausreichend performante Simulationsumgebung verwendet wird. Die Filter-basierte Methode hingegen ist eher geeignet, wenn eine Hardware-Implementierung mit begrenzten Berechnungsressourcen benötigt wird.

IV. Table of Contents

V.   List of Figures

VI. List of Tables

VII. Acronyms

APSK .... Amplitude and Phase Shift Keying
AWGN .... Additive White Gaussian Noise
BCH .... Bose–Chaudhuri–Hocquenghem code
BPSK .... Binary Phase Shift Keying
CCDF .... Complementary Cumulative Distribution Function
CDF .... Cumulative Distribution Function
CIC .... Cascaded Integrator-Comb
CSR .... Cycle Slip Rate
dBc .... Decibels relative to the Carrier
DFT... Discrete Fourier Transform
DTH .... Direct-to-Home
DVB-S... Digital Video Broadcasting via Satellite
DVB-S2X .... Digital Video Broadcasting via Satellite - 2nd Generation Extended
ESA .... European Space Agency
FER .... Frame Error Rate
FFT .... Fast Fourier Transform
FIR... Finite Impulse Response
FPGA.. Field-Programmable Gate Array
I/Q.. In-Phase/Quadrature components
IFFT .... Inverse Fast Fourier Transform
IIR.. Infinite Impulse Response
IPP... Intel® Integrated Performance Primitives
LDPC .... Low Density Parity Check codes
LNB... Low Noise Block
MODCOD .... Modulation and Coding Scheme
NDA .... Non-Data-Aided
PDF .... Probability Density Function
PLL .... Phase-Locked Loop
PLS... Physical Layer Signalling
PMF .... Probability Mass Function
PN.. Phase Noise
PSD .... Power Spectral Density
QPSK... Quadrature Phase Shift Keying
RF.. Radio Frequency
RRCos .... Root-Raised Cosine
RX.. Receiver
SER .... Symbol Error Rate
SNR .... Signal-to-Noise Ratio
SOS.. Second-Order Sections
TX... Transmitter
V&V .... Viterbi & Viterbi Phase Tracker
VSAT .... Very Small Aperture Terminal

1. Introduction

In a *Digital Video Broadcasting via Satellite* (DVB-S) environment, efficient system usage is of high priority due to the cost of the geosynchronous satellites involved. As demands for throughput rise due to innovations in television such as 4K and even higher resolutions, a continuous increase in bandwidth is required to satisfy those demands. At the same time, due to the sparsity of spectral resources in the K_a and K_u band, more and more satellite applications are required to migrate to higher frequency bands such as Q, V, and W band with carrier frequencies of up to 70 GHz. These two developments combined lead to a multitude of challenges that have to be overcome for a digital transmission system to operate efficiently.

The *Digital Video Broadcasting via Satellite - Second Generation Extended* (DVB-S2X) standard is being developed to overhaul DVB-S for current and future demands of both the *Direct-to-Home* (DTH) and interactive markets using a *Very Small Aperture Terminal* (VSAT). In order to develop a new standard such as DVB-S2X in an economical fashion, extensive simulations are required before implementations in hardware can be realized for testing. It is of utmost importance that these simulations portray realistic conditions, which means that impairments to the signal have to be carefully considered and implemented to reflect their real characteristics as closely as possible. On the other hand, in order for simulations to be effective, computational efficiency has to be taken into account. This results in a tradeoff between simulation accuracy and efficiency and calls for the simulation environment and implementation of methods to be highly efficient in order to allow for an accurate simulation for a sufficient number of data points within an acceptable time frame.

One of the important impairments in a high-throughput communications application that becomes more and more problematic as higher frequency bands such as Q, V, and W band are utilized, is *Phase Noise* (PN). This sort of impairment is introduced into an electrical system through the non-ideal properties of up- and downconverters and their components, mainly oscillators and *Phase-Locked Loops* (PLLs), which can be found in *transmitter* (TX), transponder and *receiver* (RX) blocks within the transmission chain of DVB-S2X. It manifests as phase instability at the oscillator frequency that affects the mixing stage in the converter and leads to a phase jitter that is especially severe in phase-modulated signals such as *Quadrature Phase Shift Keying* (QPSK). As opposed to *Additive White Gaussian Noise* (AWGN), this impairment is not easily addressable by averaging due to its random walk-like properties.

Commonly, phase noise has been described using simple models to simulate this kind of impairment, which are insufficient to satisfy the requirements for a detailed simulation of the DVB-S2X system. Therefore, two methods to create PN samples of the required accuracy are presented in the following, one based on using filter banks to shape AWGN according to a PN mask, the other using a multiplication of AWGN samples in the frequency domain with a PN mask and a subsequent *Inverse Fast Fourier Transform* (IFFT) to create time-domain PN samples. While the filter-based method had already been implemented and only needs verification and testing, a second independent alternative is needed due to the lack of literature available to verify results. Therefore, the IFFT-based method is implemented in a highly efficient C++ simulation environment to ensure that a variety of different analysis methods for both the raw PN samples as well as modulated DVB-S2X signal structures can be simulated and the methods can be compared and thereby verified.

The phase noise masks necessary to create PN samples are taken from the DVB-S2X standards [1], [2] and represent the expected equipment used for both DTH and interactive DVB-S2X applications in reality.

The main contribution for phase noise in the DVB-S2X system for the DTH case comes from the downconverter in the *Low Noise Block* (LNB) of the receiver. As the equipment used in mass-produced LNBs has to be cost-effective and available in large numbers compared to the TX ground station equipment and onboard satellite equipment, it is reasonable to assume a low quality, which in turn means that the largest contribution of phase noise will originate from this module. In [2], several PN masks are defined for TX, satellite, and RX for different frequency bands (K_u and K_a band) and equipment (state-of-the-art and older). Aggregate PN masks that combine the influence of all three sources are also recommended, which will be looked at in further detail in the next section.

For the case of VSAT links for news gathering, disaster relief and similar ad hoc situations [2] as well as IP traffic that require an interactive link instead of a broadcast scenario, the PN characteristics change. The equipment involved in the link is now a dedicated VSAT that can be reasonably expected to use higher-quality equipment than the average LNB, especially because it is used as a TX station for the return link and therefore required to fulfill certain conditions in terms of frequency stability in order to be functional. For this scenario, [2] provides a new set of PN masks detailing individual and aggregate contributions of phase noise across all involved equipment, where once again different frequency bands (K_u and K_a band) as well as different types of equipment (state-of-the-art and older) are suggested. Due to the relative difference in quality of electrical parts used between the DTH and the VSAT usage scenarios, it is obvious that the overall phase noise contribution in the VSAT case is lower than in the DTH case.

The remainder of this thesis is organized as follows:

In Chapter 2, the theoretical processes that describe phase noise are given, the analysis methods used within the thesis are described, and the PN masks that are used for simulations as well as their use cases are presented.

In Chapter 3, both the filter-based and the IFFT-based PN generation method are described in detail and compared with each other in terms of their advantages and drawbacks.

Chapter 4 covers the implementation of the PN generation methods in the C++ simulation environment and shows an analysis of the computational performance of either method.

Chapter 5 is dedicated to the simulation results for statistical and spectral analysis of the PN samples created using the IFFT-based method, a comparison of results for both PN generation methods as well as an analysis of modulated signals impaired by PN.

Chapter 6 concludes the thesis with a summary of the findings.

2. Phase Noise Characterization

In order to characterize phase noise, its theoretical fundamentals have to be regarded first.

As described in the introduction, phase noise mainly originates in the up- and downconverters between carrier frequencies that are necessary along the transmission path. Its intensity is inversely related to the quality of the equipment used, which comprises oscillators and PLLs. A theoretical representation of the definitions of the phase noise produced in an oscillator needs to be established in this chapter.

Additionally, methods are needed that allow for a digital analysis of the random phase noise process as well as its spectrum. An analysis of the time-domain PN process yields its statistical properties, which are necessary to give a deeper insight into the random process behind phase noise. The spectral analysis is performed in order to verify the integrity of the PN generation methods used in simulations by comparing the results to the specified PN masks. As a next step, it is desirable to measure the impact of phase noise on modulated signals through simulations to fully characterize how DVB-S2X or similar systems are affected by the presence of PN.

In order to gauge the amount of phase noise that can be expected in a real implementation of the DVB-S2X system and to replicate that in the simulation environment, some phase noise masks defined in the DVB-S2X standards [1], [2] are presented to round out the chapter.

Section 2.1 focuses on the definition of phase noise in a non-ideal oscillator and gives some theoretical insight into the different processes that are present within phase noise.

In Section 2.2, the methods to analyze phase noise in the time- as well as frequency domain are introduced. Furthermore, modulation schemes used in DVB-S2X are recapped and analysis methods for PN-impaired modulated signals are given.

Finally, in Section 2.3, the phase noise masks chosen for analysis in the framework of this thesis are presented.

2.1. Phase Noise Definition

According to [3], an ideal oscillator output voltage time series $v(t)$ may be defined as

$$v(t) = A \cdot \sin(2\pi v_0 t), \tag{2.1}$$

where A is the signal amplitude that is regarded as unaffected by errors for the purpose of this thesis. This assumption is reasonable if e.g. a power limiter is employed for the output signal [4].

When considering a realizable oscillator as opposed to an ideal one, an element of phase uncertainty has to be introduced into Eq. (2.1):

$$v(t) = A \cdot \sin\big(2\pi v_0 t + \varphi(t)\big), \tag{2.2}$$

where the time-dependent phase fluctuation $\varphi(t)$ is denoted as phase noise.

In order to further analyze the phase noise contribution, the entire signal is commonly transformed to the frequency domain. The outline of this process is taken from [3] and [5] and not further discussed here.

The double-sided *Power Spectral Density* (PSD) $S_v(f)$ is obtained by transforming the squared oscillator voltage $v^2(t)$ to the frequency domain. We define $f = v - v_0$ as the frequency

difference between the actual frequency v and the carrier frequency v_0. Therefore, $S_v(0)$ represents the double-sided PSD at the carrier frequency.

Furthermore, the one-sided PSD $S_v^+(f)$ is directly obtained by omitting the PSD contributions at negative frequencies $v < 0$ completely. This is not to be confused with the single-sided PSD $W_v(f)$ introduced in [5], for which the relation

$$W_v(f) = 2 \cdot S_v^+(f) \tag{2.3}$$

holds true for all $f > 0$.

To characterize phase noise in the PSD representation, the symbol $\mathcal{L}(f)$ is introduced as

$$\mathcal{L}(f) = \frac{S_v^+\left(\frac{f}{1\text{Hz}}\right)}{S_v(0)}, \tag{2.4}$$

which denotes the power density in the positive phase modulation sideband relative to 1 Hz bandwidth divided by the carrier power. An illustration of $\mathcal{L}(f)$ and its definition is given in [6].

For modulated signals, Eq. (2.2) can be rewritten as [3]:

$$v(t) = A \cdot \sin(2\pi v_0 t + \Delta\varphi \cdot sin(2\pi f_m t)), \tag{2.5}$$

where f_m is the modulation frequency and $\Delta\varphi$ is the peak phase deviation caused by the modulation signal, which can be related as follows:

$$\Delta\varphi = \frac{\Delta v_0}{f_m}. \tag{2.6}$$

This relation is also known as the modulation index $m = \Delta\varphi$. Δv_0 is the peak frequency deviation of the carrier v_0.

The phase noise $\mathcal{L}(f)$ can then, using some additional relations from [3], be expressed as units of decibels relative to the carrier per Hertz bandwidth (dBc/Hz):

$$\mathcal{L}(f) = 20 \cdot \log_{10}\left(\frac{\Delta v_0}{2f_m}\right), \tag{2.7}$$

where $\Delta v_0 = \Delta\varphi \cdot f_m$ is given by Eq. (2.6).

Figure 2.1 shows the different spectral domains for phase noise, which can be characterized as follows [3]:

- Random walk frequency modulation noise (slope of f^{-4}) that is related to the physical environment of the source and affected by mechanical shocks, vibration, temperature or other environmental effects.
- Flicker frequency modulation noise (slope of f^{-3}) that is related to a physical oscillator resonance mechanism or the parts used in the realization of said device.
- White frequency modulation noise (slope of f^{-2}) that is related to the materials used in passive-resonator frequency oscillators, such as rubidium or cesium.
- Flicker phase modulation noise (slope of f^{-1}) that is related to the physical resonance mechanism in high-quality oscillators and can be introduced by amplifiers and frequency multipliers.
- White phase modulation noise (flat f^0 characteristic) that is introduced by the late stages of amplification in the same way as flicker phase modulation noise.
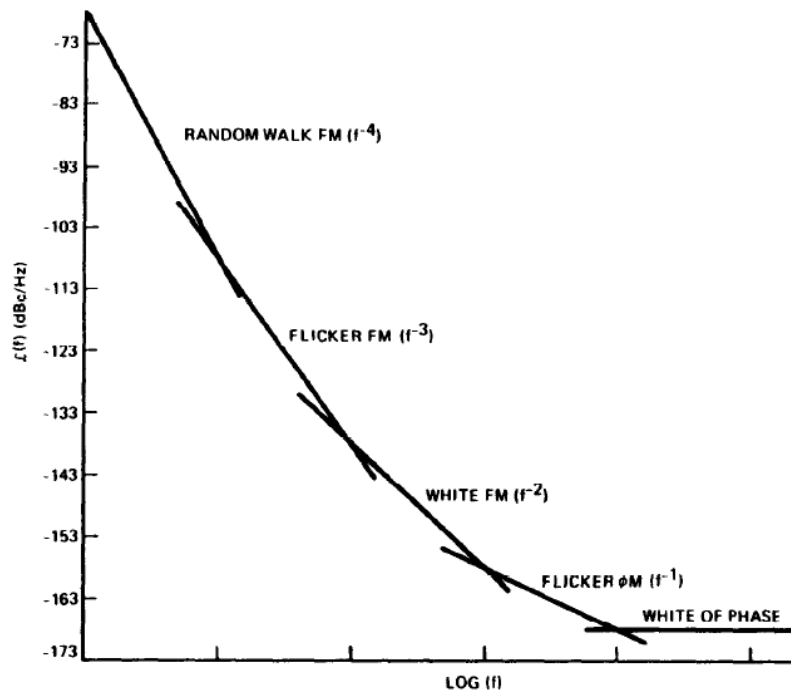
Figure 2.1: Phase noise processes [3]

2.2. Phase Noise Analysis

Having looked at what phase noise is and how it can be characterized, it is now necessary to introduce methods of analyzing its impact on a given waveform like DVB-S2X. This task falls to this chapter, which is organized in the following way:

In Section 2.2.1, methods for statistically analyzing the distribution of phase noise samples in the time-domain without a carrier or modulation signal are presented. The results of a simulation using these analysis tools are subsequently shown in Section 5.1.

Section 2.2.2 comprises the analysis of phase noise in the frequency-domain using a Fourier transformation on a waveform distorted by phase noise. This is primarily done to verify the integrity of the PN generation method via comparison of the results to the specified PN mask. Results for this type of analysis can be found in Section 5.2.

The analysis of modulated signals affected by phase noise is presented in Section 2.2.3. The corresponding results of this analysis method are found in Section 5.4.

2.2.1. Statistical Analysis

For the statistical analysis of time-domain phase noise samples, it is first necessary to characterize the random process that is represented by phase noise. As the only information about the PN process is available through the simulation of different realizations, two methods have been selected.

One realization of the random phase noise process is analyzed in a histogram with varying bin ranges and resolutions depending on the chosen phase noise mask in its entirety. The bin ranges are chosen so as to include the absolute largest PN samples that occur. The bin resolutions are chosen in a way that no bin is too sparsely populated to be able to determine the probability of occurrence of that bin.

To achieve this, each sample is sorted into bins according to

$$b_i < \varphi_k \leq b_{i+1}, \tag{2.8}$$

where b_i and b_{i+1} are the i-th and (i+1)-th bins and φ_k is the current phase noise sample. Each time a sample is sorted into a bin, the counter for that bin ϵ_i is incremented by one. The minimum bin b_{min} and the maximum bin b_{max} are chosen so that no phase noise samples are smaller or greater, respectively.

In order to compute a *Probability Mass Function* (PMF), the discrete-time variant of the more commonly seen *Probability Density Function* (PDF) from the histogram data, the total amount of samples T over the total number of bins n has to be determined using

$$\mathrm{T} = \sum_{i=1}^{n} \epsilon_i. \tag{2.9}$$

Then a PMF $f_X(i)$ is generated from the histogram data by applying (2.10) to each bin b_i.

$$f_X[i] = \frac{\epsilon_i}{\mathrm{T}} \tag{2.10}$$

Furthermore, the *Cumulative Distribution Function* (CDF) $F_X(i)$ is computed from $f_X[k]$ using

$$F_X[i] = \sum_{k=0}^{i} f_X[k]. \tag{2.11}$$

Finally, the *Complementary Cumulative Distribution Function* (CCDF) $\bar{F}_X[i]$ is derived from F_X via

$$\bar{F}_X[i] = 1 - F_X[i]. \tag{2.12}$$

Both CDF and CCDF are useful to analyze the lower and upper extrema of phase deviations due to phase noise in detail. For this purpose, a plot of CDF and CCDF with a logarithmically scaled y-axis is used to highlight the extrema.

The exact specifications of each test case are described in Section 5.1.1.

Using the same methods and the same form of a single realization of a random phase noise process, this time sampled at regular intervals, a random walk analysis is performed to show the statistics of the generated phase noise when taking into account longer phase drifts. For that purpose, the generated phase noise process is sampled every 100 ms for PN samples created with a sampling frequency of $f_s = 400\,\mathrm{kHz}$ and correspondingly every 1 ms for PN generated with $f_s = 40\,\mathrm{MHz}$. The resulting samples are analyzed using the same tools as described before, leading to a PMF and CDF/CCDF for each case.

If the analyzed statistical properties of both methods yield approximately equal results for a large number of analyzed samples, it can be assumed that the random PN process is at least wide-sense stationary, as its parameters are independent of time [7].

Once again, the exact specifications for this analysis method can be found in Section 5.1.2.

Furthermore, an ensemble of different realizations of the random PN process is taken and sampled at a constant time offset from the beginning of the observation. The comparison between this and the previous analysis methods should give some insight into ergodicity of the process. A random process is ergodic if it is at least wide-sense stationary and the time average of any arbitrary realization of the process is equal to the ensemble average of all realizations of the process at one time instant [7]. It is obviously not possible to simulate all realizations of the random PN process, however if a large enough amount of realizations is averaged so that statistically relevant results may be obtained, an assumption about the ergodicity of the random PN process may be made.

2.2.2. Spectral Analysis

In order to perform a spectral analysis of the phase noise process, a carrier waveform Ψ is required. For the purpose of this thesis, a complex sine wave has been selected:

$$\Psi(t) = \cos(2\pi f_c t) + i \cdot \sin(2\pi f_c t) \tag{2.13}$$

Ψ is then superposed with phase noise samples Φ to form the signal Θ:

$$\Theta(t) = \Psi(t) + \Phi(t) \tag{2.14}$$

Since this thesis focuses on simulations in the digital domain, continuous signals can only be represented by sampling with frequency f_s. The sampled representation of $\Theta(t)$ is denoted as $\Theta[n]$ or Θ_n in the following.

An implementation of the *Discrete Fourier Transform* (DFT) is necessary to transform the time-domain signal into the spectral domain for analysis. For computation efficiency reasons, the *Fast-Fourier Transform* (FFT) implementation of the Intel *Integrated Performance Primitives* (IPP) in C++ is chosen [8] as:

$$\Theta_k = \mathcal{F}\{\Theta_n\} = A \cdot \sum_{n=0}^{N-1} \Theta_n \cdot e^{-i \cdot \frac{2\pi k n}{N}}, \tag{2.15}$$

where n is the index of samples in the time domain, k is the index of samples in the frequency domain, N is the length of the FFT operation that necessarily must be a power of two to be efficient, and $A = 1$ is an optional scale factor.

The resulting sampled signal in the frequency domain Θ_k can then be converted into its logarithmic representation

$$\Theta_{k,\,\mathrm{dB}} = 10 \cdot \log_{10}\left(\Theta_k{}^2\right) \tag{2.16}$$

and adjusted to 1 Hz bandwidth

$$\Theta_{k,\mathrm{dB/Hz}} = \Theta_{k,\,\mathrm{dB}} - 10 \cdot \log_{10}\left(\frac{f_s}{N}\right). \tag{2.17}$$

Finally the dBc values can be obtained by

$$\Theta_{k,\,\mathrm{dBc}} = \Theta_{k,\mathrm{dB/Hz}} - \Theta_{k_0,\,\mathrm{dB}}, \tag{2.18}$$

where Θ_{k_0} represents the signal value in the frequency domain at the carrier frequency f_c. $\Theta_{k,\,\mathrm{dBc}}$ can then be used for comparison with the dBc values specified in the phase noise masks in Section 2.3.

2.2.3. Analysis of Modulated Signals

In terms of modulation techniques, the DVB-S2X standard implements *Binary Phase Shift Keying* (PSK), QPSK, 8-PSK, 16-ary *Amplitude and Phase Shift Keying* (APSK), et cetera, all the way up to 256-ary APSK. In the following, the QPSK constellation diagram and mapping is quickly described, the detailed description for the remaining modulation schemes can be found in [1].

For QPSK, two subsequent bits from the incoming bit stream are mapped onto one of four constellation points located at a distance of $\pi/2$ from each other on the unit circle in the *In-Phase/Quadrature* (I/Q) plane. In the DVB-S2X standard, Gray mapping is utilized. The constellation point in the first quadrant represents the bit sequence 00. The constellation diagram can be found in Figure 2.2, taken from [9], where similar diagrams can be found for the other modulation schemes up to 32-ary APSK. Diagrams for the larger schemes are found in [1].
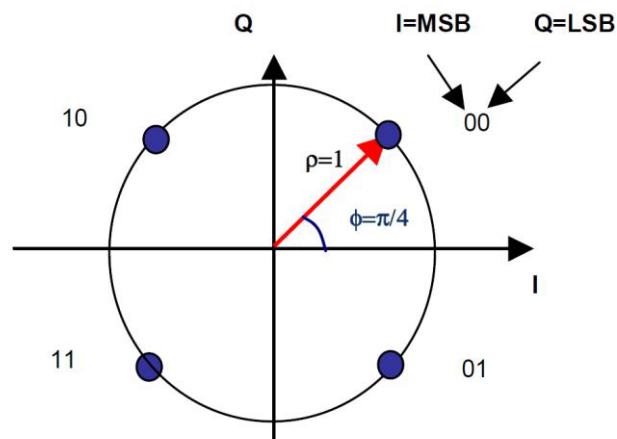
Figure 2.2: QPSK constellation diagram [9]

As a simple explanation, in order to successfully decode the QPSK symbol at the RX, the symbol affected by phase noise has to remain within its quadrant in the I/Q plane. If the added phase impairment causes the symbol to shift over quadrant boundaries, a symbol error, and resulting bit error, will occur; e.g. a transmitted "00" symbol being decoded as "01". The maximum allowed phase error for QPSK is therefore $\varphi_e = \pm\pi/4$.

To minimize symbol errors and therefore maximize the performance of the chosen data transmission scheme, phase trackers can to be employed to limit the impairment of the phase. The well-known *Viterbi-Viterbi* (V&V) phase tracker is used in the following to determine the performance gain of tracking the PN-impaired signal compared to the untracked signal. An explanation of how the V&V tracker works can be found in [10], a basic block diagram is given in Figure 2.3.
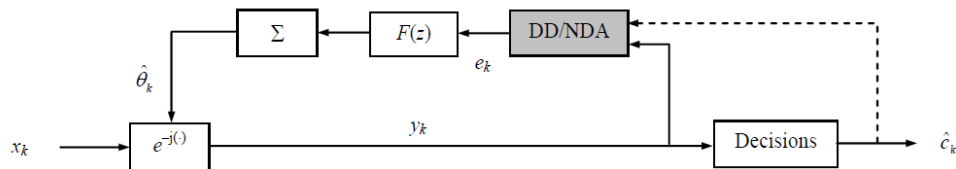
Figure 2.3: Block diagram of Viterbi-Viterbi phase tracker [10]

In order to judge the performance of the tracker, several parameters can be taken into consideration. An I/Q scatter plot shows the improvement of the phase tracker by a before-after comparison. In the case of e.g. QPSK, continuously distributed samples over the entire unit circle should be able to be separated into the four quadrants if the phase tracker performance is sufficient. Furthermore, the *symbol error rate* (SER) can also be a measure of the tracker performance, and in conjunction with it the *cycle slip rate* (CSR). A cycle slip occurs in the tracker when, in general terms, a noise event drives the synchronizer to a non-stable equilibrium point (hang-up) and one of the local minima instead of the global minimum from there [10]. For a *non-data-aided* (NDA) tracker, this usually results in a large number of samples being received erroneously, as no known symbols that could be used to correct the tracker are employed until the start of the next data burst. Figure 2.4 shows this circumstance in general terms.

Finally, for simulations taking into account the entire DVB-S2X framework including coding, the *frame error rate* (FER) is observed as a measure of performance. Using frames of length 16 200 bits, a frame error occurs if the frame contains more symbol errors than can be corrected using the coding involved. For DVB-S2X, the specifications of the coding used can be found in [9] and are summarized in Section 4.2.
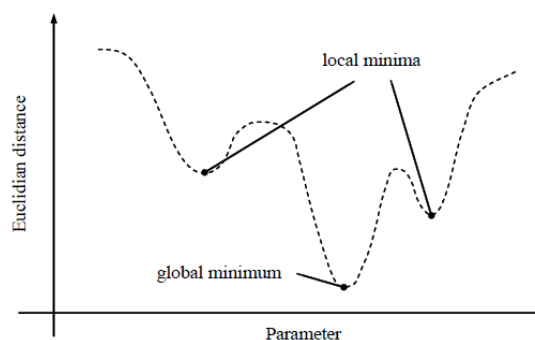
Figure 2.4: Cycle slip schematic for one-dimensional synchronization process [10]

2.3. Phase Noise Masks

In order to simulate phase noise accurately, a PN mask detailing the influence of phase noise over a wide range of frequencies is required. These masks can either be defined to represent the PN contribution of one source only or represent the aggregate of all PN sources within a link.

All masks represent the one-sided PSD $S_v^+(f)$ defined in Section 2.1 and are given in units of dBc/Hz, which defines the power level with relation to the carrier in terms of 1 Hz bandwidth.

In order to simulate the conditions of different DVB-S2X links, two masks have been chosen:

The critical mask represents an aggregate of phase noise in the DTH case and is defined in the Appendix of [1]. It is an aggregate mask in the sense of combining the influence over the entire transmission chain from ground station TX over satellite transponder to the RX LNB. The mask represents a worst-case scenario of all DTH masks presented for differing equipment and DVB-S2X frequency bands in [2]. The definition of the mask itself can be found in Table 2.1.

Frequency	Mask Λ [dBc/Hz]
10 Hz	-25
100 Hz	-25
1 kHz	-50
10 kHz	-73
100 kHz	-83
1 MHz	-103
≥ 10 MHz	-114

Table 2.1: Critical aggregate mask

The interactive link using VSAT is represented in the VSAT P2 mask defined in [2]. It has been derived there mainly from the contributions of state-of-the-art equipment and a transmission frequency in the K_a band; however it also is an aggregate mask. The overall PN values displayed in Table 2.2 are lower due to the higher quality of parts.

Frequency	Mask Λ [dBc/Hz]
10 Hz	-33
100 Hz	-62
1 kHz	-79
10 kHz	-89
100 kHz	-95
1 MHz	-105
≥ 10 MHz	-115

Table 2.2: VSAT P2 aggregate mask

Higher-quality parts used in the typical VSAT reduce the influence of phase noise on the overall link. In order to show the different phase noise contributions of TX, satellite transponder and RX, the individual contributions of the aggregate mask are presented in Table 2.3, taken from "Profile 2012-Ka-Non DTH" in [2].

Frequency	Uplink contribution	Satellite contribution	Downlink contribution	Aggregate mask [dBc/Hz]
10 Hz	-42	-33	-42	-33
100 Hz	-72	-62	-72	-62
1 kHz	-82	-80	-82	-79
10 kHz	-92	-90	-92	-89
100 kHz	-102	-95	-102	-95
1 MHz	-112	-106	-112	-105
≥ 10 MHz	-122	-116	-122	-115

Table 2.3: Individual contributions of aggregate VSAT P2 mask [2]

Furthermore, two masks not related to the overall DVB-S2X system, but rather the satellite on-board transponder as the focal point of the PN analysis, are given:

The transponder mask given by the *European Space Agency* (ESA) is supposed to represent the phase noise contribution of a typical on-board satellite transponder, which is of high quality compared to parts used for example in commercial off-the-shelf LNBs, therefore the defined dBc/Hz values as shown in Table 2.4 are much lower compared to the previous two aggregate masks especially for frequencies closer to the carrier. When comparing Table 2.4 to the satellite contribution assumed for the VSAT P2 mask in Table 2.3, it is shown that the mask profile depends heavily on which equipment is being utilized and whether a critical worst-case or typical use-case scenario is reflected even for equipment such as the satellite transponder.

Frequency	Mask Λ [dBc/Hz]
10 Hz	-63
100 Hz	-73
1 kHz	-83
10 kHz	-93
100 kHz	-112
≥ 1 MHz	-128

Table 2.4: Transponder Mask

Finally, the differential mask (also given directly by ESA) defines the lowest overall phase noise levels and is meant to represent the difference of two beams in a multiple spot-beam scenario. The main contributions of this mask therefore originate in PLLs, as different beams share the same oscillator, but different PLLs. This explains the characteristic of the mask with

comparatively very low influence in the lower frequency regions, as PN originating from PLLs mainly affects higher frequencies. The induced phase noise mainly poses a problem in multi-user detection or precoding applications, where it remains as a non-reducible impairment even if the stronger influences such as RX phase noise can be avoided. The defined PN values are presented in Table 2.5.

Frequency	Mask Λ [dBc/Hz]
1 Hz	-70
10 Hz	-100
100 Hz	-110
1 kHz	-120
10 kHz	-130
100 kHz	-150
≥ 1 MHz	-160

Table 2.5: Differential Mask

To summarize, Figure 2.5 depicts all four masks regarded within the thesis up to a frequency of 20 MHz. The relations and PN contributions over different ranges of frequency can be compared between masks fairly easily.
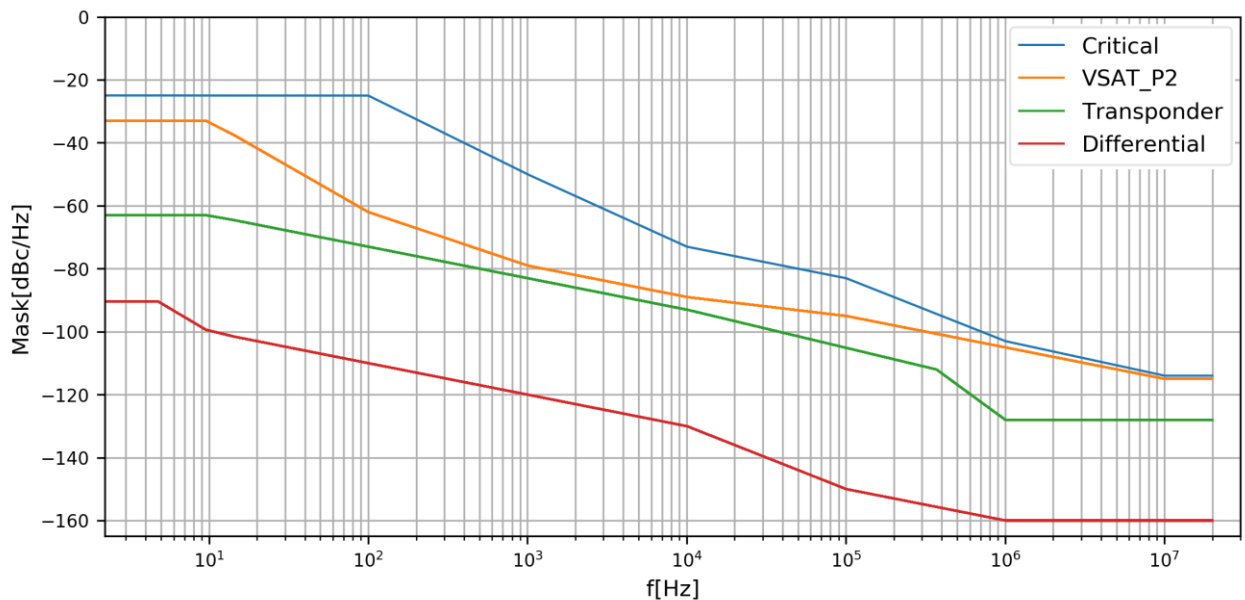
Figure 2.5: Comparison of phase noise mask profiles

3. Phase Noise Generation Methods

The implementation of phase noise generation in a digital simulation can be achieved in multiple ways. However, the most common models are not suitable for efficient simulation. Therefore other alternatives have to be investigated. A model that is both highly accurate and computationally efficient is necessary to fulfil all the requirements for large-scale high-throughput DVB-S2X simulations. Crucial to the implementation is a way to combine AWGN samples with one of the PN masks presented in Section 2.3. For this purpose, two methods are introduced and described in the following.

In Section 3.1, the first method using FFT and IFFT to transform the AWGN samples into the frequency domain before shaping them is introduced, which is the focal point of this thesis.

In Section 3.2, an alternative method using filter banks to shape the AWGN samples is shown.

In the following chapters, first the resulting PN samples from the IFFT method are analyzed closely in accordance with the title of the thesis, and later a comparison in terms of computational complexity and results between the two presented methods is given in Sections 4.3 and 5.3, respectively.

3.1. IFFT-based PN Generation

The IFFT-based method makes use of the efficient implementation of the FFT in digital systems to efficiently create large chunks of PN samples at a time. A block diagram of the basic procedure can be found in Figure 3.1. Important for this method is the choice of sampling frequency f_s and FFT length N so that the frequency resolution

$$\delta f = \frac{f_s}{N} \tag{3.1}$$

fulfills the condition $\delta f < f_{\Lambda,\min}$, or in other words: δf is smaller than the minimum frequency $f_{\Lambda,\min}$ specified in the selected PN mask.

If this condition is not fulfilled, the method is still operable, but the samples generated may not represent the desired characteristics of phase noise, as not all frequency points specified in the PN mask can be correctly represented. A very sparse frequency resolution δf in this case corresponds to a rough interpolation of the mask at low frequencies and may lead to missing power in the phase noise process PSD. However, the sampling frequency f_s cannot be chosen completely arbitrarily and has to be at least twice as large as the highest frequency that is of interest in the observation according to the well-known Nyquist theorem, e.g. f_s needs to be at least 20 MHz for masks that have a frequency point defined for 10 MHz, such as the critical and VSAT P2 mask, if the entire mask is to be represented. This puts a requirement on the size of N, meaning a certain minimum FFT length has to be maintained to accurately depict the chosen PN mask. In the end, this results in a tradeoff between computational performance in terms of FFT length N and the accuracy of the represented PN masks in terms of δf.

This tradeoff results in the disadvantage that an efficient implementation in hardware, for example *Field-Programmable Gate Arrays* (FPGAs), is difficult as in practice FFT lengths in excess of $N = 2^{19}$ are required to achieve a sufficient frequency resolution δf to represent the entire PN mask.

The advantages and drawbacks of the method are described in the following in Section 3.3.
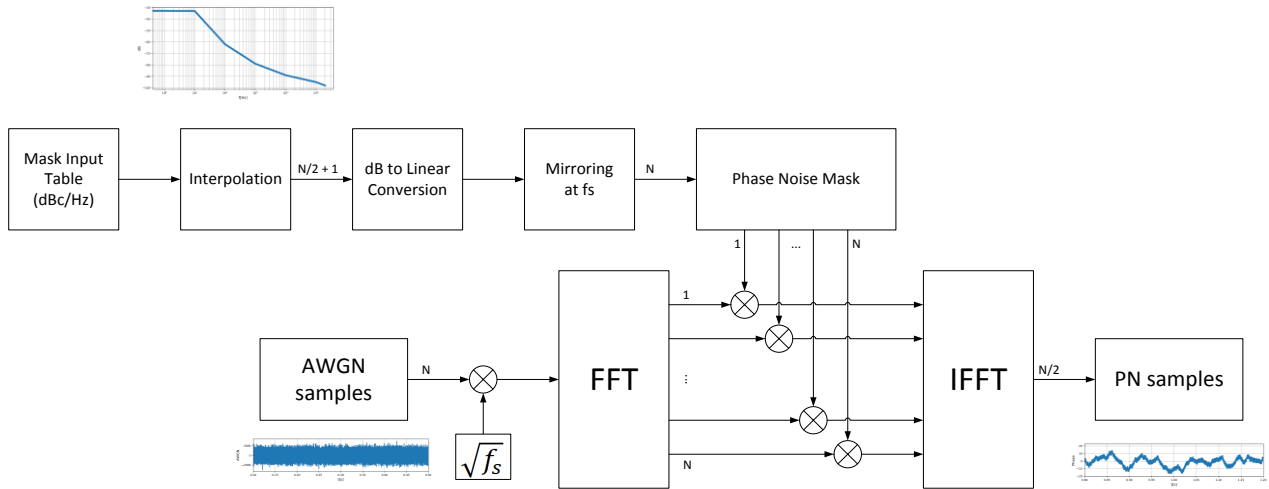
Figure 3.1: Block diagram of IFFT-based phase noise generation

In accordance with [5], the steps necessary for the PN generation using the IFFT-based method are described in the following:

1) Creation of AWGN samples: an AWGN process with $\sigma = \sqrt{f_s}$ is required as the source from which to generate PN samples. The chosen standard deviation of the white noise process ensures its spectral domain power is unitary. A block of N AWGN samples are needed as FFT input, where N is the FFT length. The generation of AWGN samples within the simulation requires several computationally expensive operations; the total impact on complexity is quantified in the following in Section 4.3.

2) FFT: the AWGN samples are converted to the frequency domain using the FFT algorithm in order to be processed further. The FFT implementation used in the simulation is provided by the IPP library.

   Mask generation: The chosen frequency domain mask $\Lambda(f)$ specified in Section 2.3 has to undergo linear interpolation in the logarithmic domain for all frequencies up to $f_s/2$, where for every $f \leq f_{M,min}$ the mask amplitude $\Lambda(f) = \Lambda(f_{M,min})$ and for every $f > f_{M,max}$ $\Lambda(f) = \Lambda(f_{M,max})$, or in other words: for frequencies smaller than the minimum specified mask frequency, mask values are set to the dBc/Hz value for the minimum mask frequency and vice versa at the upper end of the mask specification, simulating AWGN behavior for frequencies outside of those specified in the mask. An example of this can be found in Figure 2.5 for the Critical, VSAT P2 and Transponder PN masks, where for frequencies less than 10 Hz and greater than 10 MHz the curves are horizontal.
   After converting the interpolation results to the linear domain, the frequency axis has to be extended to f_s by mirroring all values at $f_s/2$. The resulting PN mask is then N samples long, equaling the length of the FFT.

3) Multiplication: Since both the AWGN process and the mask are now available in a frequency domain representation with the same length N, shaping the noise according to the PN mask is realized with a simple multiplication. For this step it is vital to have the sampling of the PN mask be the same as the frequency resolution δf of the transformed AWGN process. This constraint means that the interpolated PN mask cannot be reused if

the frequency resolution is changed during subsequent simulations. For convenience purposes and because of negligible computation time in most situations, the interpolated mask in the frequency domain that results from step 3) is therefore not saved between simulations but generated once during the initialization phase of each simulation.

4) IFFT: The AWGN samples shaped by the PN mask are then converted back to the time domain using the IFFT algorithm. Due to the "wrap-around problem when performing the convolution of finite segments" [5], only $N/2$ time-domain samples can be obtained from N frequency-domain samples. Considering that the PN mask had to be mirrored at $f_s/2$ in order to be multiplied with the AWGN samples, it is understandable that half the created samples are redundant. This process can be seen in Figure 3.2.

One important resulting consequence is that half of the N AWGN samples used in creating PN samples have to be buffered and re-used the next time PN samples are created in order to ensure the time-continuity of the random phase noise process, as shown in Figure 3.2.
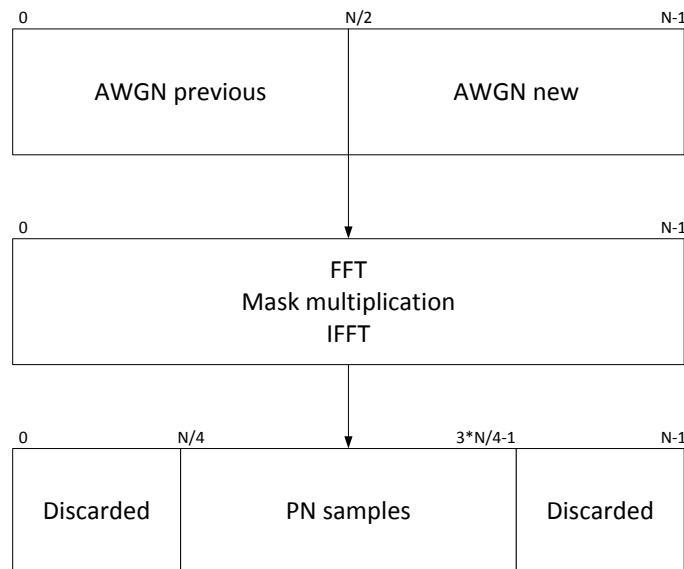
Figure 3.2: Detailed PN sample generation including N/2 discarded samples

One more issue arising from this PN sample generation procedure is that chunks of PN samples of arbitrary length cannot be created. Therefore buffers have to be utilized to save a PN sample chunk of length $N/2$ or multiples thereof. Samples can then be taken from this buffer in arbitrary lengths to satisfy the requirements of the simulation, which increases the simulation complexity in terms of memory management.

3.2. Filter-based PN Generation

The filter-based generation method uses filter banks and up-sampling techniques to create PN samples from an AWGN input. The method requires the necessary filters to be designed according to the chosen PN mask before the simulation. The filter impulse response needs to match the selected PN mask as closely as possible to achieve the desired characteristics of the PN impairment. This method of PN generation was used by Casini et. al. in [11] to simulate the impact of phase noise on the DVB-S2 system using two filters to realize one specific PN mask for a limited range of frequencies from 1 kHz to 10 MHz.

In order to expand on the method and to be able to simulate phase noise over a wide range of frequencies, some adjustments have to be made. Ideally, a single Finite Impulse Response (FIR) filter shaped according to the desired PN mask would be sufficient to create PN samples; however, this would lead to a prohibitively large number of filter coefficients not suited for implementation according to [12].

In order to prevent this, the filtering has been separated into two stages with maximum sampling frequencies of $f_{s,1} = 400\,\text{kHz}$ and $f_{s,2} = 40\,\text{MHz}$ with an up-sampling block in between. Instead of using a single filter for each stage, which would still lead to the same problem of requiring filters with a large number of coefficients, filter banks consisting of up to five parallel low-pass filters and a subsequent addition of samples are chosen. The chosen low-pass filters themselves are *Infinite Impulse Response* (IIR) filters of a maximum order of four, which are designed using the Matlab filter design tool, as described in [12]. The resulting *Second-Order Sections* (SOS) are then saved and can be imported into the simulation environment for an efficient application of the method.
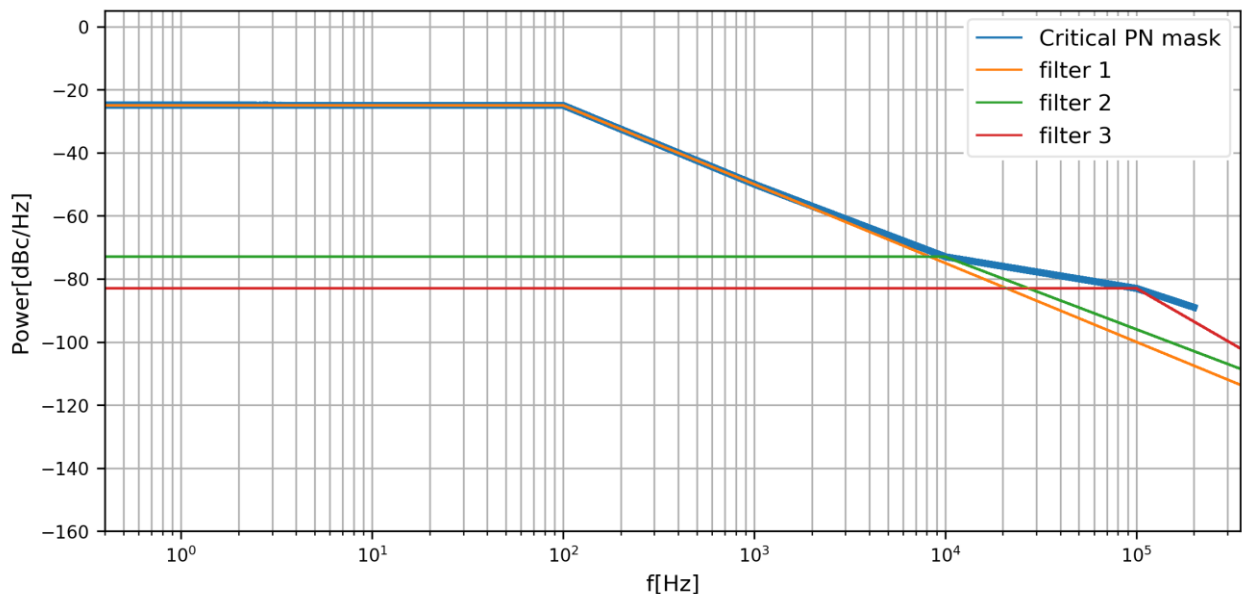
Figure 3.3: Filter bank PN mask representation example (critical PN)

An example of how the filter-based method is used to replicate the PN mask can be found in Figure 3.3, where the critical PN mask is recreated using a simple quantitative example of three low pass IIR filters with their cutoff frequencies at the values specified in the mask. This is to be taken as an explanatory case and does not represent the actual filter design process used.

The mask generation using such filter banks can be seen as an optimization problem with the criteria cutoff frequency, attenuation and filter order. However, in the scope of this thesis, an exact analysis is disregarded as the existing implemented filters are used. It falls to future investigations into this topic to present a solution that solves this optimization problem in an ideal manner.

A block diagram depicting the method can be found in Figure 3.4.

The up-sampling blocks are realized using zero-sample insertion and subsequent *Cascaded Integrator-Comb* (CIC), or Hogenauer, filters [13] of order four and variable conversion rates.

Due to the reliance on pre-designed filters that work for specific sampling frequencies only, the sampling frequency of the resulting PN samples f_s is limited to integer multiples of 400 kHz or 40 MHz, as CIC up-sampling is only possible for integer rates. If PN samples with other sampling frequencies are required, it is possible to use a resampling module to adjust the sampling frequency to non-integer multiples of 400 kHz or 40 MHz.

Because of the multiple stages of up-sampling and filtering, multiple branching steps are needed to create PN samples based on the desired sampling rate, as shown in Figure 3.4. The branching steps are explained more closely in the following.

Contrary to the IFFT-based method, the usage of SOS IIR filters with a small number of taps makes it possible to efficiently implement the filter-based PN generation method in FPGAs or similar hardware applications.

A comprehensive description of advantages and drawbacks of the method is given in the following in Section 3.3
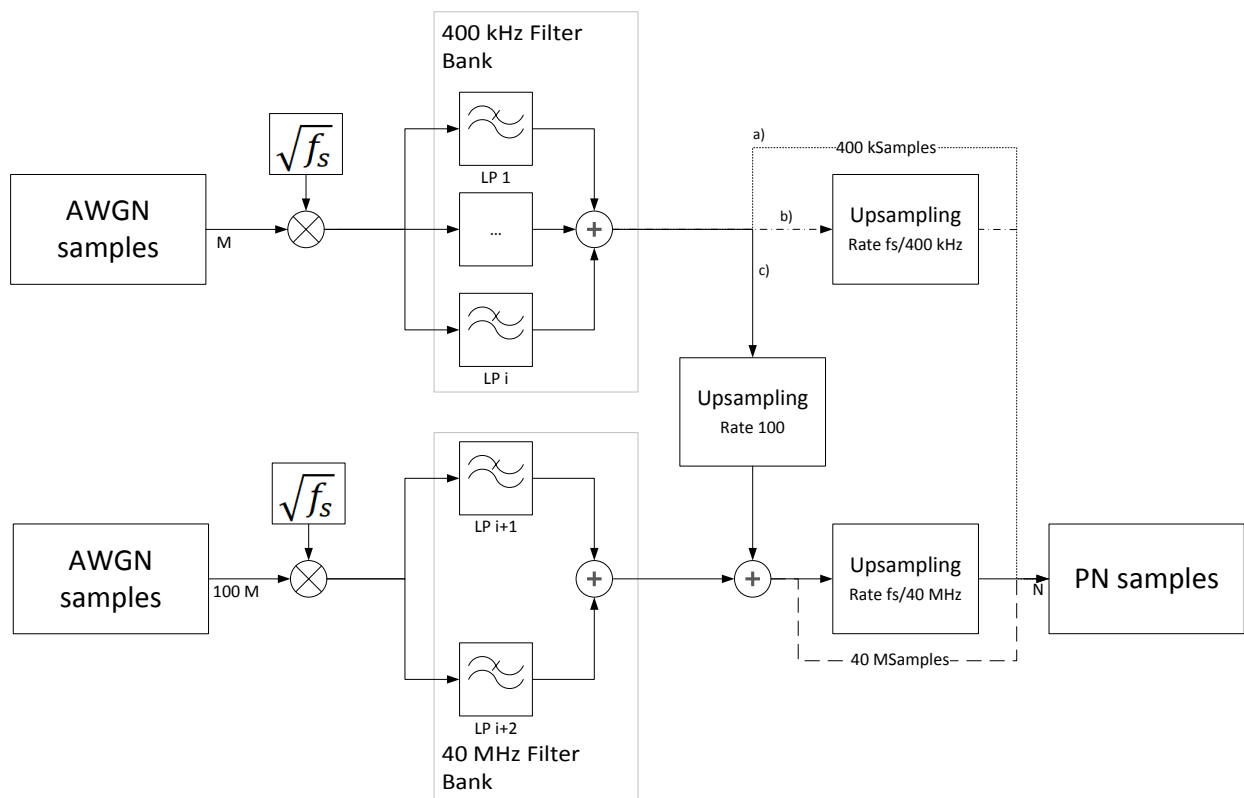
Figure 3.4: Block diagram of filter-based phase noise generation

The steps necessary to create PN samples according to the filter-based method are described in the following:

1) Creation of AWGN samples: analog to the IFFT-based method, an AWGN process with $\sigma = \sqrt{f_s}$ is required to generate PN samples. Even though no frequency domain conversion is performed, σ is still retained as a scale factor to ensure compatibility between methods. The rate of the AWGN process is $M = 400\,\mathrm{kSamples/s}$.

2) 400 kHz filter bank: the AWGN samples are filtered in parallel using i low-pass filters designed for $f_s = 400\,\mathrm{kHz}$ and subsequently added together. The required number of filters i depends on the chosen mask and the filter realization and is specified for the implementation used in this thesis for each mask in Section 4.2.

3) Depending on the desired sampling rate N of the resulting PN samples, three different alternatives exist for the next step:

   a. $N = 400\,\mathrm{kSamples}$: In this case, the desired rate N equals the current rate M and the samples after step 2) do not need to be processed further and can be taken as PN output samples (dotted line in Figure 3.4).

   b. $N = n \cdot 400\,\mathrm{kSamples}$, $n > 1$: In this case, an up-sampling filter with rate conversion n is required to create the output samples, the resulting rate of the PN samples is $N = n \cdot M$ (dash-dotted line in Figure 3.4).

   c. $N = n \cdot 40\,\mathrm{MSamples}$, $n > 0$: If the PN process needs to have a sampling rate in the range of MSamples, the additional steps continuing at 4) are required.

4) Rate 100 up-sampling: In order to transform the filtered 400 kHz AWGN samples to $f_s = 40\,\mathrm{MHz}$, they have to pass through an up-sampling filter with rate 100 or an equivalent filter bank with combined rate 100. The resulting rate of samples is $M' = 100 \cdot M$.

5) 40 MHz filter bank: AWGN samples from a separately generated process with rate $100M$, or 40 MSamples/s pass through the filter bank consisting of up to two low-pass filters designed for $f_s = 40\,\mathrm{MHz}$. No more than two filters are required to realize the PN masks defined in Section 2.3 as only a maximum of two mask points are at frequencies greater than 1 MHz. Analog to step 2), the required number of filters is dependent on the chosen mask and the filter realization and is specified for each of the utilized PN masks in Section 4.2.

6) Sample addition: the low-pass filtered output samples created during step 5) then need to be added to the up-sampling output samples from step 4) to form the phase noise process samples.

7) Depending on the desired sampling rate N one more branching step exists:

   a. $N = 40\,\mathrm{MSamples}$: In this case, no further processing of the samples is required and they are taken directly as the PN output samples (dashed line in Figure 3.4).

   b. $N = n \cdot 40\,\mathrm{MSamples}$, $n > 1$: If the resulting process requires a rate greater than 40 MSamples, an up-sampling filter with rate conversion n is necessary to adjust the sampling rate to $N = n \cdot M'$. In this way PN processes with rates that are integer multiples of 40 MSamples can be created.

3.3. Advantages and Drawbacks

The IFFT-based method will be regarded as the reference in the following since it represents the focal point of this thesis. Starting with this method, the advantages can be listed as:

- Adaptability in terms of PN mask
- Efficient implementation and scalability due to parallelization

Adaptability refers to the possibility to create phase noise samples based on any desired frequency mask using the IFFT-based method. The phase noise mask is generated at runtime from a set of values consisting of frequencies and attenuations as presented in Section 2.3, where all values in between the specified ones are obtained by interpolation in the logarithmic domain. Therefore, any form of mask may be realized as long as the frequency resolution δf defined in Eq. (3.1) is sufficiently able to represent the mask with the required accuracy. By comparison, the filter-based method requires going through the filter design and optimization process mentioned in Section 3.2 for each new mask, which results in a significantly increased complexity.

Another advantage of the IFFT-based method is that the FFT/IFFT methods required for the calculation of the PN samples are completely independent from the previously created samples. Only the AWGN samples need to be repeated in subsequent iterations of PN creation as described in Section 3.1, but no delay lines or other filter characteristics need to be considered, therefore an efficient implementation in C++ using parallelization is possible. This allows for a scalability of the performance of the method based on hardware limitations, and on modern multi-core CPUs allows for multiplying the overall throughput of the method by a factor of four to eight or even higher.

The drawbacks of the IFFT-based method are:

- Higher complexity
- Hardware implementation difficult

The overall complexity of the IFFT-based method is higher due to several factors. Firstly, because of the nature of the DFT producing both positive and negative frequencies, twice as many AWGN samples are needed to create the same amount of PN samples as with the filter-based method. Half the phase noise samples have to be discarded since they represent the negative frequencies in the DFT. Half the AWGN samples have to be saved and carried over to the next phase noise sample generation operation in order to guarantee time continuity of the generated PN samples. This results in additional complexity and memory management. Secondly, because the entire mask has to be realized by one sampling frequency and a sufficient frequency resolution is needed to cover all low frequencies represented in the mask if the required accuracy demands it, the required FFT length is in the range of 2^{19} to 2^{23} and high frequencies are represented with more samples than necessary. Here, the filter-based method with its two-step generation process and up-sampling in between has clear advantages in terms of computational complexity, and an improvement in complexity would be the implementation of an up-sampling functionality for the IFFT-based method as well. In summary, this leads to the lower computational performance of the IFFT-based method that will be focused on in Section 4.3.

Another downside of the IFFT-based method is the difficult implementation in hardware. As already mentioned in Section 3.1, due to the large required FFT lengths of up to 2^{23} that are required to keep the frequency resolution δf within the limits to fulfill accuracy requirements, an

implementation in hardware such as FPGAs becomes prohibitively difficult, as these would require a corresponding amount of hardware elements.

Conversely, regarding advantages and drawbacks from the perspective of the filter-based method, the lists could simply be reversed to read

- Lower complexity
- Efficient hardware implementation possible

as advantages and

- Higher computational complexity of mask adaptation
- Implementation performance limited

as disadvantages.

The topic of the result accuracy and a comparison thereof is to be determined in Section 5.3.

4.   Implementation and Simulation

In this chapter, the simulation framework is introduced and described. In order to fulfill the requirements of accurate phase noise generation as well as computational efficiency that were already mentioned in the introduction to this thesis, a highly efficient simulation environment is of paramount importance. Therefore, C++ has been selected as a programming language that facilitates the processing of large amounts of data within manageable time frames. In order to increase the efficiency of the implementation, additional third-party libraries have been included, most notably the Intel IPP that was mainly used for its efficient array operations and FFT implementation.

Modularity of the simulation framework is also a necessity, as a wide range of different simulations and analysis types are to be investigated, as already outlined in Section 2.2. This ranges from simulations with relatively limited scope in terms of computational requirements, like statistical and spectral analysis, to very elaborate full DVB-S2X system simulations using modulated signals. This means that a variable number of modules have to be included in the simulation depending on its complexity, i.e. a simulation environment that allows for this kind of flexibility is required. In order to satisfy these demands, the JOANNEUM RESEARCH simulation environment has been utilized.

In the following, details of the simulation environment and implementation are presented. Section 4.1 focuses on the simulation environment and its capabilities in general. Section 4.2 presents the modules involved in the simulations, utilized parameter sets and implementation details. In Section 4.3, the computational performance of the IFFT-based as well as the filter-based PN generation methods are analyzed within the simulation framework.

4.1. Simulation Environment

The JOANNEUM RESEARCH simulation environment provides an already existing and thoroughly tested high performance implementation of DVB-S2 and DVB-S2x waveforms. The capabilities of the simulator allow for the simulation of codec curves down to a FER of 10^{-5} and below in reasonable time. This is achieved through optimizations to the core C++ implementation using the IPP as well as additional external libraries. Further multi-threading and multi-computing were necessary to achieve the required simulation performance. A requirement for the IFFT-based phase noise generation method was not to limit the overall performance of the system, as well as to provide an accuracy of the spectral domain analysis with a deviation below 1 dB compared to the original phase noise mask.

The structure of the simulation environment is visualized in Figure 4.1 and outlined in the following. At its core, it is realized as a modular software concept which allows for project-specific functionality through the use of ASCII simulation files (sim-file), an example of which can be found in Figure 4.3 in the next section. Internally, the simulator utilizes the IPP, Intel Math Kernel Library (MKL) and Intel compiler to make use of advanced CPU instruction sets such as AVX which are necessary to cope with computational complexity requirements. Furthermore, the simulation core allows for parallelization on multicore CPUs as well as a server cluster of multiple machines. The simulation modules and algorithms are loaded on demand, as specified in the sim-file. A graphical user interface exists to control and monitor ongoing simulations. Furthermore, resources such as files specifying the PN masks or SOS coefficients for the IIR filters can be imported through specialized simulation modules. Scripted executions of

simulations make automated FER measurements and similar applications possible. The output of simulations is stored in form of numerical result files.
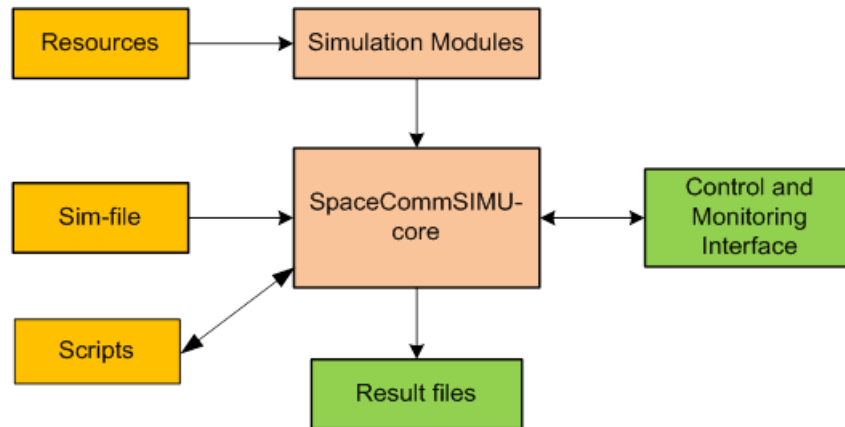
Figure 4.1: Basic structure of the JOANNEUM RESEARCH simulation environment

The JOANNEUM RESEARCH simulation environment provides the ideal working environment for simulations using DVB-S2X waveforms. Using such an environment circumvents limitations of a stand-alone simulation environment, such as simplifications due to time constraints, difficulties to verify results using untested code and the inability to take higher order functions such as modulation and coding into account properly.

The main goal of the thesis was adding the IFFT-based phase noise generation method as a module in the existing simulation environment with the aforementioned requirements in mind, resulting in a tradeoff between computational complexity and result accuracy. Furthermore, the method was to be used as a way to verify the code for the already existing filter-based PN generation method through the comparison of results. In practice, working with large code bases requires the adaptation of several modules for effective interoperability.

Using the available resources of the simulation environment, simple statistical and spectral simulations as well as complex full DVB-S2X system simulations with superposed phase noise impairment can be performed in an efficient manner. For this purpose, the simulator makes use of the highly parallelizable simulation structure and the computer grid the simulations are run on.

Additional aspects of the DVB-S2X system, such as the framing structure, *Bose–Chaudhuri–Hocquenghem* (BCH) and *Low Density Parity Check* (LDPC) codes with variable code rates, AWGN impairments on the channel, and synchronization can be taken into account for comprehensive simulations of the FER and will be summarized in the following section.

4.2. Simulation Structure

For the simulations of statistical and spectral analysis as described in Sections 2.2.1 and 2.2.2, the required modules are depicted in Figure 4.2: a tone generator, phase noise creation module, statistical and spectral analysis module. Data are handled within the simulation structure in form of burst containers, the lengths of which are chosen to coincide with the FFT length of the spectral analysis for convenience purposes, but are essentially arbitrary.
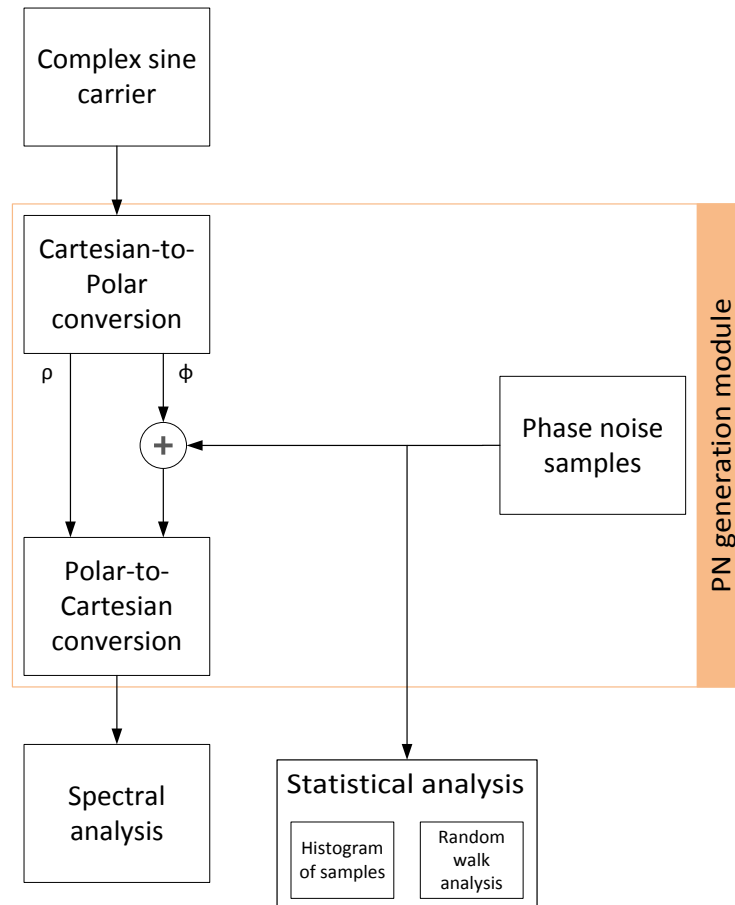
Figure 4.2: Block diagram spectral and statistical analysis

The tone generator module is responsible for creating a carrier waveform according to Eq. (2.13). In this case, a complex sine wave has been selected for this purpose, mainly for the reason that a later spectral analysis of a sine wave yields the well-known Kronecker δ function at one distinct frequency, leaving all other frequencies free of carrier influence and therefore only influenced by the phase noise process to be analyzed. The resulting samples are then segmented into burst containers for data handling purposes before being relayed to the next module.

The phase noise creation module provides the requested amount of phase noise samples using either the IFFT-based generation method (Section 3.1) or the filter-based generation method (Section 3.2). Since the samples can only be created in chunks of $N/2$ in case of the IFFT-based method, they may need to be buffered locally before being utilized. The detailed block diagrams on phase noise sample creation can be found in the aforementioned sections.

```
MODULE SimulationControl
     maxContainerLength              8400000
     maxLargeContainerLength         8400000
     containerNumber                 5
     largeContainerNumber            2
     loopsPerPoint                   50000
     loopsPerIntermediateResult      50000
     infoRate                        -1
     streamingMode                   1

STATIC_PIPE -1

// Tone Generator ------------------------------------------------------

MODULE SinToneGenerator
     freq                            4.76837158203125
     samplingFreq                    40000000
     amplitude                       1
     operatingMode                   2
     containerLength                 8388608

// PN generation -------------------------------------------------------

MODULE PhaseNoiseFFT
     samplingFreq                    40000000
     fftLength                       8388608
     bufferLength                    0
     maskID                          2
     operatingMode                   1
     IppCartPolarConversion          1
     randomSeed                      -1

// Spectral Analyzer ---------------------------------------------------

STATIC_PIPE -1

MODULE Spectrum_Analyzer
     startIndex                      0
     length                          8388608
     oversampling                    1
     windowType                      0
     normalizedOutput                0
     logXaxis                        0

STATIC_PIPE                         -1

END
```

Figure 4.3: Example sim-file for spectral analysis simulation of critical PN mask, f_s = 40 MHz

An example ASCII simulation file for this type of simulation can be found in Figure 4.3. When comparing it to the block diagram in Figure 4.2, it becomes apparent that each block is represented by one module in the sim-file. The input parameters for the tone generator are the output frequency, sampling frequency f_s, amplitude and burst container length, as well as a simulation-specific parameter operating mode. Using these parameters, the module creates a continuous sine wave sampled at the specified frequency and packed into burst containers of the given length. The input parameters of the IFFT-based PN generation module include once again the sampling frequency f_s, the FFT length N, the desired PN mask in form of an internal identification number ($maskID = 2$ corresponds to the critical PN mask in this case) as well as some parameters specific to the simulation. It uses a table saved in the simulation resources folder to translate the mask ID to the frequencies and amplitudes of the mask specified in Table 2.1 in Section 2.3, then interpolates said mask and creates PN samples according to the block

diagram for the IFFT-based generation method that can be found in Figure 3.1. Furthermore, the PN samples are added to the phase values of the sine signal after a Cartesian-to-Polar conversion. The aggregate values are then converted back to their Cartesian representation before the burst container is returned. The final module in this simulation is the spectral analyzer, which uses only the relevant input parameter FFT length. It transforms the PN-impaired samples it receives in each burst container to the spectral domain and averages the results over the number of simulation iterations specified. Once the simulation is complete, it also performs the adjustment to 1 Hz bandwidth and determines the carrier power in order to save the final spectral results in units of dBc/Hz, as described in Section 2.2.2. The simulation control module contains relevant information for the simulation core that is required for the simulation to work; the only relevant parameter that can be discussed here is loopsPerPoint, which denotes the overall iterations that will be performed by the simulation.

For the IFFT-based generation method, the following cases have been simulated with parameters chosen in order to facilitate comparisons with the filter-based method as well as to keep the computational complexity within a reasonable limit:

- A first parameter set of sampling frequency $f_s = 400$ kHz with FFT length $N = 2^{19}$, leading to a frequency resolution of $\delta f = 0.76$ Hz. This means that all the frequency points defined in the PN masks can be reproduced up to $\frac{1}{2}f_s$, as the frequency resolution is smaller than the first point in any of the masks. However, since all masks have frequency points greater than $\frac{f_s}{2}$, PN contribution at these frequencies are omitted. This parameter setting corresponds to using only the 400 kHz filter bank in the filter-based method.
- A second parameter set of sampling frequency $f_s = 40$ MHz with FFT length $N = 2^{23}$, leading to a frequency resolution of $\delta f = 4.77$ Hz. This is sufficient to fully portray the Critical, VSAT P2 and Transponder masks. This choice corresponds to using the added samples from both filter banks in the filter-based method.
- A third parameter set with sampling frequency $f_s = 4$ MHz and FFT length $N = 2^{23}$, leading to a frequency resolution of $\delta f = 0.48$ Hz. This is used exclusively for the Differential mask that requires $\delta f < 1$ Hz to fully represent the mask. While this parameter set has no counterpart for the filter-based method, it is acceptable to use because filters corresponding to the differential mask have not been implemented, and therefore the filter-based method cannot be used for comparison.

A tabular representation of the parameter sets is found in Table 4.1.

For the filter-based method, the number of 400 kHz filters i and number of 40 MHz filters is taken directly from the implementation described in [12] and can be found in similar fashion in Table 4.2. The efficiency of the filter-based method relies on the actual filters being designed before runtime using third-party tools. The SOS coefficients of the filters then only have to be imported into the C++ simulation framework in order to generate PN samples. However, this means that the differential mask could not be taken into consideration for the analysis because no filter coefficients were available. Despite that, the remaining masks offer a qualitative insight into the comparison of both methods.

Crit.	VSAT	Transp.	Diff.	Sampling frequency f_s	FFT length N [samples]	Frequency resolution δf [Hz]
■	■	■	■	400 kHz	2^{19}	0.76
			■	4 MHz	2^{23}	0.48
■	■	■		40 MHz	2^{23}	4.77

Table 4.1: Parameter sets for IFFT-based PN generation for Critical, VSAT P2, Transponder, and Differential mask

Crit.	VSAT	Transp.	Number of 400 kHz LP filters i	Number of 40 MHz LP filters	Total number of LP filters
■			3	2	5
	■		5	2	7
		■	4	2	6

Table 4.2: Number of bandpass filters per filter bank for filter-based PN generation for Critical, VSAT P2, and Transponder mask

If phase noise samples have to be combined with carrier samples for the spectral analysis, a conversion module is required to transform the Cartesian carrier samples $a + ib$ into their polar representation using the following relationships:

$$\rho_k = \sqrt{a^2 + b^2} \tag{4.1}$$

$$\phi_k = \arctan\left(\frac{b}{a}\right). \tag{4.2}$$

The phase noise samples can then be added to the carrier phase samples by simple addition according to Eq. (2.14). Finally, the conversion to polar coordinates has to be reversed:

$$a = \rho_k \cos(\phi_k) \tag{4.3}$$

$$b = \rho_k \sin(\phi_k). \tag{4.4}$$

Since the statistical analysis functions using raw phase noise samples without a superposed carrier, the samples for this form of analysis can be taken straight from the phase noise creation module (see Figure 4.2)

The FFT module performs the spectral analysis of the combined carrier and phase noise samples. Its theoretical groundwork is described in Section 2.2.2. The FFT length N has to be chosen so that a sufficiently small δf for the regarded phase noise mask and the simulation accuracy requirements is achieved according to Eq. (3.1), as already discussed in Section 3.1. In order to verify the PN generation process, the FFT frequency bins are then adjusted to 1 Hz bandwidth and the carrier bin power subtracted to obtain dBc values for each bin. The

comparison between the original PN mask and the resulting dBc values then yields the accuracy of the PN generation method; the closer they are, the better the characteristics of the random PN process matches the specified PN mask. Further, these results in the spectral domain can also be used to compare the accuracy of results between the different PN generation methods as well as give some insight into the quality of the designed filter banks for the filter-based PN generation.

In the time domain analysis module, the statistical analysis outlined in theory in Section 2.2.1 is performed. This is divided into two analysis methods, the first is a histogram taken from all samples of one realization of a random phase noise process up to a given maximum number of samples for each of the PN masks. With this, the overall distribution of phase impairment is analyzed and statistical properties of the process such as the mean value μ and standard deviation σ can be derived. Furthermore, using the CDF and CCDF of the process, the probability of phase deviations larger than a certain threshold can be obtained and the maximum phase deviations are comparable between masks.

The second method is a random walk analysis where one realization of a random phase noise process is sampled at regular intervals of 100 ms for $f_s = 400\,\mathrm{kHz}$ and 1 ms for $f_s = 40\,\mathrm{MHz}$. The sampled process is then again taken as the input for a statistical analysis including a histogram, PMF and CDF as well as CCDF. The results can be compared to the results from the first analysis method to determine if longer phase drifts of a scale of the sampling periods exist within the random phase noise process and how those affect the statistical properties. A graphical representation of the samples involved in this analysis method is found in Figure 4.4 for an example PN process using the VSAT P2 mask and a sampling frequency of $f_s = 400\,\mathrm{kHz}$.
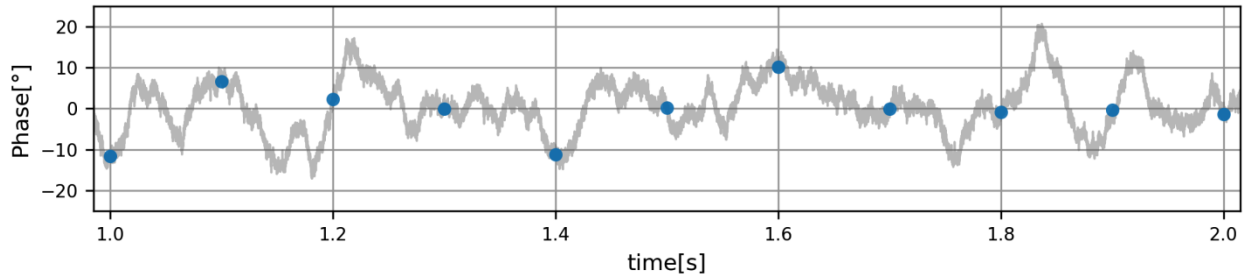
Figure 4.4: Time series of VSAT P2 PN samples for f_s = 400 kHz, samples for random walk analysis are highlighted

For completeness, this second analysis method is also compared to a similar method where instead of sampling one realization of the random phase noise process N times, N realizations of the process are taken and sampled once after 100 ms for $f_s = 400\,\mathrm{kHz}$ each. However, due to the complexity of this method in the simulation framework, only a limited amount of realizations N could be realized.

Moving on from these simulations to analyze the generation methods and properties of PN in an isolated fashion, it is desirable to address modulated signals in some way. As a first step of this analysis, the I/Q components of a QPSK-modulated signal distorted by phase noise is regarded and analyzed. The results are compared to the output of a phase tracking module using a V&V phase tracker, as described in Section 2.2.3. Figure 4.5 depicts a block diagram of the entire processing chain of a modulator-demodulator structure distorted by phase noise.

The TX module consists of a bit stream generator that creates a stream of constant zeroes, two of which together are then mapped to the QPSK constellation point 00 by the mapper as defined in [9]. While this does not reflect the characteristics of a real modulated signal transmission, it allows for an easier analysis of the impact of phase noise on the system, as all symbols can be regarded as known at the receiver, which allows for easier calculation of the SER.

In the following, the baseband QPSK symbols are zero-padded and root-raised cosine (RRCos)-filtered to create the HF signal.
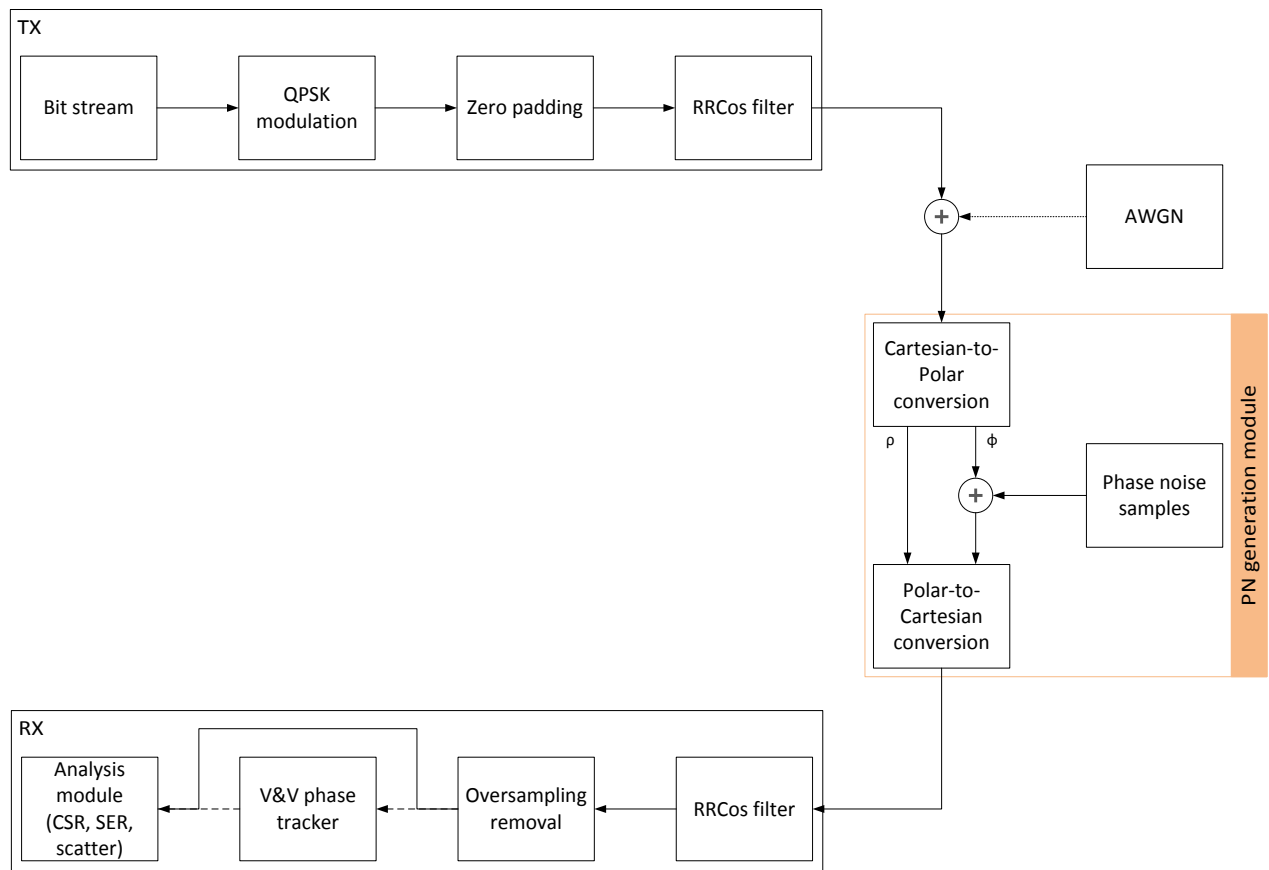
Figure 4.5: Block diagram of modulated I/Q scatter plot creation

The channel consists of the phase noise impairment that is superposed with the radio frequency (RF) samples as well as optional AWGN (dotted line in Figure 4.5). Because the PN masks are aggregate masks that combine the influence from various TX, satellite transponder, and RX sources, it is a valid procedure to add the entire impairment in one step for simulation simplicity.

The RX module then down-samples the HF signal to the baseband using a matched RRCos filter and the oversampling introduced in the TX is removed. If used, the phase tracking module then attempts to recover the phase of the QPSK symbols (dashed line in Figure 4.5). The loop bandwidth $B_L T$ of the tracker may be varied to adjust tracker performance based on the severity of phase noise added. Finally, the QPSK symbols impaired by phase noise can be plotted in a scatter plot in the I/Q plane. Furthermore, the CSR and SER of the transmission scheme may be determined.

In order to assess the impact of phase noise on the overall DVB-S2X system, a simulation using the entire modulation and coding structure of DVB-S2X is performed to measure FER for different modulations.

Without going too deep into the specifics of the DVB-S2X standard, the entire details of which can be found in [1] and [2], the simulation structure is briefly explained in the following. A visual representation of it is found in Figure 4.6.

The packet generator is used to create data bytes used in the transmission. These are then converted to bit level. Two different frame lengths are supported by DVB-S2X, which are 64 800 bits for normal and 16 200 bits for short frames. For simulation purposes, only short frames have been used.

The encoding is done in two steps using different codes. An outer BCH block code with an error correction capability of 12 and a resulting length of 168 bits is applied first, followed by an LDPC code of variable length depending on the chosen code rate. As the code rate does not significantly influence the performance degradation introduced by phase noise, a static code rate has been selected for each modulation scheme in the simulations.

The resulting coded bits are then mapped onto the symbols of the selected modulation scheme ranging from QPSK to 32-APSK as well as zero-padded and RRCos filtered to obtain the HF signal.
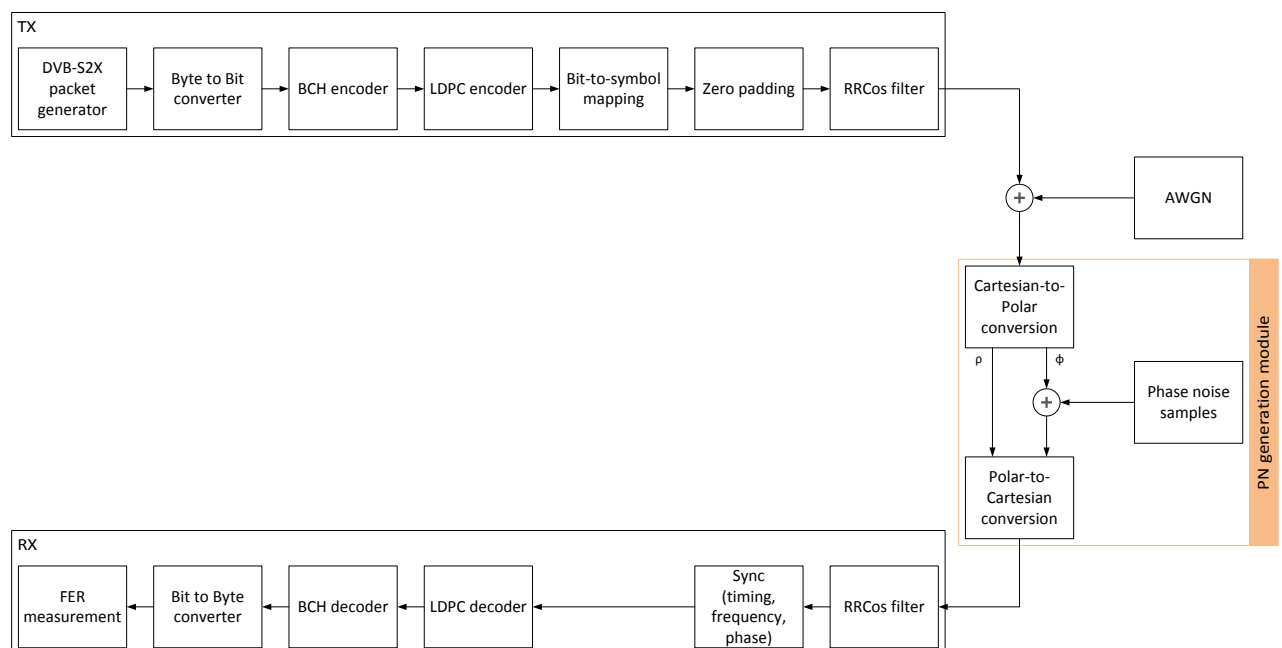
Figure 4.6: Block diagram of complete DVB-S2X system simulation for FER measurements

The channel is represented by an AWGN addition that regulates the overall system *Signal-to-Noise Ratio* (SNR) as well as the addition of phase noise onto the signal phase, which necessitates a conversion from a Cartesian-to-Polar signal representation and back. Again, as the PN mask is an aggregate of all phase noise sources within the system (TX, satellite transponder, and RX), adding the aggregate phase noise can be done in one step.

The RX stage then needs to move the HF signal to the baseband by way of a matched RRCos filter and perform synchronization in terms of symbol timing, frequency and phase. However, for the case of simulating the system performance degradation due to phase noise impairment, no additional timing or frequency errors have been introduced that would need to be corrected. The synchronized symbols are then decoded in two steps, first by the LDPC, then by the BCH decoder, to remove residual errors and correct blocks of errors, respectively.

Finally, a bit-to-byte conversion is performed to return to the byte format originally used to create data, and a comparison of the generated and the decoded data yields whether the frame was received erroneously or not, leading to a FER measurement if a sufficiently large number of frames is analyzed in this way.

4.3. Performance

In order to assess the computational performance of the simulation, the main parameter being examined is the throughput in samples/s. Because the overall throughput in a serial chain of modules is always equal to the throughput of the slowest module, it is sufficient to analyze one module at a time. The requirement for the implementation of the IFFT-based generation method as stated in Section 4.1 was an efficiency equal to other modules in the simulator so that the overall performance is not impaired. It is therefore enough to analyze and compare both PN generation methods in terms of their computational efficiency and throughput, knowing that the maximum throughput of the overall JOANNEUM RESEARCH simulator was assessed internally to be roughly 40 MSamples/s for a simulation comparable to the one presented in Figure 4.6. The desirable figure of merit for the throughput of the PN generation modules, therefore, is that the throughput in Samples/s is so that the overall simulation is not slowed down by including the PN generation module.

For the tests, PN was generated using the VSAT P2 mask, which makes no difference for the IFFT-based method, but constitutes a worst-case for the filter-based method as the maximum amount of filters have to be calculated, as seen from Table 4.2.

The remaining parameters were also chosen as a worst-case, as the full mask has been simulated with $f_s = 40$ MHz and FFT length $N = 2^{23}$, leading to a frequency resolution of 4.77 Hz, as can be seen from Table 4.1.

In order to minimize the impact of buffering, chunks of data equal to the FFT length N have been processed in each burst container. Knowing the number of samples processed, it is necessary to measure the processing time to calculate the throughput using

$$\text{Throughput} = \frac{\text{Samples processed}}{\text{Processing time}}. \tag{4.5}$$

For the IFFT-based PN generation method, the computationally most complex steps are the Cartesian-to-Polar (and vice versa) conversion, creation of AWGN samples and the FFT/IFFT calculation. The mask creation and interpolation from the PN mask tables presented in Section 2.3 is done only once in the initialization phase of the simulation, therefore its influence can be disregarded for long simulations.

Based on measurements, creating 2^{23} (or 8 388 608) PN samples takes 1020 ms, leading to a module throughput of only 8.2 MSamples/s. This assumes a strictly serial processing of tasks in the method. However, the architecture of the JOANNEUM RESEARCH simulator allows highly

parallelized processing of modules within the simulation chain, therefore a parallel implementation of the IFFT-based PN generation method is possible.

The only task within the IFFT method that cannot be parallelized is the creation of the AWGN samples, as each block of PN samples requires half of the previous AWGN samples to be available for time continuity reasons, as explained in Section 3.1. The proposed parallel method makes use of a "domino-like" scheme, where AWGN blocks that consist of one half of repeated samples and another half of new samples are created in serial fashion and passed to a parallel processing structure through a queue element that buffers the AWGN blocks. The computationally most expensive tasks, like the Cartesian-to-Polar conversion (and vice versa) as well as the FFT and IFFT methods, are subsequently performed in parallel. In the end, the signal impaired by PN is available in each burst container; however the bursts that leave the parallel structure are not necessarily in order anymore. This is due to one parallel arm being possibly slightly faster in terms of execution time than the other, therefore an additional queue element is needed at the end to restore the original order of burst containers. A graphical representation of the parallelization structure can be found in Figure 4.7.

The parallelization order i can be chosen arbitrarily, but significant processing time gains can only be achieved if the number of CPUs available on the simulating machine is larger or equal to i and the throughput of the domino-style AWGN generation is not lower than the throughput of the parallel structure following it. In this case, $i = 4$ is chosen in accordance with the conditions above.

Table 4.3 lists the measured execution times in ms for the different tasks within the parallel method. Because AWGN and PN generation are now two different modules, the execution time of the AWGN sample generation can be disregarded for the throughput calculation, as it is significantly lower than the PN generation execution time. FFT and IFFT can easily be identified as the largest contribution to the overall PN generation execution time alongside the Cartesian-to-Polar (and vice versa) conversions. Shorter tasks are collectively summarized without listing every single one separately.

Task	Duration [ms]
Sequential AWGN generation (separate module)	**50**
FFT calculation	*330*
IFFT calculation	*340*
Cart-Polar/Add/Polar-Cart	*180*
Misc. tasks	*120*
Parallel structure total	**970**

Table 4.3: Processing times for parallel implementation of IFFT-based PN generation method separated by tasks in ms for blocks of length 2^{23}

The overall throughput of the IFFT-based PN generation method then increases to

$$\text{Throughput} = i \cdot \frac{\text{Samples processed}}{\text{Processing time}} \qquad (4.6)$$

and with the choice of $i = 4$ yields a result of approx. 35 MSamples/s. This number is much closer to the desired 40 MSamples/s, so using a higher parallelization order i in conjunction with the appropriate hardware can easily achieve that target.
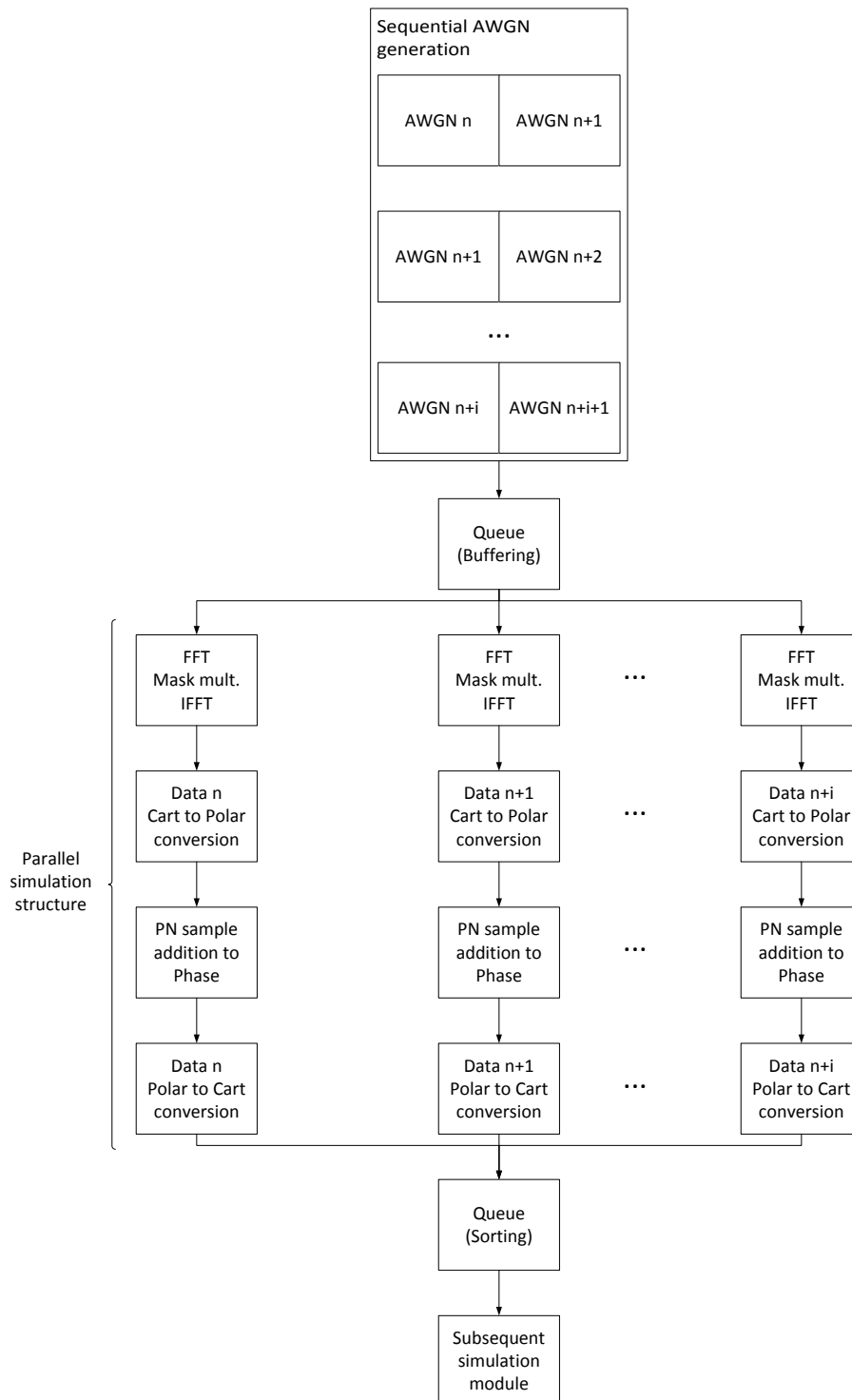
Figure 4.7: Parallel simulation of IFFT-based PN generation in JOANNEUM RESEARCH simulator

For the filter-based method, the complexity of creating the SOS filter coefficients is outsourced and therefore doesn't add to the execution time of the module, leaving the CIC up-sampling to 40 MHz and the 40 MHz filter bank as the most computationally complex steps.

Analog to the previous analysis of the IFFT-based method, a breakdown of the tasks and their required execution time is given in Table 4.4. It can be seen that once again the Cartesian-to-Polar (and vice versa) conversion in sum take a large chunk of the overall time. The CIC up-sampling filter that converts the 400 kHz samples to 40 MHz ones and the 40 MHz filter bank, despite consisting of only two filters, are the other big contributors, as suspected. The 400 kHz filter bank is computationally very efficient, which can be explained by the relatively small amount of samples it needs to process. Once again, all other tasks are cumulatively specified.

Task	Duration [ms]
Cart-Polar/Polar-Cart	*180*
AWGN generation	*50*
400 kHz filter bank	*10*
40MHz up-sampling	*170*
40MHz filter bank	*180*
Misc. tasks	*30*
Total duration	**620**

Table 4.4: Processing times for filter-based PN generation method separated by tasks in ms for blocks of length 2^{23}

Using these measured values, the throughput of the filter-based method can be calculated as approx. 13.5 MSamples/s. In order to achieve higher throughputs, the filter banks and especially the up-sampling filters could be designed more efficiently using IPP functions instead of a direct implementation. It is estimated that this step would increase performance at minimum by a factor of four for the up-sampling and filter banks, leading to a theoretical total duration of the simulation of 350 ms, which corresponds to a simulation time improvement of roughly a factor of two. This increases the overall throughput to approx. 24 MSamples/s, leaving the Cartesian-to-Polar (and vice versa) conversions as a significant limit that prohibits reaching the desired throughput of 40 MSamples/s.

5. Phase Noise Analysis

Having discussed the simulation structure and implementation details of the simulation environment, the results obtained via simulations are presented in this chapter. The influence of phase noise impairment onto a DVB-S2X system have been simulated in a variety of ways focusing on both time-domain statistical results, frequency-domain spectral results and the results obtained via more complex simulations using modulated signals as specified in the DVB-S2X standard [1].

In Section 5.1 the findings from the statistical analysis are presented, along with a detailed description of how they were obtained from the raw PN samples created in the simulation.

Section 5.2 focuses on the spectral analysis of a PN-impaired sine carrier waveform using an FFT to transform the samples into the frequency domain.

Additionally, both methods are revisited in Section 5.3, where a comparison between the IFFT-based and the filter-based PN generation methods is shown.

The chapter is concluded by Section 5.4, that focuses on modulated signals impaired by PN, which is the most complex scenario analyzed in the framework of this thesis and is meant to show the influence of PN on an entire system structure such as that of DVB-S2X.

5.1. Statistical Analysis

For the statistical analysis of the generated PN process the raw PN samples are observed in the absence of a carrier signal, as can be seen from the block diagram in Figure 4.2. Statistical properties of the noise, namely mean value μ and standard deviation σ, are calculated, and the PMF as well as CDF/CCDF are created with the help of a histogram of the data according to the method described in Section 2.2.1.

The histogram bins are chosen with different values for each mask in order to have approximately the same amount of bins for each mask and ensure that enough samples are present in each bin so that a meaningful probability can be obtained for the PMF. The histogram ranges have to be different for each mask due to the large variation of magnitudes of the PN samples depending on which mask was used for the creation, e.g. the critical mask produces PN samples of > 200° magnitude, whereas the maximum magnitude of the phase noise for the differential mask is < 0.2°. The exact specification of the bin ranges and resolution is given in the analysis in the following.

The analysis of the raw samples is performed in Section 5.1.1 for sampling frequencies of $f_s = 400\,\text{kHz}$ for all four PN masks, and $f_s = 40\,\text{MHz}$ for critical, VSAT P2, and transponder mask, as well as $f_s = 4\,\text{MHz}$ for the differential PN mask as a smaller frequency resolution δf is required to accurately represent the 1 Hz point defined in the mask. For each plot, 5 000 containers of 2^{19} samples for $f_s = 400\,\text{kHz}$, and 2^{23} samples for $f_s = 40\,\text{MHz}$, have been simulated, leading to a total amount of approx. $2.6 \cdot 10^9$ and $4.2 \cdot 10^{10}$ samples, respectively.

The analysis of the random walk statistical properties is presented in Section 5.1.2, where first the method is further explained, followed by the results being compared to those of the raw PN sample analysis. In order to make this comparison possible, the sampling frequencies, histogram bin resolutions and bin ranges have to be chosen identically to those in the raw PN sample analysis.

5.1.1. Statistical Analysis of Phase Noise Samples

5.1.1.1. Critical Mask

For the critical mask, a frequency bin resolution of 5° has been chosen. The bin ranges are chosen to encompass ±440° to facilitate the comparison with the filter generation method in Section 5.3.1.

First of all, in Figure 5.1 an exemplary time series of PN samples created with the critical PN mask is visualized for a length of 0.1 seconds and sampling frequency $f_s = 400\,\text{kHz}$. The different frequency components of the signal as well as the random walk characteristics over short time-frames can be seen.
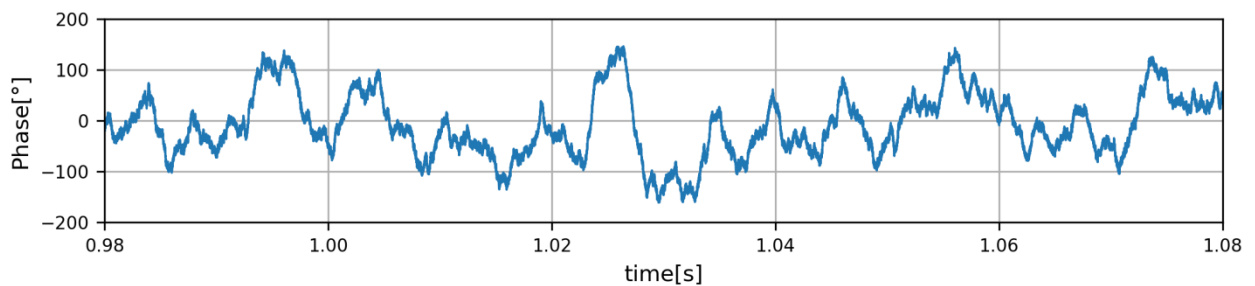
Figure 5.1: Time series of PN samples created from critical PN mask for f$_s$ = 400 kHz

For $f_s = 400\,\text{kHz}$, the expectation is calculated as $\mu = 0.0003°$ and can therefore safely be rounded to zero. As this is true for all of the following cases, it will not be separately stated in each case. Instead, the standard deviation σ is regarded as a parameter quantifying the distortion caused by different types of phase noise. In this case, the standard deviation is $\sigma = 58.99°$. PMF and CDF as well as CCDF can be found in Figure 5.2 (a) and (b), respectively.

The results resemble a Gaussian distribution with mean value of zero. No phase limitation is applied in this case, meaning phase values greater than 180° and smaller than -180° occur, that would normally be projected onto values of their respective opposite sign counterpart on the unit circle, e.g. 185° would be represented as -175°.

When regarding the CDF and CCDF, only statements about the probability of values greater than the observed value in case of the CCDF and smaller than the observed value in case of the CDF can be made. Therefore, the probability of a value of greater than 180° occurring must be determined using the CCDF curve and is approx. $2 \cdot 10^{-3}$. Since the distribution of the samples is zero-mean Gaussian and therefore symmetrical with respect to the y-axis, the same probability of occurrence holds true for values smaller than -180°, this time determined from the CDF curve. Therefore, the combined probability of occurrence of absolute phase values $|\varphi| > 180°$ is approx. $4 \cdot 10^{-3}$. This is further supported by the 3σ rule of thumb that states that approx. 99.7% of samples lie within the ±3σ range, which is ±177° in this case.
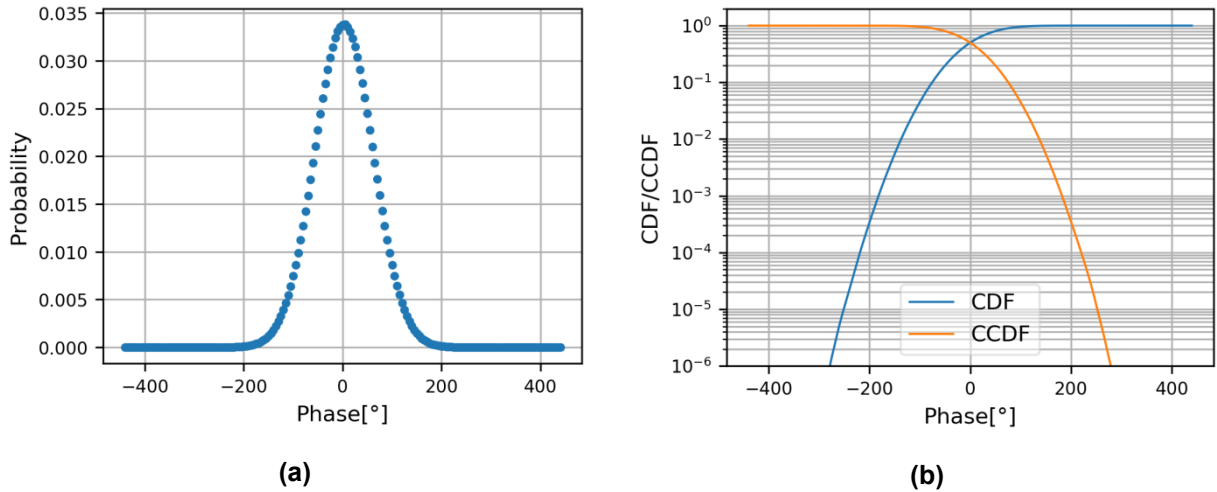
Figure 5.2: (a) PMF and (b) CDF/CCDF of histogram analysis of critical mask for f$_s$ = 400 kHz (2.6·10^9 samples)

For $f_s = 40\,\text{MHz}$, which takes the entire defined PN mask into account, the expectation is $\mu = 0$ again, and the standard deviation is $\sigma = 59.00°$. The similarity of the values compared to the lower sampling frequency suggests that the additional contribution from higher frequencies is in fact not quantifiable using statistical properties of the process. This suggestion is further supported by the similarities of PMF and CDF/CCDF in Figure 5.3 (a) and (b), respectively. The same tendencies as exhibited by Figure 5.2 are present here again.
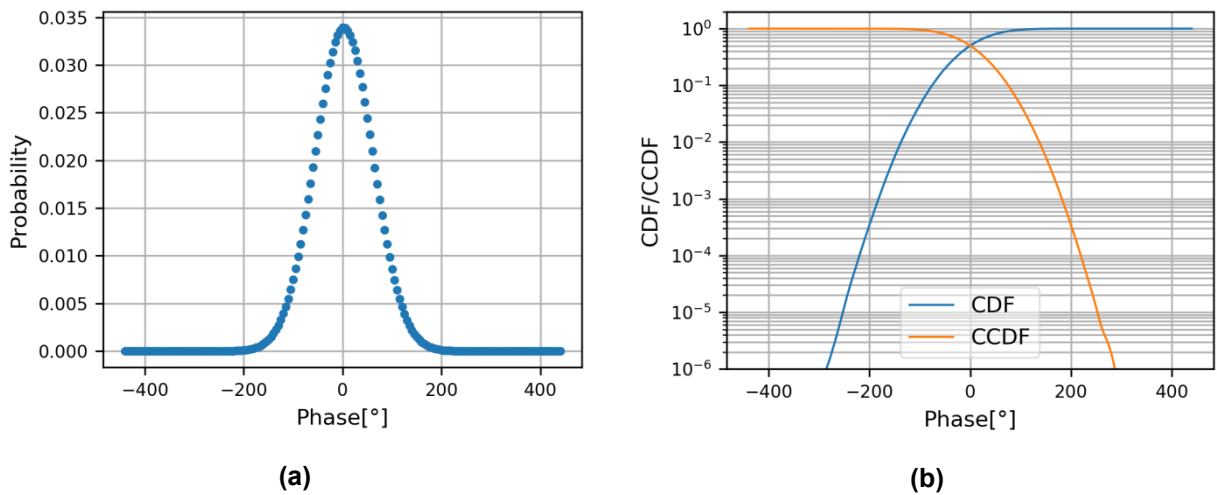
Figure 5.3: (a) PMF and (b) CDF/CCDF of histogram analysis of critical mask for f$_s$ = 40 MHz (42·10^9 samples)

5.1.1.2. VSAT P2 Mask

For the VSAT P2 mask, a bin resolution of 0.5° has been chosen. The ranges have been selected as ±45° to include all occurring samples and allow for a comparison with the filter-based method in Section 5.3.1. Once again, the expectation μ is in the order of 10^{-4} and can therefore be approximated to 0 when accounting for numerical errors and a finite number of observed samples.

An example time series is given in Figure 5.4 for this PN mask as well. The same parameters of length of 0.1s and $f_s = 400\,\text{kHz}$ have been chosen to facilitate comparisons. It has to be noted that the y-axis scaling is different from Figure 5.1; therefore, care has to be taken when directly comparing the two figures.
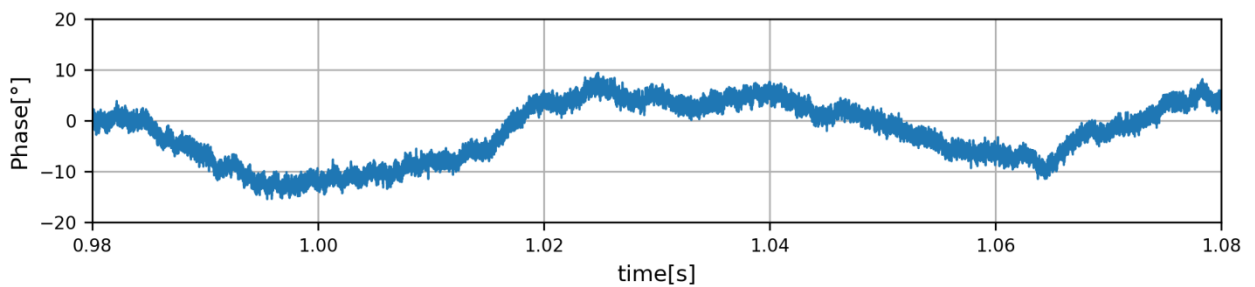
Figure 5.4: Time series of PN samples created from VSAT P2 PN mask for f$_s$ = 400 kHz

For $f_s = 400\,\text{kHz}$, the standard deviation is $\sigma = 7.19°$. PMF and CDF as well as CCDF can be found in Appendix A.1 in Figure A.1 (a) and (b), respectively.

For $f_s = 40\,\text{MHz}$, the standard deviation is $\sigma = 7.30°$. PMF and CDF as well as CCDF can be found in Figure 5.5 (a) and (b), respectively. Once again the PMF resembles a zero-mean Gaussian distribution. It should be noted however, that despite the visual similarity to Figure 5.2 and Figure 5.3, the bin ranges are different by a factor of 10, therefore the only comparison that can be made between both masks is that PN samples generated using the VSAT P2 mask are approximately 10 times smaller in magnitude than those created with the critical PN mask.

(a) (b)
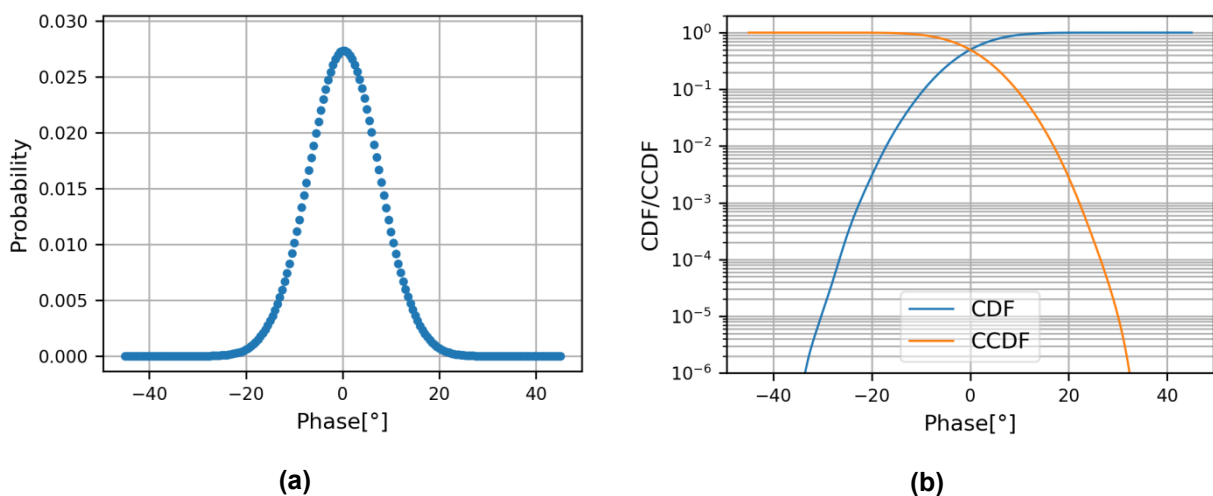
Figure 5.5: (a) PMF and (b) CDF/CCDF of histogram analysis of VSAT P2 mask for f$_s$ = 40 MHz (42·10^9 samples)

5.1.1.3. Transponder Mask

Once again, an exemplary time series plot with the same parameters of 0.1s and $f_s = 400\,\text{kHz}$ is given in Figure 5.6. For the transponder PN mask, the y-axis had to be adjusted to ±3° for the occurring samples. In this case, the first noticeable difference is that higher frequencies seem to play a bigger impact than lower ones compared to the VSAT P2 mask time series in Figure 5.4.
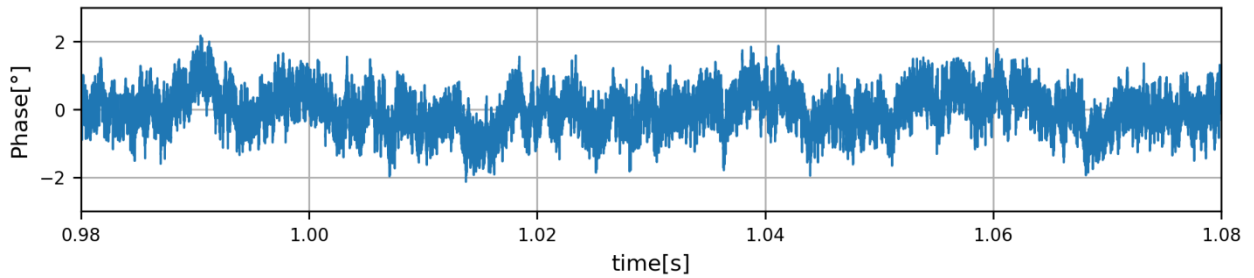
Figure 5.6: Time series of PN samples created from transponder PN mask for f$_s$ = 400 kHz

The bin resolution for the transponder mask has been selected as 0.05° in accordance with the reasoning stated in the previous sections. The ranges are selected as ±4°. The assertion that $\mu \approx 0$ can be supported by the measured values in the order of 10^{-5} in this case.

For $f_s = 400\,\text{kHz}$, the standard deviation is $\sigma = 0.578°$. PMF and CDF as well as CCDF can be found in Appendix A.1 in Figure A.2 (a) and (b), respectively.

(a) (b)
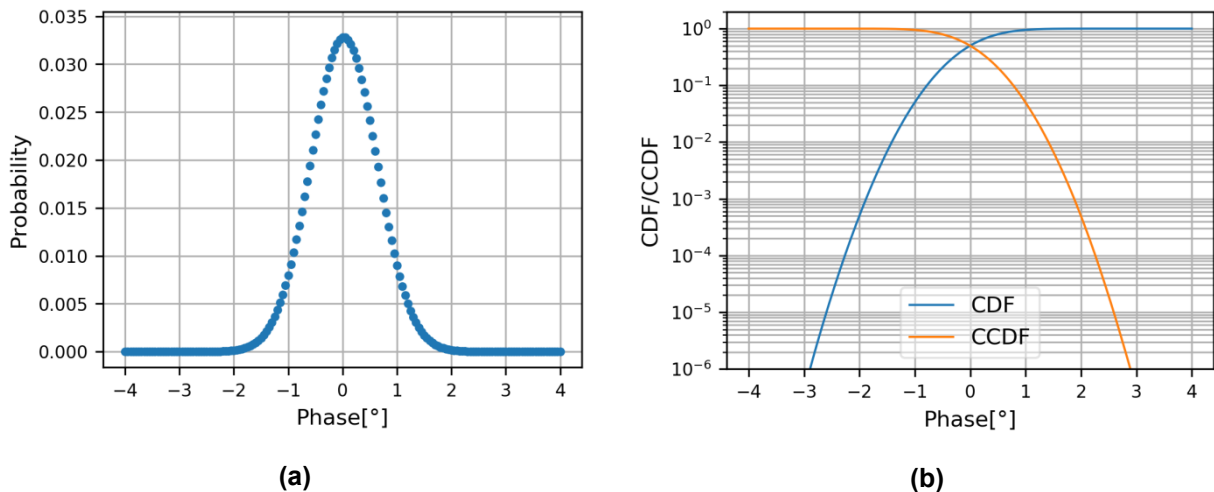
Figure 5.7:(a) PMF and (b) CDF/CCDF of histogram analysis of transponder mask for f$_s$ = 40 MHz (42·10^9 samples)

For $f_s = 40\,\text{MHz}$, the standard deviation is $\sigma = 0.608°$. PMF and CDF as well as CCDF can be found in Figure 5.7 (a) and (b), respectively. For the transponder masks, slight differences in the maximally occurring PN sample magnitude as well as the standard deviation σ have to be noted, as σ is roughly 5% larger for the $f_s = 40\,\text{MHz}$ case. This can be explained by the relatively larger influence of the higher frequencies that are included in the analysis with $f_s = 40\,\text{MHz}$. Due to the values of the transponder PN mask being much lower for frequencies <200 kHz compared to the previously analyzed masks, the higher frequencies have a larger influence on the overall

samples. This leads to a broader CDF/CCDF plot in Figure 5.7b compared to the plot for $f_s = 400\,\text{kHz}$ in Figure A.2b and therefore an occurrence of PN samples that are of larger absolute value.

Compared to PN samples created using the VSAT P2 mask, the overall magnitude of the phase is approx. another 10 times smaller. Again, this makes comparing the results from the two PN masks in one plot very difficult and is therefore not attempted. However, the fact should be noted because of the similar appearance of the plots due to the chosen ranges and bin resolutions.

5.1.1.4. Differential Mask

For the differential PN mask, the example time series is given in Figure 5.8 over a larger timeframe of 1.5s in order to visualize the lower frequencies better. The sampling frequency is still $f_s = 400\,\text{kHz}$ and the y-axis is limited to even smaller values of ±0.15°.
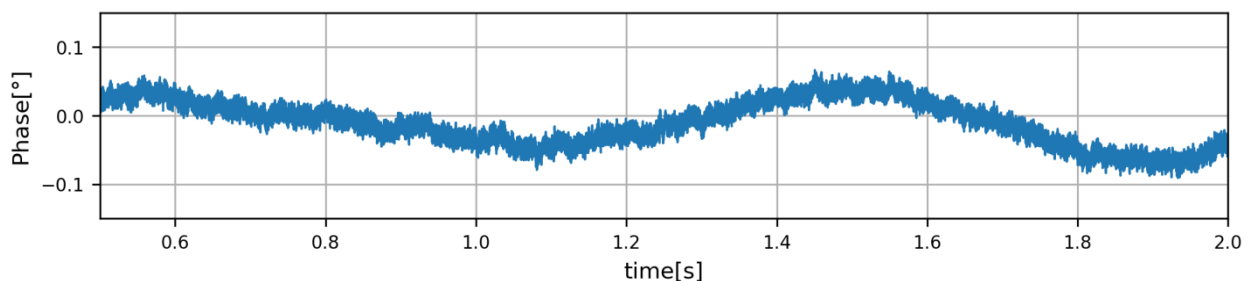
Figure 5.8: Time series of PN samples created from transponder PN mask for f$_s$ = 400 kHz

The bin resolution for the differential mask has been set to 0.002° due to the small overall phase noise contribution. As in the above sections, the ranges have been set to include all samples and are chosen as ±0.17°. The measured values for the expectation μ are in the order of 10^{-7} for this mask, therefore the aforementioned assumption of $\mu \approx 0$ is even more strongly supported through the analysis of this mask.

(a)

(b)
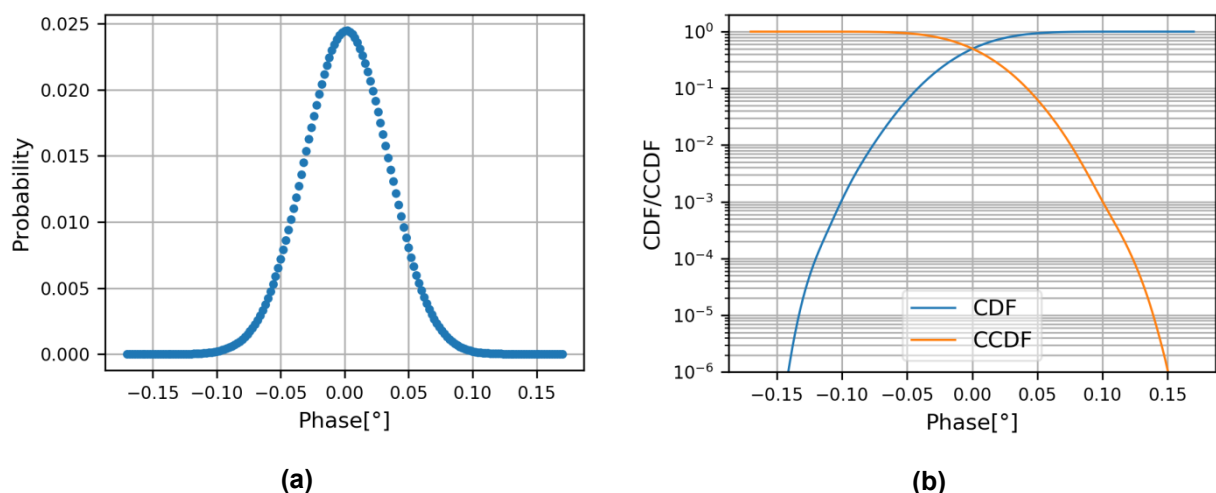
Figure 5.9: (a) PMF and (b) CDF/CCDF of histogram analysis of differential mask for f$_s$ = 4 MHz (42·10^9 samples)

For $f_s = 400\,\mathrm{kHz}$, the standard deviation is $\sigma = 0.032°$. PMF and CDF as well as CCDF can be found in Appendix A.1 in Figure A.3 (a) and (b), respectively.

For $f_s = 4\,\mathrm{MHz}$, the standard deviation is $\sigma = 0.033°$. PMF and CDF as well as CCDF can be found in Figure 5.9 (a) and (b), respectively. The same effects as already described for the transponder mask can be observed here as well. Despite σ being close to identical, a broadening of the CDF/CCDF plots can be seen between Figure A.3b and Figure 5.9b here as well.

Compared to the case of the transponder PN mask, the absolute values of resulting PN samples generated with the differential mask are roughly 20 times smaller, leading to a factor of approx. $2 \cdot 10^3$ when comparing the absolute values of PN samples created using the critical mask with those created using the differential mask.

To portray the effect of a non-sufficient frequency resolution in terms of covering all specified frequency points of the PN mask, the differential mask is also simulated at $f_s = 40\,\mathrm{MHz}$ for an FFT length of $N = 2^{23}$, leading to a frequency resolution of 4.77 Hz compared to the first specified PN mask point at 1 Hz for the differential mask. The range between 1 Hz and 10 Hz is therefore represented by only two points at 4.77 Hz and 9.54 Hz.

It can clearly be seen in Figure 5.10 (a) and (b) that the lacking frequency resolution in the lower frequency spectrum leads to a misrepresentation of the phase noise due to the drastically lower absolute values of the PN samples compared to the $f_s = 4\,\mathrm{MHz}$ case. The standard deviation is only $\sigma = 0.011°$, i.e. approx. 66% lower than in the $f_s = 4\,\mathrm{MHz}$ case.

This simulation also shows that the lower frequencies, due to being specified with the comparatively highest dBc/Hz values in the PN masks have the largest impact on the statistical analysis in the time domain. It should be noted that in further simulations, it will be shown that this is not the case for all different types of analyses. However, this case is just meant to illustrate the effect of choosing a non-sufficient frequency resolution for the IFFT-based PN generation method as described in Section 3.1 and will not be referenced further.

(a)   (b)
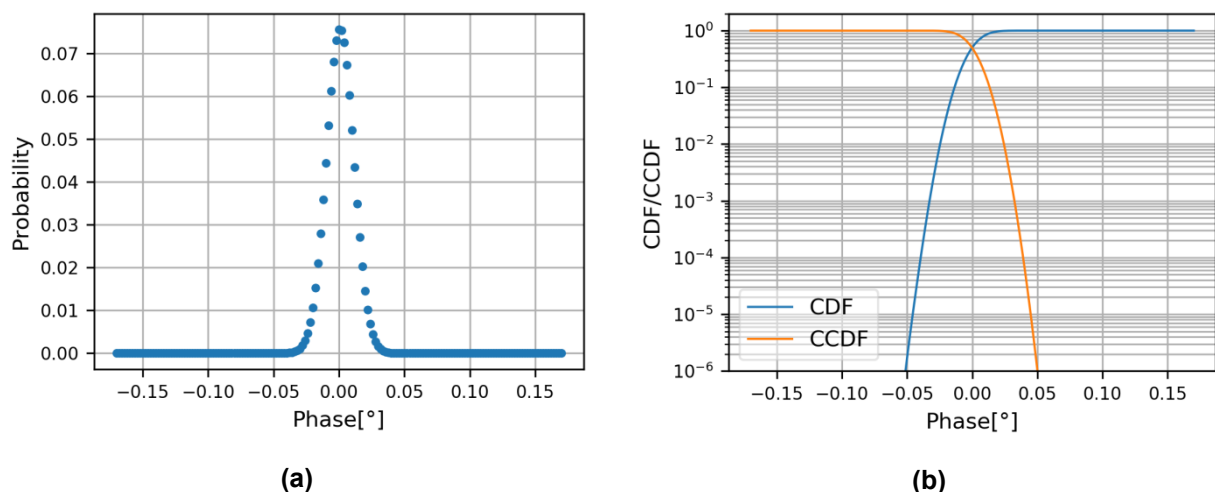
Figure 5.10: (a) PMF and (b) CDF/CCDF of histogram analysis of differential mask for f$_s$ = 40 MHz (42·10^9 samples)

5.1.2. Statistical Analysis of Random Walk

For the random walk analysis, not every sample, but each sample after a period of 100 ms for $f_s = 400\,\text{kHz}$, and conversely 1 ms for $f_s = 40\,\text{MHz}$, is taken into consideration for the calculation of the statistical properties. This is supposed to show the statistics of the phase noise when taking into account longer periods of phase drift. A graphical example of this process for one set of noise samples generated using the VSAT P2 mask can be found in Figure 4.4.

The periods of 100 ms and 1 ms for the two sampling frequencies are chosen arbitrarily, yet from a practical standpoint have to be close enough together so that a reasonable simulation time can be achieved. As an example, using the sampling period of 100ms with PN samples created with $f_s = 400\,\text{kHz}$, 1 sample in 40 000 created samples is used, meaning that more than 99.99% of samples have to be discarded. If a reasonable amount of samples at least greater than 1 million is required for the statistical analysis, choosing an even larger period between two subsequent samples would lead to an unreasonably large number of total samples that need to be simulated. Furthermore, with the realization of DVB-S2X waveforms in mind, the length of a superframe within that structure is 60 ms for a baud rate of 10 MSymbols/s and conversely 6 ms for 100 MSymbols/s, meaning that the chosen periods are within the same order of magnitude.

To verify this analysis method, the same procedure is performed for the VSAT P2 mask for an ensemble of realizations each sampled once time instance $t = 100\,\text{ms}$. That means that for every sample taken into account in the analysis, a completely new set of AWGN samples is used and each FFT/IFFT operation as described in Section 3.1 yields only one single PN sample for the analysis. The results are found in Section 5.1.2.2.

Due to using the same statistical tools of mean value μ, standard deviation σ, PMF, and CDF as well as CCDF as in Section 5.1.1, a comparison between the results can give insight into the time-properties of the phase noise process.

For $f_s = 400\,\text{kHz}$, a time series of overall length of 327 680 s, or 91 hours, has been sampled every 100 ms, leading to 3 276 800 overall resulting samples.

For $f_s = 40\,\text{MHz}$, the overall length of the time series is reduced to 8 388.6 s, or approx. 2 hours 20 min, which has been sampled every 1 ms, leading to 8 388 654 overall analyzed samples.

For the special case of the differential PN mask, the high sampling frequency has once again been adjusted to $f_s = 4\,\text{MHz}$ in order to portray the phase noise mask fully, as demonstrated in Section 5.1.1.4. This leads to an overall time series length of 83 886.1 s, or approx. 23 hours, but due to the sampling at every 10 ms, the overall number of samples remains at 8 388 654 as in the case of $f_s = 40\,\text{MHz}$.

Overall, fewer samples are included in the analysis compared to Section 5.1.1 due to the practical limitations described above, but the results are still comparable up to an accuracy of 10^{-4} in terms of probability.

5.1.2.1. Critical Mask

In order to keep the results comparable to the previous section, the same bin ranges and resolutions have been chosen for all simulations. For the critical mask, the bin resolution is 5° with a range of ±440°.

For $f_s = 400\,\text{kHz}$, the standard deviation is $\sigma = 58.98°$, very similar in value to the results from the previous section. PMF and CDF as well as CCDF can be found in Figure 5.11 (a) and (b), respectively.

As can be seen in comparison to Figure 5.2b, CDF and CCDF are very similar up to 10^{-5}, after that the lower number of points in the random walk analysis leads to some inconsistencies which could only be overcome by increasing the simulation time by a factor of at least 100.

This suggests that the random PN process created with the IFFT-based method is at least wide-sense stationary. However, to make a more substantiated claim, more detailed investigations into this topic would be necessary, which were out of scope for this thesis.

(a)   (b)
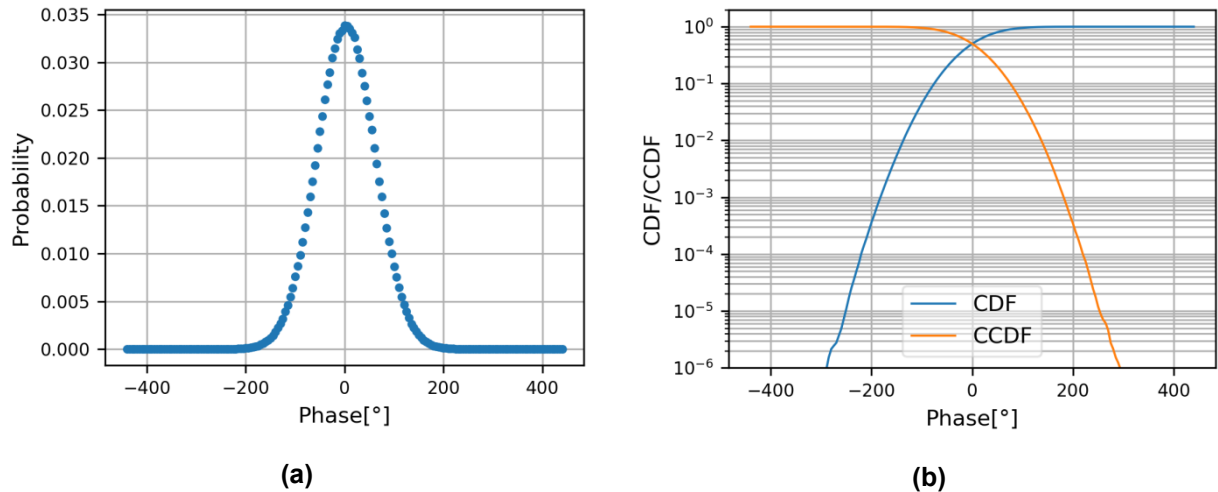
Figure 5.11: (a) PMF and (b) CDF/CCDF of random walk analysis of critical mask for f_s = 400 kHz ($3.2 \cdot 10^6$ samples)

For $f_s = 40$ MHz, the standard deviation is $\sigma = 59.01°$. Again, this value is very similar to that from Section 5.1.1.1, further emphasizing the similarities of results between both analysis methods. PMF and CDF as well as CCDF can be found in Figure 5.12 (a) and (b), respectively and show the same similarity to Figure 5.3 that has already been stated above. It should once again be noted that for y-axis values smaller than 10^{-4}, the CDF and CCDF plots are not accurate anymore due to the number of simulated samples.

(a)   (b)
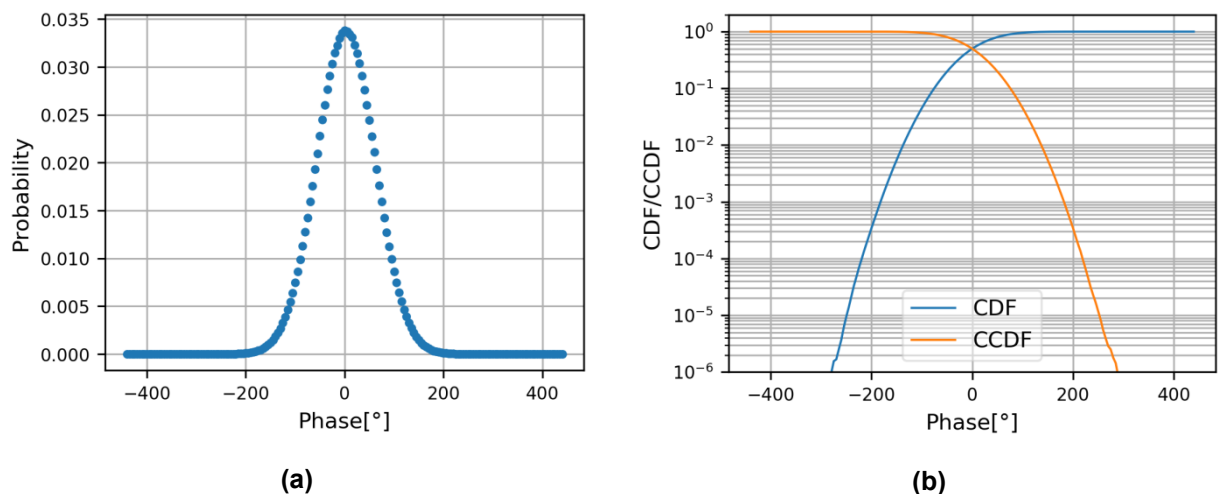
Figure 5.12: (a) PMF and (b) CDF/CCDF of random walk analysis of critical mask for f_s = 40 MHz ($8.3 \cdot 10^6$ samples)

5.1.2.2. VSAT P2 Mask

The bin ranges for the VSAT P2 mask are ±45° with a resolution of 0.5°.

For $f_s = 400\,\mathrm{kHz}$, the standard deviation is $\sigma = 7.18°$. PMF and CDF as well as CCDF can be found in Figure 5.13 (a) and (b), respectively. Analog to the critical mask, the comparison to Figure A.1 and the variance given in Section 5.1.1.2 again show the close similarities of both methods up to values of 10^{-4}.
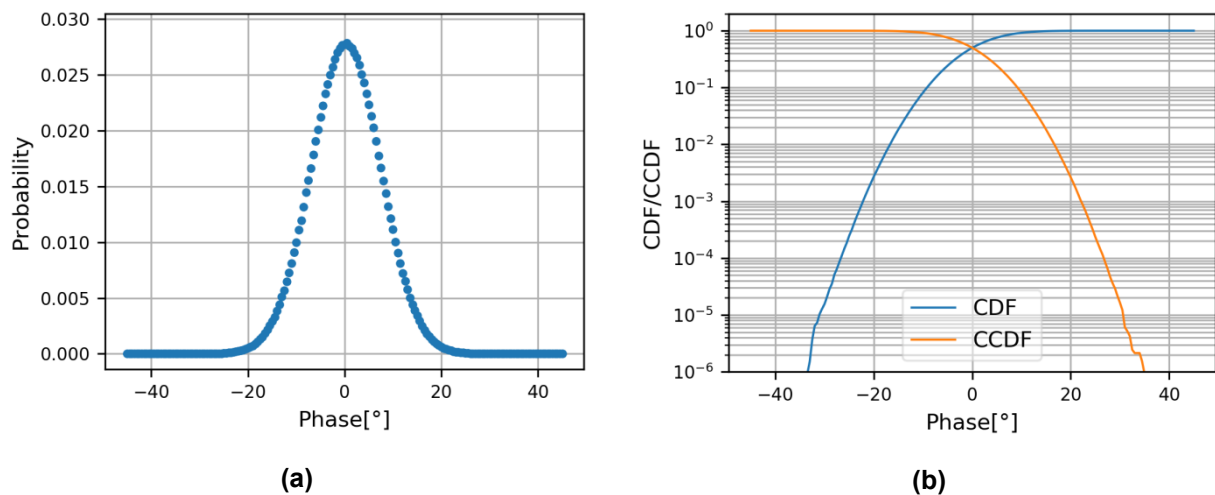
Figure 5.13: (a) PMF and (b) CDF/CCDF of random walk analysis of VSAT P2 mask for f$_s$ = 400 kHz (3.2·10^6 samples)

Furthermore, as mentioned in the introduction to this section, the random walk values are compared to independently generated realizations of the PN process where only one value at time instance $t = 100\,\mathrm{ms}$ is taken per block of generated PN samples, corresponding to an analysis of an ensemble of realizations of the process. Because of the additional computational complexity of this method (instead of using 1 out of 40 000 samples for analysis, here only 1 out of every 524 288 samples is used), only 100 000 samples could be generated in this way within the limits of reasonable computational complexity. The PMF and CDF/CCDF plots can be found in Figure 5.14 (a) and (b), respectively.

Due to the relatively low amount of overall samples, the CDF values are only accurate up to 10^{-3}, but the results of both PMF and CDF are suggesting both methods to be equivalent.

This leads to the hypothesis that the IFFT-based PN generation yields an ergodic PN process, as the statistical properties of multiple realizations of the process sampled at the same time instant are preserved if one realization of the process is taken and sampled at multiples of that time interval. This hypothesis is only valid if the claim of wide-sense stationarity from the previous section is valid as well, therefore it should once again be noted that further detailed investigations into this topic would be necessary to confirm these hypotheses, which was out of scope for this thesis.
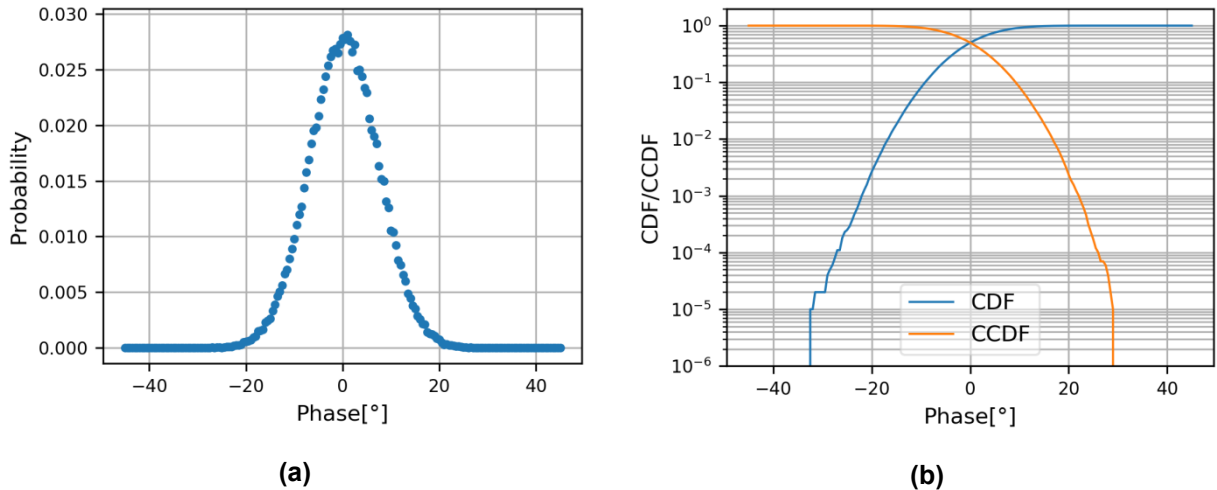
Figure 5.14: (a) PMF and (b) CDF/CCDF of ensemble-based random walk analysis of VSAT P2 mask at t = 100 ms for f_s = 400 kHz (100 000 samples)

For $f_s = 40\,\text{MHz}$, the standard deviation is $\sigma = 7.30°$. PMF and CDF as well as CCDF can be found in Figure 5.15 (a) and (b). As previously discussed, the similarities to Figure 5.5 in Section 5.1.1.2 are apparent here as well.
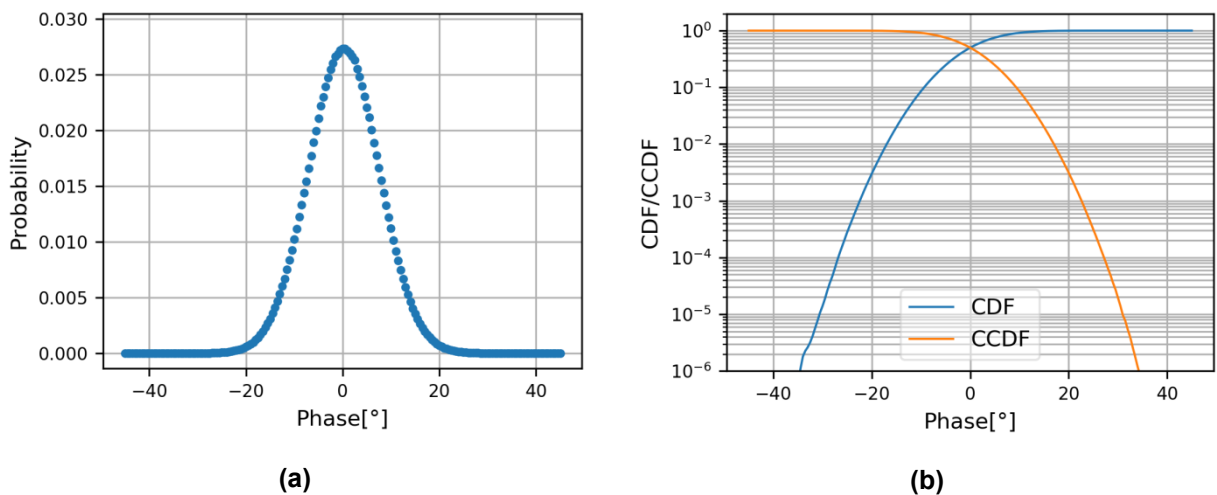
Figure 5.15: (a) PMF and (b) CDF/CCDF of random walk analysis of VSAT P2 mask for f_s = 40 MHz (8.3·10^6 samples)

It has been shown for the phase noise process that an analysis of all samples over an arbitrary time frame yields the same results as sampling the process at an arbitrary interval and taking all the resulting samples for analysis independent of the selected PN mask by analyzing both the critical and the VSAT P2 masks. Furthermore, the ergodicity of the PN process has been suggested by analyzing how one instance of the process sampled at arbitrary points corresponds to many realizations sampled once, in this case for the VSAT P2 mask. Further results are not explicitly given here, as they are just a repetition of the results from Section 5.1.1. It is however remarked that both the transponder and differential mask lead to the same results, which can be found in Appendix A.2.

5.2. Spectral Analysis

This chapter comprises the results from the IFFT phase noise generation method in the frequency domain. For this purpose, a sine carrier has been impaired with phase noise and then transformed into the frequency domain via FFT.

The resulting spectrum is then compared to the original PN mask, which should be identical at all frequency bins that do not contain carrier influence, i.e. as the carrier frequency is always selected as exactly the first frequency bin (0.76 Hz in the $f_s = 400\,\text{kHz}$ case, 4.77 Hz in the $f_s = 40\,\text{MHz}$ case), the PN generation method is working flawlessly if all bins except the first one are identical to the selected PN mask. The amplitude of the carrier is set to 1 V, therefore the bin containing the carrier power is expected to be 0 dBV.

As the original masks are defined in units of dBc/Hz in Section 2.3, the obtained values in this simulation have to be adjusted for 1 Hz bandwidth and expressed in units of dBc. This analysis method therefore serves as a verification method for the overall functionality of the PN generation method, and the deviation of the measured dBc spectrum compared to the original PN mask serves as a measurement of quality of results.

For the purpose of this simulation, the FFT lengths have been chosen as 2^{19} and 2^{23} for sampling frequencies of $f_s = 400\,\text{kHz}$ and $f_s = 40\,\text{MHz}$ respectively. This leads to frequency resolutions of 0.76 Hz and 4.77 Hz for the two cases. The frequency resolutions are chosen identically for both the FFT/IFFT operation in the creation of PN samples as well as the spectral analysis module to avoid aliasing. The choice of carrier frequency is based on the same explanation.

Due to the different specification frequencies of the differential mask, the sampling frequencies have been chosen slightly differently to accurately reproduce the entire mask. Since a frequency resolution smaller than 1 Hz is needed in both cases to accurately represent the 1 Hz point defined in the mask, $f_s = 4\,\text{MHz}$ is used for an FFT length of 2^{23} just like in the previous sections for the statistical analysis, leading to a frequency resolution of 0.48 Hz. The carrier frequency is adjusted in similar fashion for this case to match the first frequency bin and avoid aliasing.

In order to obtain the dBc/Hz values found in the result tables, the raw FFT output has to be adjusted as described in Section 2.2.2. Because of the chosen frequency resolution, the dBc values cannot be measured for the exact frequencies defined in the mask specifications (e.g. the 100 Hz point can be measured at 99.95 Hz or 100.7 Hz for 0.76 Hz frequency resolution). Therefore, the closest point in the respective frequency resolution (99.95 Hz in the aforementioned example) has been chosen to represent each value, resulting in a small error due to frequency quantization. This can be exemplified for the 1 Hz point of the differential mask, where the next closest available FFT frequency bin is located at 1.52 Hz (taking into account that the first bin at 0.76 Hz contains the entire carrier power), so a quantization error of $1.52\,\text{Hz} - 1\,\text{Hz} = 0.52\,\text{Hz}$ occurs. The smaller the chosen frequency resolution is, the smaller this error will be, however it is necessary to keep in mind the tradeoff between result accuracy and computational complexity due to large FFT lengths.

Furthermore, as the well-known Nyquist theorem states, frequency values greater than $f_s/2$ cannot be computed, therefore those values are left blank for $f_s = 400\,\text{kHz}$. Wherever the highest frequency point in the specified PN mask was lower than the Nyquist frequency, an AWGN-like noise has been assumed for the frequencies greater than the last point in the mask, which is consistent with most mask definitions in [1], [2], [9], and [14]. This AWGN-like noise is expressed as a flat horizontal line in the spectrum, which is especially prominent for the transponder mask, where the highest specified mask frequency is only 1 MHz.

All results were obtained by averaging over 50 000 iterations of bursts of data equal in length to the FFT to facilitate the FFT calculation. This means that for each burst, 2^{19} or 2^{23} PN samples were generated that were subsequently used to impair the carrier waveform.

5.2.1. Critical Mask

The carrier bin at 0.76 Hz is different from 0 dB by an attenuation of 4.58 dB for $f_s = 400\,\mathrm{kHz}$. Conversely, in the $f_s = 40\,\mathrm{MHz}$ case, the carrier bin at 4.77 Hz is attenuated by 4.51 dB, leading to the observation that phase noise influences the carrier bin significantly. In Table 5.1, the measured values at the frequencies specified in the PN mask definition are shown in units of dBc/Hz. It can easily be seen that a high deviation from the specified mask values is obtained for frequencies greater than 1 kHz, which is in the range of the carrier attenuation specified above.

It is likely that this carrier attenuation caused by PN contributions at the carrier frequency itself is the cause of this phenomenon, leading to a conclusion that the verification of the PN mask via the results of the spectral analysis is not possible in this case.

Frequency	Mask [dBc/Hz]	Measured values [dBc/Hz] f_s = 400 kHz	Measured values [dBc/Hz] f_s = 40 MHz
10 Hz	-25	-23.206	-23.241
100 Hz	-25	-23.450	-23.571
1 kHz	-50	-45.180	-45.111
10 kHz	-73	-68.408	-68.304
100 kHz	-83	-78.397	-78.484
1 MHz	-103		-98.486
10 MHz	-114		-109.488

Table 5.1: Critical mask dBc values for f_s = 400 kHz and f_s = 40 MHz

To further investigate the relationship between carrier attenuation and deviation from the specified mask, the absolute dB values are regarded in Table 5.2, virtually setting carrier attenuation to 0 dB. It can be seen that for frequencies greater 1 kHz the results fit the specified mask with deviations less than 0.4 dB, inferring that, as suspected, phase noise at the carrier frequency is responsible for the large dBc deviations.

Frequency	Mask [dBc/Hz]	Measured values [dB/Hz] f_s = 400 kHz	Measured values [dB/Hz] f_s = 40 MHz
10 Hz	-25	-27.787	-27.749
100 Hz	-25	-28.031	-28.080
1 kHz	-50	-49.761	-49.619
10 kHz	-73	-72.989	-72.813
100 kHz	-83	-82.978	-82.993
1 MHz	-103		-102.995
10 MHz	-114		-113.997

Table 5.2: Critical mask dB values for f_s = 400 kHz and f_s = 40 MHz

The resulting spectra are plotted in units of dBc/Hz and compared to the PN mask in Figure 5.16 and Figure 5.17 for $f_s = 400\,\text{kHz}$ and $f_s = 40\,\text{MHz}$, respectively. The deviation of the carrier bin from 0 dB at 0.76 Hz/4.77 Hz for the respective sampling frequency can be seen clearly, as well as the constant offset this carrier attenuation causes for higher frequencies, which is logical given that the carrier power subtracted from the dB values according to Eq. (2.18) is approx. 4.5 dB lower than it should be if the carrier tap was unaffected by PN.
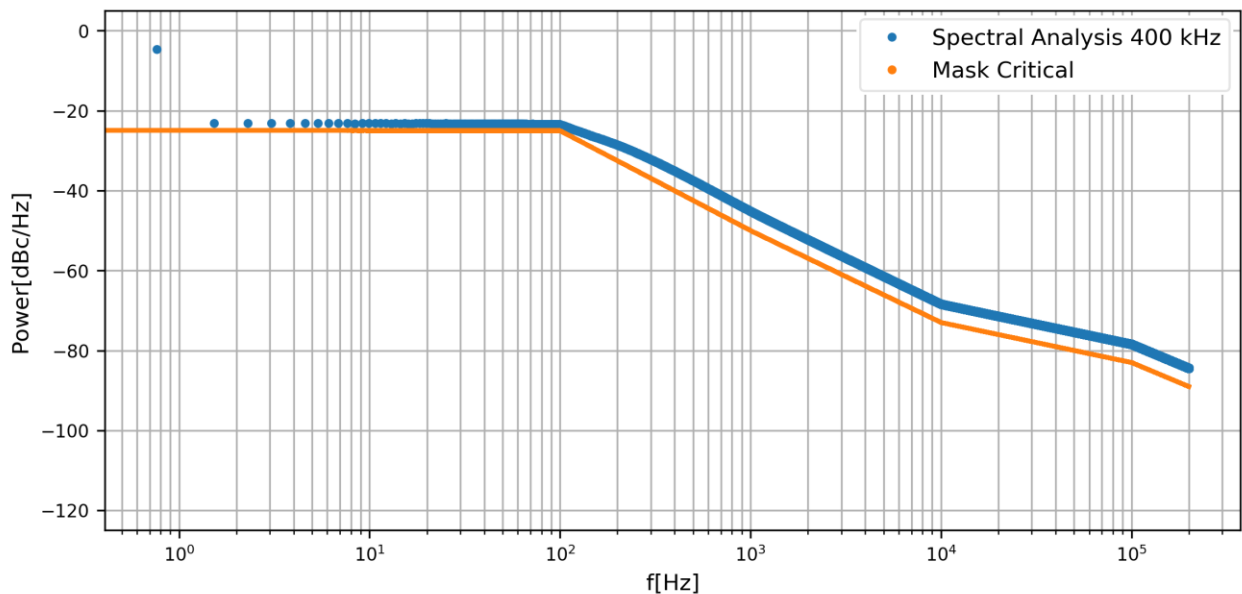
Figure 5.16: Spectrum of PN-impaired sine wave for critical mask, avg. over 50 000 iterations (blue), compared to the critical PN mask (orange), f_s = 400 kHz, carrier bin at 0.76 Hz
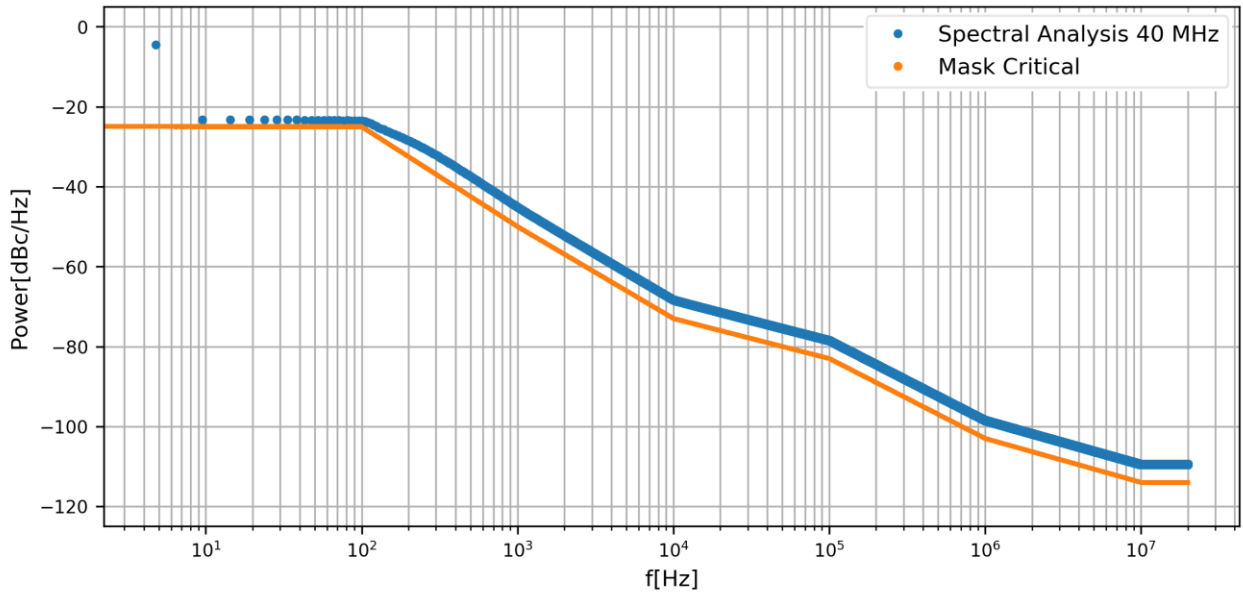
Figure 5.17: Spectrum of PN-impaired sine wave for critical mask, avg. over 50 000 iterations (blue), compared to critical PN mask (orange), f$_s$ = 40 MHz, carrier bin at 4.77 Hz

5.2.2. VSAT P2 Mask

In case of the VSAT P2 mask, the carrier attenuation is observed at -0.07 dB for $f_s = 400\,\text{kHz}$ and -0.06 dB at $f_s = 40\,\text{MHz}$, meaning that compared to the critical PN mask, the influence of the PN impairment on the carrier bin is lower by a factor of 10^{-2}. Therefore, this effect plays a significantly less important role for the VSAT P2 mask. The resulting dBc values match the specified mask to approx. 1 dB difference with one exception, the largest deviation of 2.58 dB at 100 Hz for $f_s = 40\,\text{MHz}$, as can be seen in Table 5.3.

Frequency	Mask [dBc/Hz]	Measured values [dBc/Hz] f$_s$ = 400 kHz	Measured values [dBc/Hz] f$_s$ = 40 MHz
10 Hz	-33	-33.033	-33.113
100 Hz	-62	-61.449	-59.416
1 kHz	-79	-78.730	-77.703
10 kHz	-89	-88.920	-88.819
100 kHz	-95	-94.921	-94.924
1 MHz	-105		-104.924
10 MHz	-115		-114.927

Table 5.3: VSAT P2 mask dBc values for f$_s$ = 400 kHz and f$_s$ = 40 MHz

The resulting spectra in units of dBc/Hz are compared to the mask profile in Figure 5.18 and Figure 5.19 for $f_s = 400\,\text{kHz}$ and $f_s = 40\,\text{MHz}$, respectively. Taking into account only the $f_s = 400\,\text{kHz}$ case in Figure 5.18, the results verify the high accuracy of the PN creation method, as

the deviation from the mask is lower than 1 dB across all frequencies, which also supports the results from Table 5.3. The $f_s = 40\,\mathrm{MHz}$ case in Figure 5.19 shows that the same results cannot be obtained regardless of the choice of sampling frequency, as the frequency regions between 10 Hz and 1 kHz show a misrepresentation with a maximum deviation of 4 dB for the 14.3 Hz point.
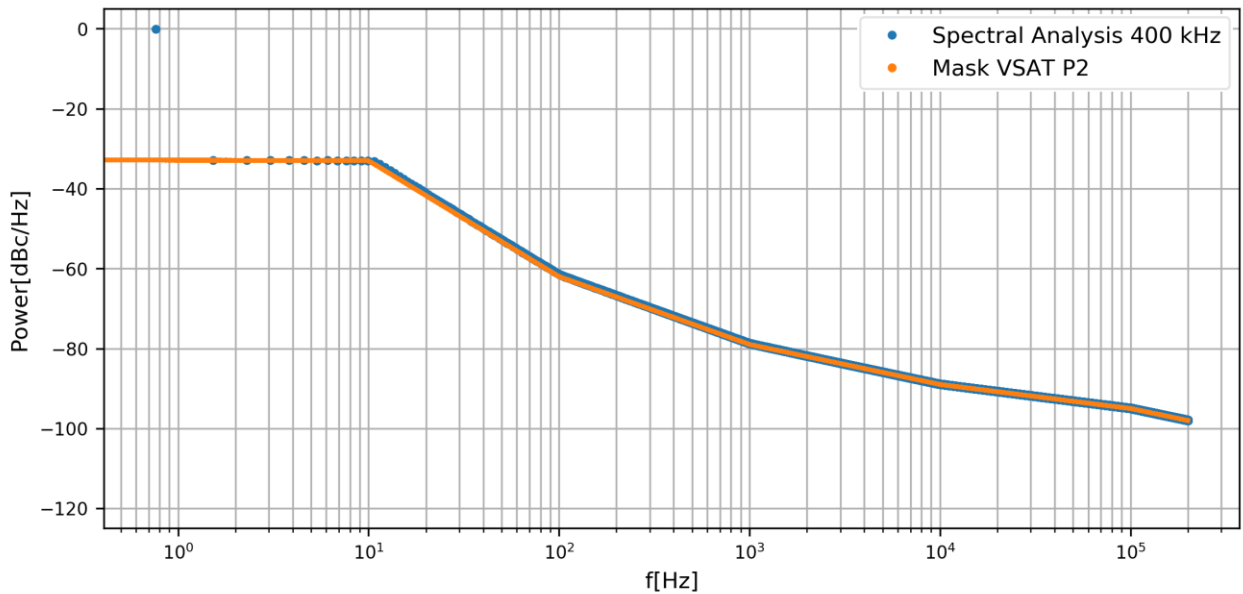
Figure 5.18: Spectrum of PN-impaired sine wave for VSAT P2 mask, avg. over 50 000 iterations (blue), compared to the VSAT P2 PN mask (orange), f$_s$ = 400 kHz, carrier bin at 0.76 Hz
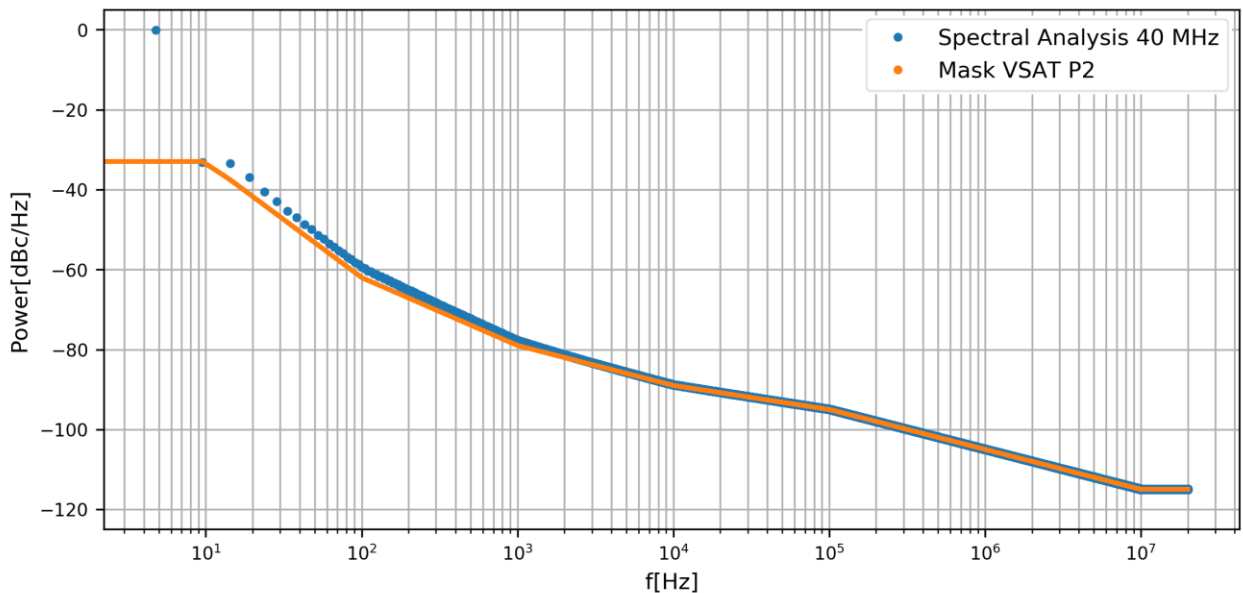
Figure 5.19: Spectrum of PN-impaired sine wave for VSAT P2 mask, avg. over 50 000 iterations (blue), compared to VSAT P2 PN mask (orange), f$_s$ = 40 MHz, carrier bin at 4.77 Hz

This deviation is investigated more closely in Figure 5.20, where the results from both $f_s = 400\,\text{kHz}$ and $f_s = 40\,\text{MHz}$ case are compared to the PN mask profile focused on the frequency region between 10 Hz and 100 Hz.
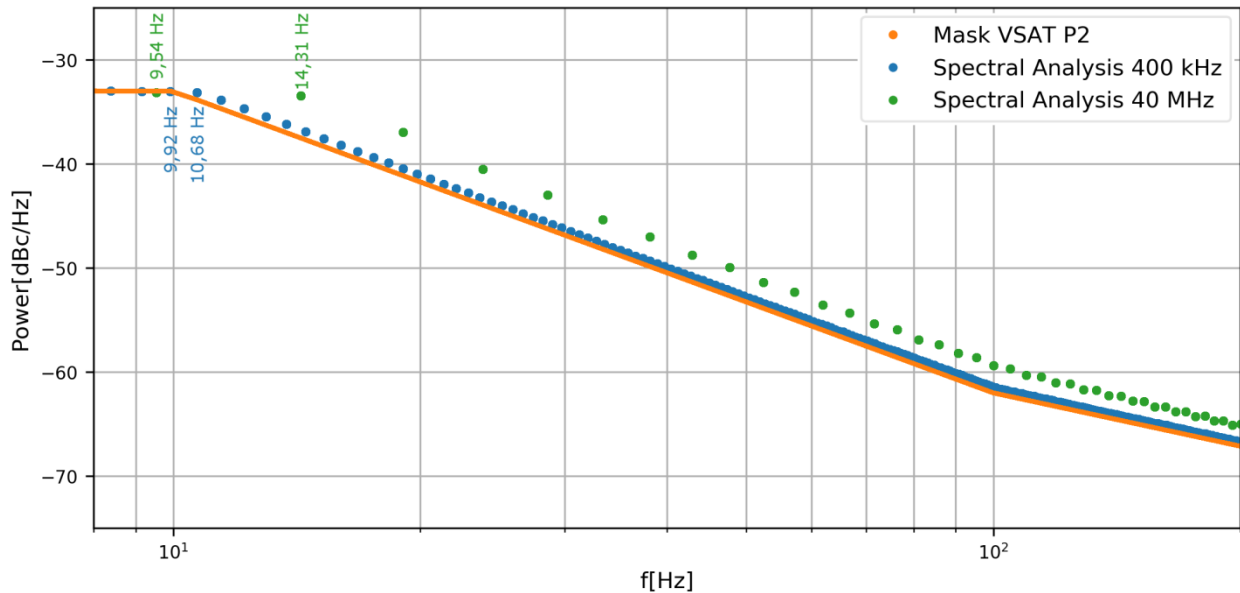
Figure 5.20: Comparison of spectral analysis results of VSAT P2 mask for both f_s = 400 kHz (blue) and f_s = 40 MHz (green) with VSAT P2 PN mask profile (orange) between 10 Hz and 100 Hz

It can be observed that due to the differing frequency resolutions of 0.76 Hz in the $f_s = 400\,\text{kHz}$ case and 4.77 Hz in the $f_s = 40\,\text{MHz}$ case, the relevant frequency points around 10 Hz are spaced out differently, as denoted in the figure. The point at 14.31 Hz includes a lot more energy than it should if the results were approaching the mask profile, but there are no other bins that the energy could be distributed into, which leads to errors in this bin as well as subsequent bins. Only as the frequencies rise and the frequency resolution becomes less impactful does the green curve approach the reference mask again. It is therefore hypothesized that this energy accumulation by the FFT is the cause of the deviations in the $f_s = 40\,\text{MHz}$ case for this mask and the following. This leads back to the tradeoff between result accuracy and computational complexity in terms of FFT length, which directly influences frequency resolution, as discussed previously. If the application requires matching the specified PN masks over all frequency bins, it seems a frequency resolution that is approx. 1/10th of the lowest frequency in the mask, in this case approx. 1 Hz, or lower is required.

With this effect being explained for the case of the VSAT P2 mask, it is not explicitly described again in the following for the remaining PN masks. Therefore, only the $f_s = 40\,\text{MHz}$ spectra are given for PN masks in the following. Aside from the different frequency resolution, they contain more information as a higher Nyquist frequency results from the choice of sampling frequency, so that the information contained in the $f_s = 400\,\text{kHz}$ would be redundant. For completeness reasons, those plots are given in the Appendix.

5.2.3. Transponder Mask

For the transponder mask, the carrier attenuation (i.e. the deviation of the carrier bin from 0 dB) is virtually 0 dB for both sampling frequencies. All deviations from the specified mask are within 0.3 dB, with the largest deviation being 0.27 dB at 100 Hz for $f_s = 40\,\mathrm{MHz}$ due to the same effects already explained for the VSAT P2 mask. The detailed results are found in Table 5.4.

Frequency	Mask [dBc/Hz]	Measured values [dBc/Hz] f_s = 400 kHz	Measured values [dBc/Hz] f_s = 40 MHz
10 Hz	-63	-63.028	-63.050
100 Hz	-73	-72.948	-72.732
1 kHz	-83	-82.982	-83.000
10 kHz	-93	-93.032	-92.967
370 kHz	-112		-112.020
1 MHz	-128		-128.001

Table 5.4: Transponder mask dBc values for f$_s$ = 400 kHz and f$_s$ = 40 MHz

Analog to previous chapters, the resulting spectra compared to the PN mask can be found in Figure A.8 in Appendix A.3 and Figure 5.21 for the two sampling frequencies, respectively.
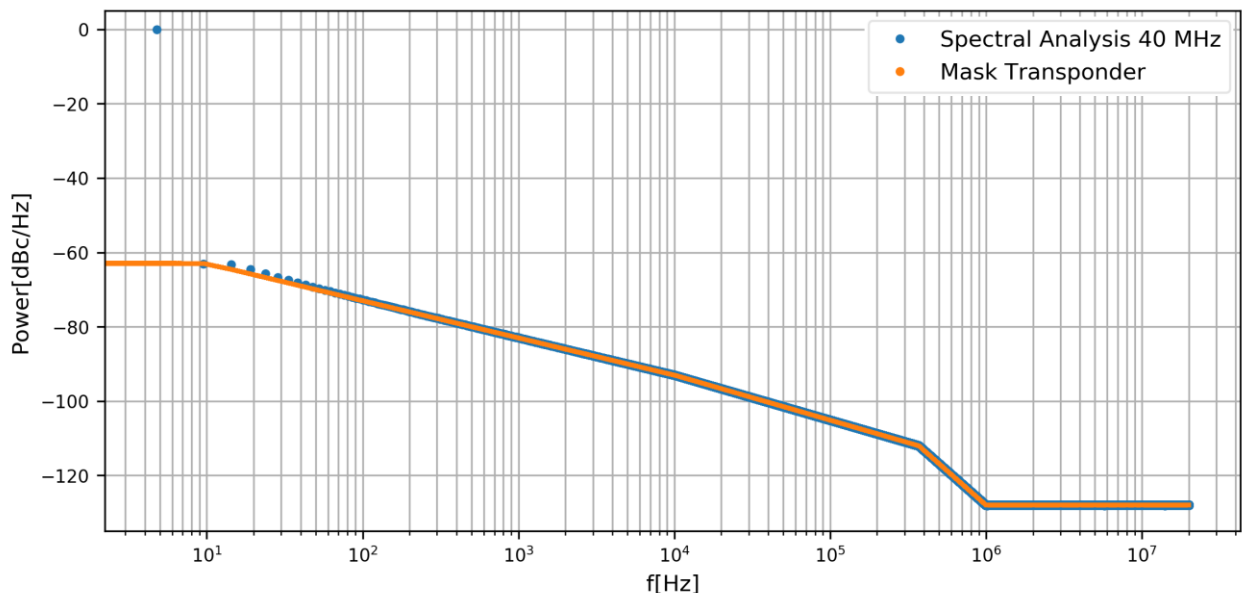
Figure 5.21: Spectrum of PN-impaired sine wave for transponder mask, avg. over 50 000 iterations (blue), compared to transponder PN mask (orange), f$_s$ = 40 MHz, carrier bin at 4.77 Hz

Analog to the VSAT P2 case, the point with the measured highest deviation is the 100 Hz point for $f_s = 40\,\mathrm{MHz}$, however the spectrum suggests that the largest deviation is once again located at the 14.31 Hz point. The deviation is lower in value to a point where it could be considered

negligible. It is suggested that the effect of insufficient frequency resolution as described in the VSAT P2 case is less severe due to the slope of the curve for the 10 Hz to 100 Hz segment being lower than for the VSAT P2 mask.

5.2.4. Differential Mask

The carrier attenuation for the differential mask is 0 dB for both $f_s = 400\,\text{kHz}$ and $f_s = 4\,\text{MHz}$. The maximum deviation is 4.8 dB and 2.9 dB at 10 Hz for both sampling frequencies respectively, and can be explained by the sparsity of frequency points in that region, equivalent to the explanation for the VSAT P2 mask. The remaining points show a maximum deviation of 0.56 dB and 0.36 dB respectively. All results are displayed in Table 5.5.

Frequency	Mask [dBc/Hz]	Measured values [dBc/Hz] f_s = 400 kHz	Measured values [dBc/Hz] f_s = 4 MHz
1 Hz	-70	-70.513	-70.094
10 Hz	-100	-95.243	-97.056
100 Hz	-110	-109.444	-109.643
1 kHz	-120	-119.944	-119.940
10 kHz	-130	-130.007	-129.994
100 kHz	-150	-149.983	-150.044
1 MHz	-160		-160.016

Table 5.5: Differential mask dBc values for f$_s$ = 400 kHz and f$_s$ = 4 MHz
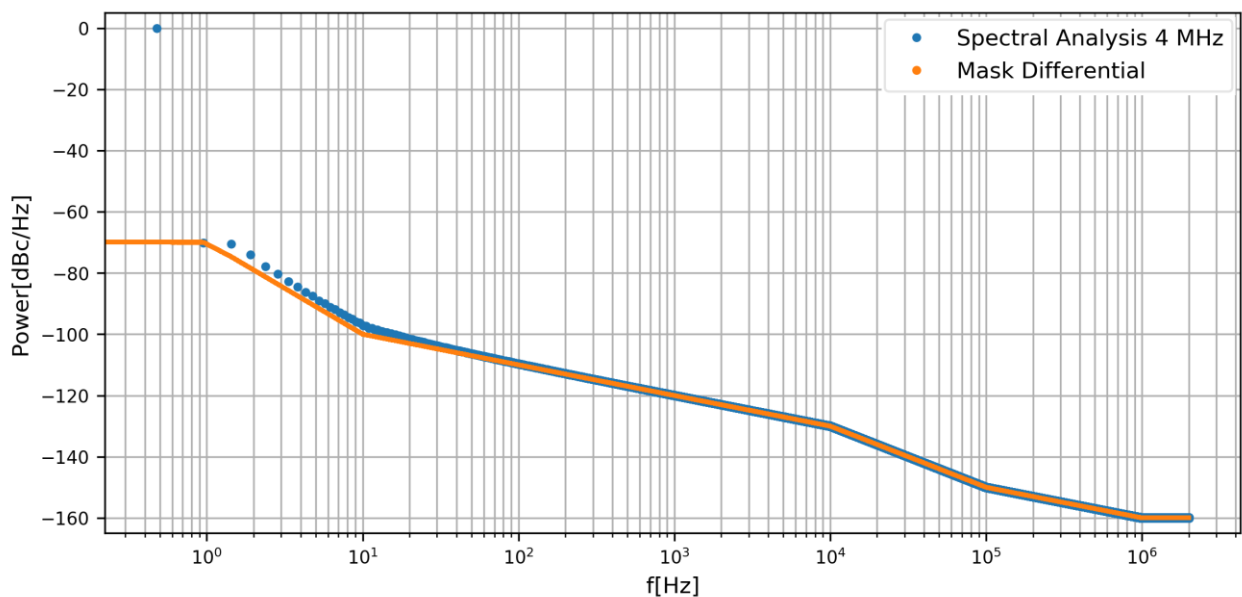
Figure 5.22: Spectrum of PN-impaired sine wave for differential mask, avg. over 50 000 iterations (blue), compared to differential PN mask (orange), f$_s$ = 4 MHz, carrier bin at 0.48 Hz

The resulting spectra compared to the PN mask for $f_s = 400\,\text{kHz}$ and $f_s = 4\,\text{MHz}$ can be found in Figure A.9 in Appendix A.3 and Figure 5.22 respectively.

It has to be noted again for clarity that the sampling frequency in this case is only $f_s = 4\,\text{MHz}$, i.e. lower by a factor of 10 compared to the previous case of $f_s = 40\,\text{MHz}$ because the differential PN mask contains a frequency point at 1 Hz that needs to be represented accurately. The frequency resolution for this case is therefore 0.48 Hz, lower by a factor of 10 as well. As the frequency resolution value of 0.76 Hz for the case of $f_s = 400\,\text{kHz}$ didn't change, δf is now lower for the $f_s = 4\,\text{MHz}$ case, which offers an explanation why the deviation from the specified PN mask is lower in that case as opposed to the $f_s = 400\,\text{kHz}$ case for the differential PN mask.

However, as noted before for the VSAT mask, in order to reduce the effect of deviation occurring at the 1.44 Hz point, the frequency resolution would have to be chosen at least 10 times lower than the first point of the mask, or 0.1 Hz.

5.3. Comparison of Methods

This section is dedicated to the comparison of IFFT-based and filter-based phase noise generation methods. As the IFFT-based method is the focal point of this thesis, it shall be regarded as the reference in the following. The filter-based method is presented as an alternative way of creating PN samples. Simulation results obtained using the same analysis tools and methods as for the IFFT-based PN generation in the previous section shall be applied to offer a thorough comparison between the methods.

The advantages and drawbacks of the IFFT-based method compared to the filter-based method are highlighted in Section 3.3 to discern which method is more suitable for which situation or use case. In terms of computational complexity, both methods have been compared in Section 4.3, so the focus of this section will be on the simulation results and the accuracy thereof.

In Section 5.3.1, the simulations for the statistical analysis are repeated from Section 5.1 for the filter-based method, and the results from both methods are compared in the form of standard deviation, PMF and CDF as well as CCDF.

In Section 5.3.2, the spectral analysis from Section 5.2 is similarly repeated for the filter-based method and results are presented in comparison to those from the IFFT-based method.

5.3.1. Time Domain

Since the results for $f_s = 400\,\text{kHz}$ and $f_s = 40\,\text{MHz}$ have shown no significant difference in Sections 5.1.1 and 5.1.2, only the analysis using the higher sampling frequency of $f_s = 40\,\text{MHz}$ is repeated for the samples generated with the filter-based method. Furthermore, the results of Section 5.1.2 have shown that the results are the same whether all samples of one realization of the PN process, one sampled realization of the PN process or a multitude of PN processes (each of them sampled once) are used, as long as enough samples are taken into account. The analysis for the filter-based method is repeated only for the first case, using all of the created PN samples for one realization of the PN process. These results are then compared to those from Section 5.1.1, where the equivalent analysis has been performed for the IFFT-based method.

Since the differential mask is not implemented in the form of filter banks in the JOANNEUM RESEARCH simulator and designing the necessary filters did not fit into the scope of this thesis,

no filter-based results have been obtained, meaning this chapter will focus on the remaining three masks.

Bin ranges and resolutions have been kept the same as in Section 5.1.1 in order to allow for results to be compared. They shall be re-iterated here for clarity if not already apparent from the related figures. The exemplary plots of the time series for each mask are very similar to the examples given in Figure 5.1, Figure 5.4, Figure 5.6, and Figure 5.8 for the four corresponding PN masks so that they are not visualized again in this context.

5.3.1.1. Critical Mask

For the critical mask, the bin resolution is 5°. The standard deviation is $\sigma = 75.98°$, and therefore significantly different from the $59.00°$ obtained with the IFFT-based method, suggesting that the PN samples still follow a zero-mean Gaussian distribution, but the absolute values are much larger to account for the larger standard deviation.

A comparison for PMF and CDF is shown in Figure 5.23 (a) and (b), respectively. It shows that both extreme values are much larger in terms of absolute value and also more likely to occur in the phase noise samples generated with the filter-based method, leading to an overall broader and less tall Gaussian distribution in the PMF in Figure 5.23a and a broader bell shape of the CDF/CCDF plot in Figure 5.23b.

(a)   (b)
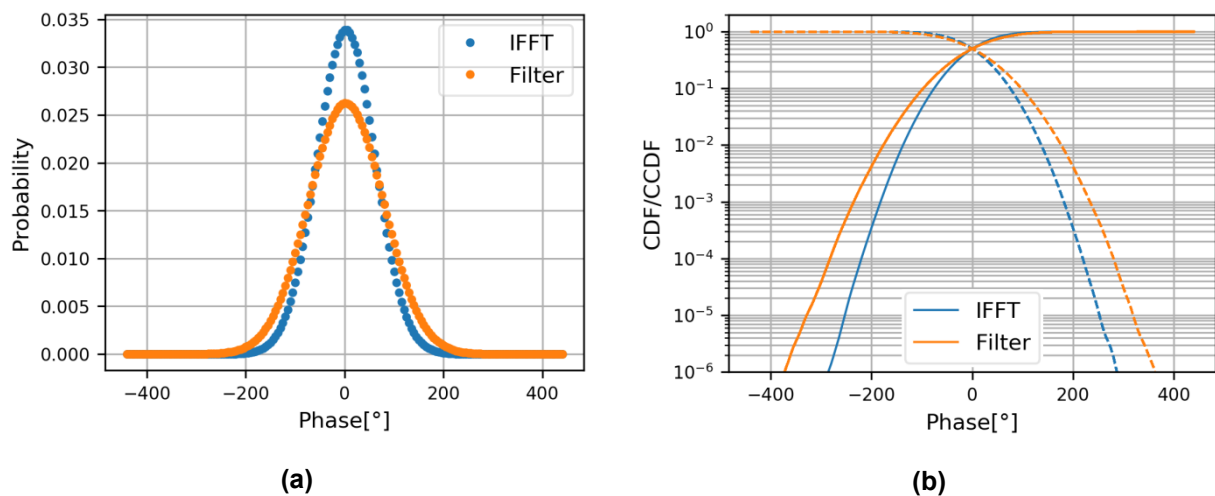
Figure 5.23: (a) PMF and (b) CDF/CCDF comparison (CDF solid line, CCDF dashed line) of critical mask for f_s = 40 MHz ($42 \cdot 10^9$ samples)

5.3.1.2. VSAT P2 Mask

For the VSAT P2 mask, the standard deviation is $\sigma = 6.24°$, roughly 1° smaller than the standard deviation for the IFFT-based method.

A comparison for PMF and CDF is shown in Figure 5.24 (a) and (b), respectively. Compared to Figure 5.23, the opposite effect is happening here, with filter-based method phase noise samples being smaller in absolute value and large deviations being less likely to occur.

That leads to the conclusion that, as opposed to the results from the critical PN mask, here the filter-based method-generated PN samples show the characteristics of smaller absolute values, a

narrower, but taller PMF and a more contracted bell shape of the CDF/CCDF plot. It can therefore be assumed that these characteristics are not specific to the method used, but rather influenced by the way the shape of the specified PN mask is represented by each method in the frequency domain, which will be analyzed in more detail in the following.

(a)   (b)
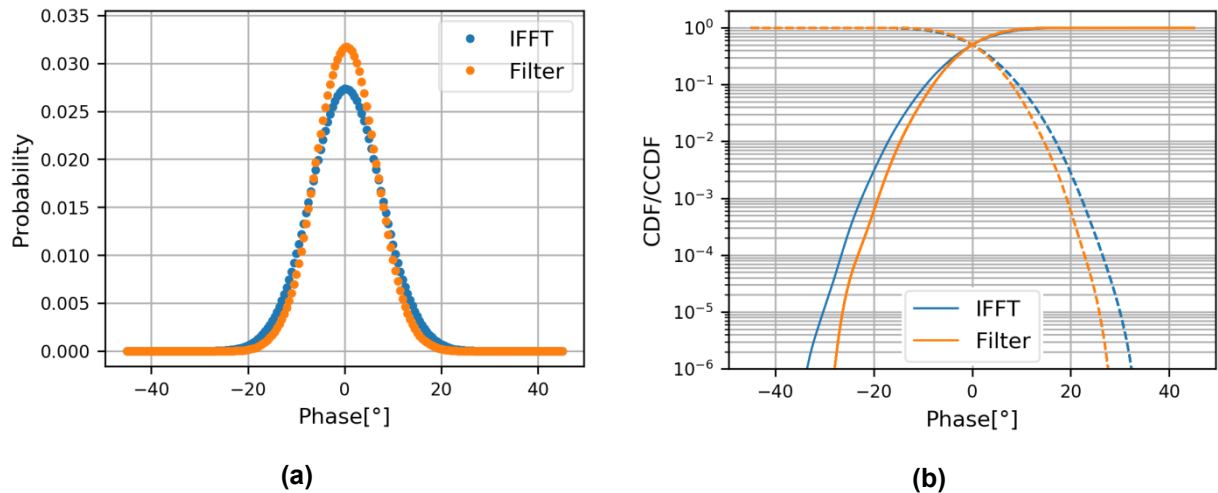
Figure 5.24: (a) PMF and (b) CDF/CCDF comparison (CDF solid line, CCDF dashed line) of VSAT P2 mask for f_s = 40 MHz (42·10^9 samples)

5.3.1.3. Transponder Mask

Finally, for the transponder mask with a bin resolution of 0.05°, the standard deviation is $\sigma = 0.571°$, a very slight deviation from the standard deviation value of $\sigma = 0.608$ from the IFFT-based method.

A comparison for PMF and CDF is shown in Figure 5.25 (a) and (b), respectively. As the small difference in standard deviation already suggests, the plots show only a very slight deviation from each other.

(a)   (b)
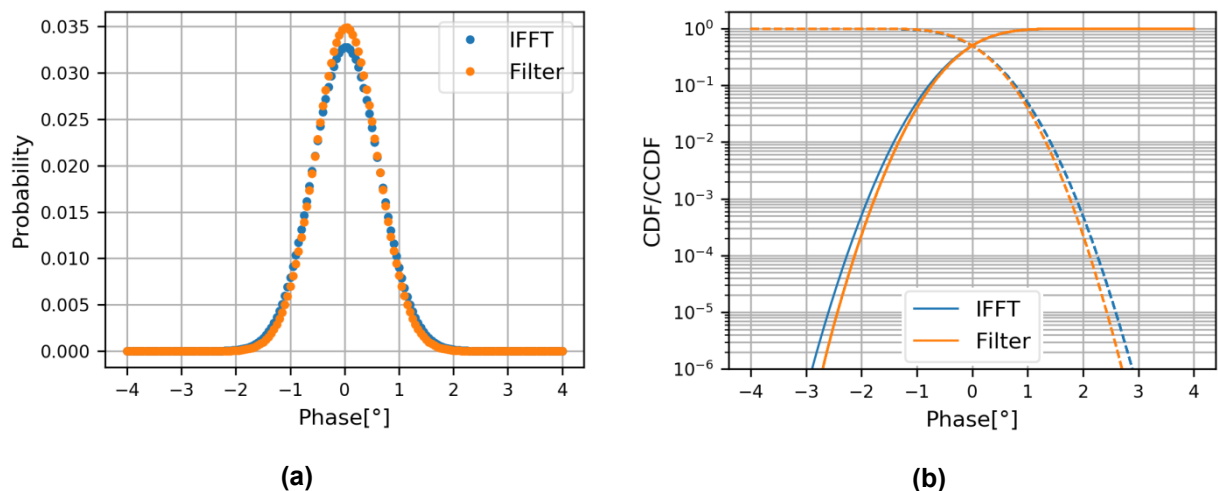
Figure 5.25: (a) PMF and (b) CDF/CCDF comparison (CDF solid line, CCDF dashed line) of transponder mask for f_s = 40 MHz (42·10^9 samples)

This result in conjunction with the results for the other two PN masks suggests that for the transponder PN mask, the IFFT-based and filter-based methods yield the most closely-matching results due to their characteristics being nearly equal across all frequencies. This assumption is further examined in the next section, where frequency domain results are compared.

5.3.2. Frequency Domain

In analogy to the time domain analysis, only the case of $f_s = 40\,\text{MHz}$ will be regarded for the spectral analysis of the filter-based method. While it would be possible to compare also the results obtained with $f_s = 400\,\text{kHz}$, there are several reasons to omit them. First of all, the results are contained within the $f_s = 40\,\text{MHz}$ case, where all frequencies from 0 Hz to 20 MHz are covered. Furthermore, Section 5.2 has already shown little difference in the results obtained for the $f_s = 400\,\text{kHz}$ case except for the influence of the different frequency resolution, making further investigations in this direction redundant.

5.3.2.1. Critical Mask

For the critical mask, the statistical analysis in the time domain in the previous section suggests a large deviation between both methods. For the dBc values at the specified frequencies that are presented in Table 5.6, deviations up to 6 dB at 1 kHz can already be noted.

In part, this can be explained by the deviation of the carrier bin at 4.77 Hz with a value of -7.5 dB opposed to the expected 0 dB, which is an even more significant deviation than the 4.6 dB observed in the case of the IFFT-based method.

Frequency	Mask [dBc/Hz]	IFFT-based [dBc/Hz]	Filter-based [dBc/Hz]
10 Hz	-25	-23.241	-21.781
100 Hz	-25	-23.571	-21.964
1 kHz	-50	-45.111	-39.107
10 kHz	-73	-68.304	-67.356
100 kHz	-83	-78.484	-80.291
1 MHz	-103	-98.486	-96.077
10 MHz	-114	-109.488	-105.843

Table 5.6: Critical mask dBc values for IFFT- and filter-based methods for f_s = 40 MHz

Regarding the graphical representation of the entire frequency range of both spectra in absolute dB values in Figure 5.26, it can be seen that the deviations between the methods are most notable for frequencies between 100 Hz and 1 MHz. It should be noted that this plot is given in units of dB instead of dBc/Hz as the relative difference between the curves is analyzed, not the difference to the specified PN mask. If these values were to be converted into dBc/Hz representations, the term $10 \cdot \log_{10}(4.77) = 6.79\,\text{dB/Hz}$ as well as the carrier power of $\Theta_{k_0,\text{dB}} =$

$-7.5 \, \mathrm{dB}$ would have to be subtracted from each frequency bin as specified in Eqs. (2.17) and (2.18), respectively.

The deviations seen in Table 5.6 mainly stem from the carrier attenuations caused by PN of this type. The biggest regions of difference between the two result curves are located around 3 kHz and 250 kHz, with apparent deviations of approx. 15 dB and 10 dB, respectively. These deviations likely stem from two-fold origins: firstly, from the characteristics of the low-pass filters used in the creation of the filter-based PN mask, which are hard to model accurately between the specified frequency points, and secondly, from the up-sampling process that is responsible for the characteristics of the filter at frequencies around 200 kHz.

However, these issues are limitations of the current implementation of the filter-based method, and could be alleviated with a more complex, and therefore more accurate, optimized filter design process. Equivalent to the IFFT-based method, this leads to a tradeoff between result accuracy and complexity of filter parameters such as filter order, roll-offs and attenuations.
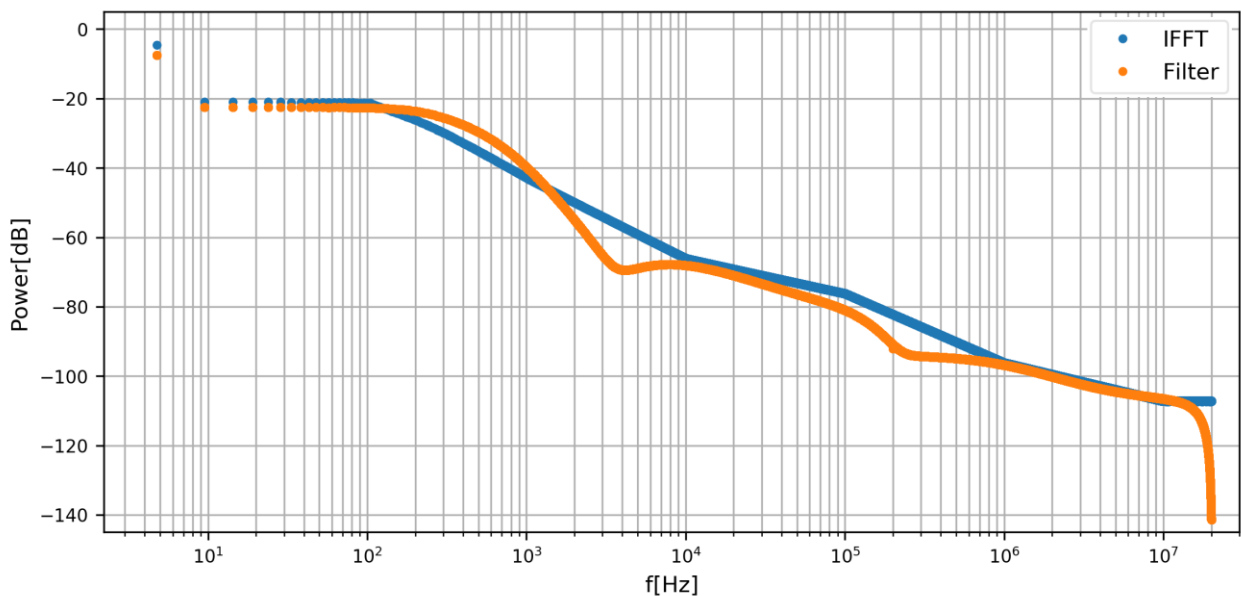
Figure 5.26: PN spectra comparison for critical mask, avg. over 50 000 iterations, f_s = 40 MHz, carrier at 4.77 Hz

The other immediately obvious difference is that for frequencies greater than the Nyquist frequency, the filter method, due to using low-pass filters only, is implemented to reach $-\infty$ at $f_s/2$, where the IFFT-based method assumes an AWGN characteristic for all frequencies greater than the maximum frequency defined in the PN mask. This is however a property of the implementation of the filter-based method and, as comparisons with an IFFT-based PN mask with similar characteristics have shown, does not impact the results in a meaningful way.

In order to show the influence of the carrier attenuation equivalent to Section 5.1.1.1 and create the link with the values in Figure 5.26, the absolute dB values are presented in tabular form in Table 5.7. This representation disregards the influence of the carrier attenuation caused by the PN mask. It can be seen that the largest difference between the two methods is then observed with 4.8 dB at 10 kHz, although as already stated Figure 5.26 suggests deviations of up to 15 dB for frequencies between 1 kHz and 10 kHz that are not represented in the table.

Frequency	Mask [dBc/Hz]	IFFT-based [dB/Hz]	Filter-based [dB/Hz]
10 Hz	-25	-27.749	-29.283
100 Hz	-25	-28.080	-29.465
1 kHz	-50	-49.619	-46.608
10 kHz	-73	-72.813	-74.857
100 kHz	-83	-82.993	-87.793
1 MHz	-103	-102.995	-103.579
10 MHz	-114	-113.997	-113.344

Table 5.7: Critical mask absolute dB values for IFFT- and filter-based methods for f_s = 40 MHz

5.3.2.2. VSAT P2 Mask

For the VSAT P2 mask, the comparison of dBc values at the specified frequencies can be found in Table 5.8. Compared to the results from the critical mask, both carrier attenuations are smaller by a factor of roughly 10^{-2}, and overall the deviations between the two methods seem less severe but still noticeable, which is supported by the time-domain results in Section 5.3.1. The maximum deviation again occurs for 10 kHz, this time with 2.8 dB.

Frequency	Mask [dBc/Hz]	IFFT-based [dBc/Hz]	Filter-based [dBc/Hz]
10 Hz	-33	-33.113	-34.041
100 Hz	-62	-59.416	-60.720
1 kHz	-79	-77.703	-78.666
10 kHz	-89	-88.819	-86.053
100 kHz	-95	-94.924	-94.789
1 MHz	-105	-104.924	-105.314
10 MHz	-115	-114.927	-114.475

Table 5.8: VSAT P2 mask dBc values for IFFT- and filter-based methods for f_s = 40 MHz

However, when looking at the behavior across the entire frequency spectrum in Figure 5.27, larger deviations are readily apparent for frequencies between 20 Hz and 1 kHz as well as around 200 kHz. These differences reach approx. 6 dB in magnitude. Once again, these deviations can be explained by the filter bank characteristics as well as up-sampling.
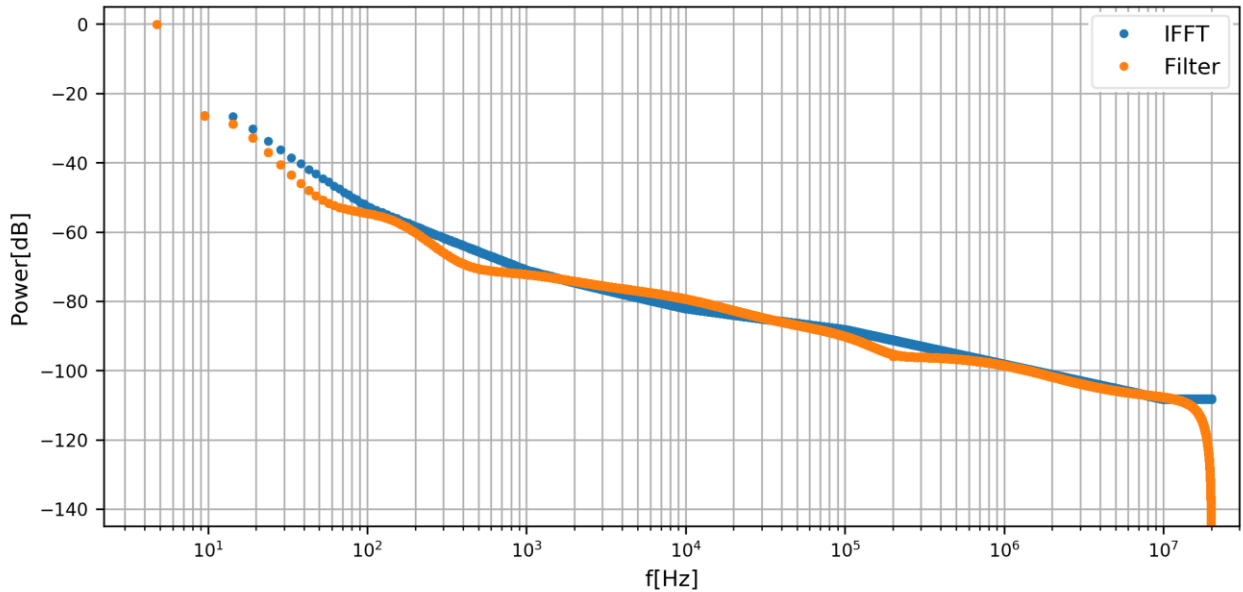
Figure 5.27: PN spectra comparison for VSAT P2 mask, avg. over 50 000 iterations, f_s = 40 MHz, carrier at 4.77 Hz

As before, it is once again noted that the curves in Figure 5.27 are given in units of dB as the plot is a relative comparison between results. They can therefore not be directly compared to the PN masks given in Section 2.3 in units of dBc/Hz without applying Eqs. (2.17) and (2.18) as explained for the critical PN mask.

5.3.2.3. Transponder Mask

For the transponder mask, the corresponding dBc value table is shown in Table 5.9. As suggested by the time domain results in Section 5.3.1, the difference of dBc values between methods is very small here. The result at 370 kHz has to be excluded from observations due to the point being defined at 100 kHz instead for the filter-based method, which is the main source of differences between the results for this PN mask. Disregarding this, the maximum deviation evident from Table 5.9 is 0.8 dB at 10 kHz.

Frequency	Mask [dBc/Hz]	IFFT-based [dBc/Hz]	Filter-based [dBc/Hz]
10 Hz	-63	-63.050	-62.61
100 Hz	-73	-72.732	-72.44
1 kHz	-83	-83.000	-82.352
10 kHz	-93	-92.967	-92.124
370 kHz/100 kHz	-112	-112.020	-114.735
1 MHz	-128	-128.001	-127.369

Table 5.9: Transponder mask dBc values for IFFT- and filter-based methods for f_s = 40 MHz

The graphical representation of the spectral domain characteristic in Figure 5.28 backs up these results, the only visible differences occur between 100 kHz and 1 MHz as well as for points > 1 MHz after the defined mask. The improved fit compared to the critical and VSAT P2 masks can also be explained by the constant slope of the mask for frequencies between 10 Hz and 10 kHz making filter design easier and the fact that only one point is defined for frequencies > 200 kHz, therefore making up-sampling less impactful.
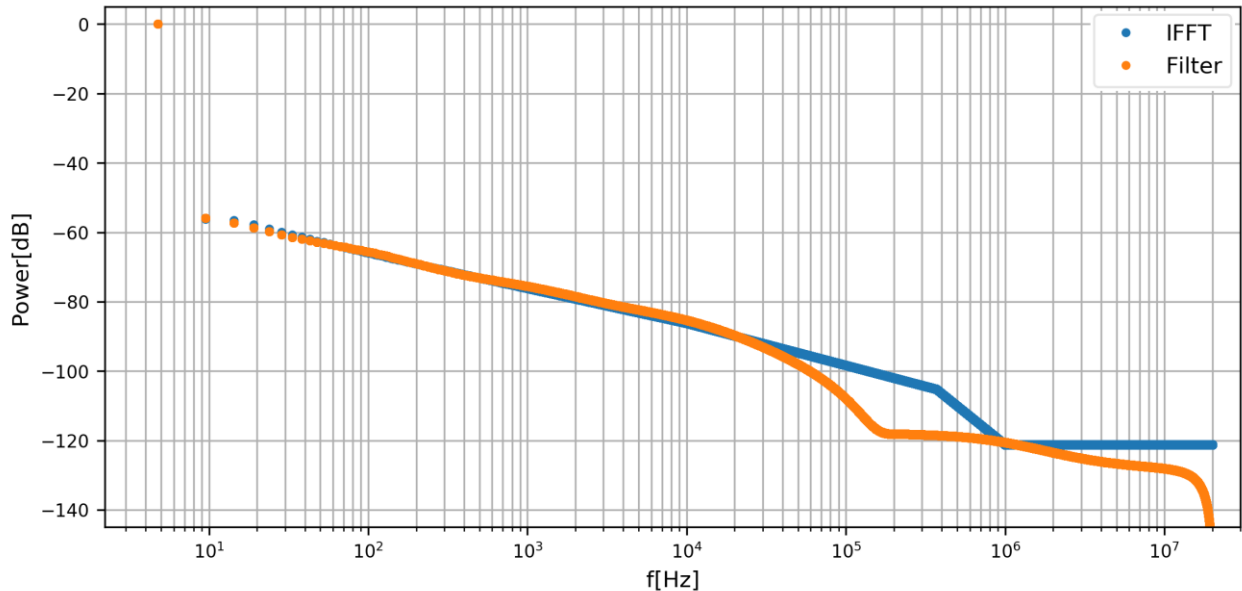
Figure 5.28: PN spectra comparison for transponder mask, avg. over 50 000 iterations, f_s = 40 MHz, carrier at 4.77 Hz

One last time, it shall be noted that the curves in Figure 5.28 are given in units of dB as opposed to dBc/Hz in the mask specifications, therefore the values cannot be used to directly compare them to the corresponding mask definition.

To conclude, it can be stated that the quality of results in the current implementation of both methods is better with the IFFT-based method, which is able to create PN samples that have frequency characteristics much closer to the PN mask utilized in their creation than is the case for the filter-based method. However, both methods are fully functional and deliver samples that can be both statistically and spectrally analyzed. The accuracy of results is dependent on the computational complexity of the FFT/IFFT for the IFFT-based method and the filter design and optimization for the filter-based method, and therefore results in a tradeoff for both PN generation methods. With the current implementation, the IFFT-based method yields more accurate results with an acceptable expenditure in terms of computational complexity and has the additional advantage of easy PN mask adjustment for further simulations, therefore it is selected as the PN generation method for the analysis of the impact PN has on modulated signals in the subsequent and last section of this chapter.

5.4. Analysis of Modulated Signals

After the phase noise generation methods have been verified to work as desired as well as having been compared through simulations in the previous chapters, the impact of phase noise on modulated signals, phase tracking and FER is to be analyzed in this section. In order to achieve that, modulated signals distorted by phase noise such as those utilized in DVB-S2X have to be used for the analysis instead of a sine waveform. This requires the use of more advanced simulation blocks overall, as bit-to-symbol mapping, matched filtering and demodulation are necessary at minimum to simulate and analyze modulated signals. The overall simulation structure has already been described in detail in Section 4.2.

For the analysis of how phase tracking is affected by PN, the V&V phase tracker described in Section 2.2.3 is used at the RX in order to compare the untracked and tracked results, leading to an assessment of the tracker performance, as described in Section 5.4.1.

Finally, a full simulation of DVB-S2X waveforms is presented to round out the thesis in Section 5.4.2. It comprises a concatenated BCH/LDPC coding scheme for error correction, a DVB-S2X framing structure, synchronization of carrier phase, frequency and symbol timing and the calculation of the FER across different modulation schemes and PN impairment types.

5.4.1. Phase Tracker Performance

For the phase tracking performance assessment, QPSK has been chosen as a modulation scheme. Bursts of length 262 144 bits which contain only 0 are used with a baud rate of 400 kSymbols/s and mapped onto the constant QPSK symbol "00" that is repeated 131 072 times per burst. This is done to facilitate the analysis of the results, as the correct symbol is known at the RX, which simplifies SER calculation. If a symbol is not decoded as "00", it is immediately identified as a symbol error and no further information exchange between TX and RX module is necessary. The length of the bursts has been chosen in such a way as to accommodate one full FFT length of $N = 2^{19}$ using the 4 times oversampled signal.

PN samples created by the IFFT-based method with $f_s = 400\,\text{kHz}$ are then added to the signal. While it would be possible to use PN samples with $f_s = 40\,\text{MHz}$, it would result in significantly larger burst lengths in order to allow for spectral analysis. This would in turn significantly increase complexity of the overall simulation and enlarge the time the tracker must work without the aid of known symbols (in the form of the initial acquisition of the subsequent burst in this case). That however would represent a scenario not comparable to the overall DVB-S2X system. This constitutes another tradeoff, as the PN contribution from frequencies greater than 200 kHz is neglected, however it is a necessary step to limit simulation complexity.
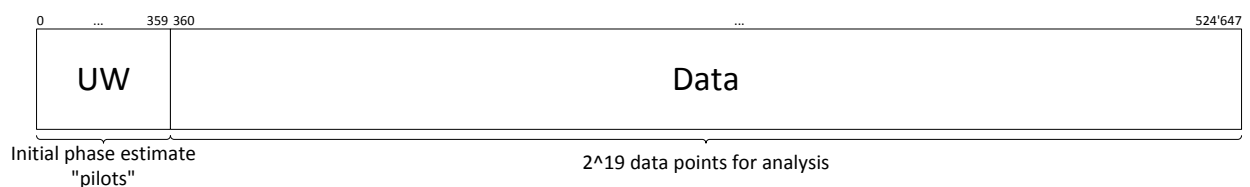
Figure 5.29: Burst structure with unique word (UW) and data, oversampled by factor of 4

The V&V phase tracker is described in Section 2.2.3 with a configurable loop bandwidth $B_L T$. An initial acquisition is performed using a unique word with a length of 80 bits that is added to the

front of each data burst. The unique word is subsequently removed after phase tracking so that the data analysis is unaffected by it. Figure 5.29 exemplifies the structure of one burst oversampled by a factor of 4.

The V&V phase tracker itself is realized as a second-order loop

$$F(z) = A + \frac{B}{z - 1} \tag{5.1}$$

with filter coefficients

$$A = 2\frac{\zeta\omega_n T}{K_d} \tag{5.2}$$

and

$$B = \frac{(\omega_n T)^2}{K_d}, \tag{5.3}$$

where ζ is known as damping factor and chosen as $\zeta = 1$, K_d is the detector gain and ω_n is the natural frequency. [10]

The single-sided noise bandwidth normalized to symbol period T is not available in closed form for second-order loops, but can be analytically approximated by [10]

$$B_L T \approx \frac{\omega_n T}{2\left(\zeta + \frac{1}{4\zeta}\right)}. \tag{5.4}$$

Given that the damping factor and detector gain are chosen as constant values, $B_L T$ directly relates to the filter coefficients A and B and can therefore be used as an input parameter to tune the tracker performance across different types of PN and AWGN impairment. A more in-depth description of the NDA FB phase tracker can be found in [10].

Using QPSK as a modulation scheme, the constellation points are at a distance of $\pi/2$, or 90° apart from each other, meaning that a phase noise impairment of less than ±45° will not lead to symbol errors on the RX side. Therefore, regarding the results from Section 5.1, only the critical mask leads to PN of sufficient phase variation to affect the QPSK demodulation if no additional AWGN is added to the signal. This assertion is supported by the I/Q scatter plots shown in Figure 5.30 and Figure 5.31 for critical and VSAT P2 PN mask, respectively.

It has to be noted that due to internal properties of the JOANNEUM RESEARCH simulator, modulated signals are always adjusted to 3 dB power for implementation reasons. This leads to an I/Q plot where the QPSK constellation point "00" as taken from Figure 2.2 is located at coordinates $I = 1, Q = 1$. In order to guarantee functionality, all impairments and related figures are scaled with the same factor; therefore the results are not affected by this in any way.

In the untracked case for critical PN, it can immediately be seen that all phase values from -180° to 180° occur due to the magnitude of the PN impairment. The improvement upon using a phase tracker is also apparent, where in the case of a loop bandwidth of $B_L T = 0.01$ symbol errors still occur, however for higher values of $B_L T$ results that lie exclusively within the correct decision region can be achieved. It has to be noted however that a theoretical SNR approaching ∞ was assumed to obtain these results, the thickness of the points in Figure 5.30 and Figure 5.31 is chosen as gradually decreasing to maintain visibility when points are superposed, not as an indication of AWGN.
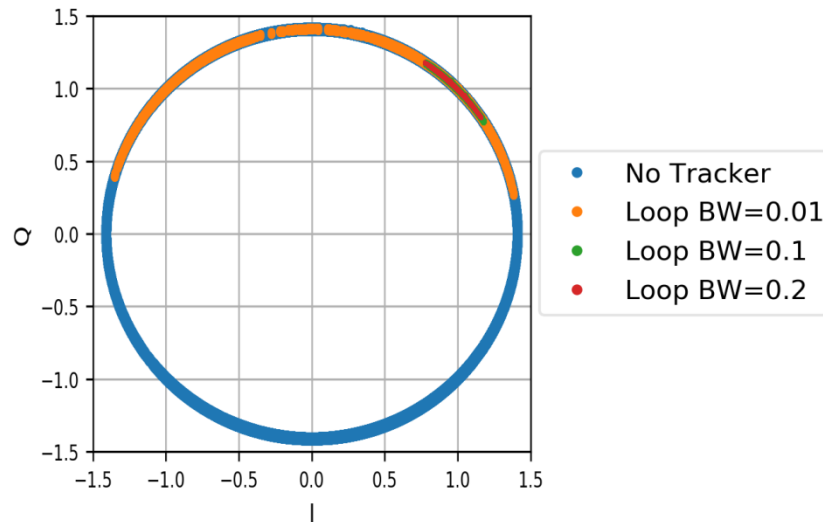
Figure 5.30: I/Q scatter plot of QPSK signal with critical mask PN (f$_s$ = 400 kHz), B$_L$T values of 0.01 (orange), 0.1 (green), and 0.2 (red) compared to the untracked result (blue)

For the VSAT P2 mask, as was already assumed from the results of the statistical analysis in previous sections, it is apparent that even without a phase tracker, symbol errors will never occur due to the large decision regions of QPSK. Nevertheless, significant improvements of the phase sample distribution that improve as the loop bandwidth $B_L T$ rises can be obtained if a V&V phase tracker is used here as well.
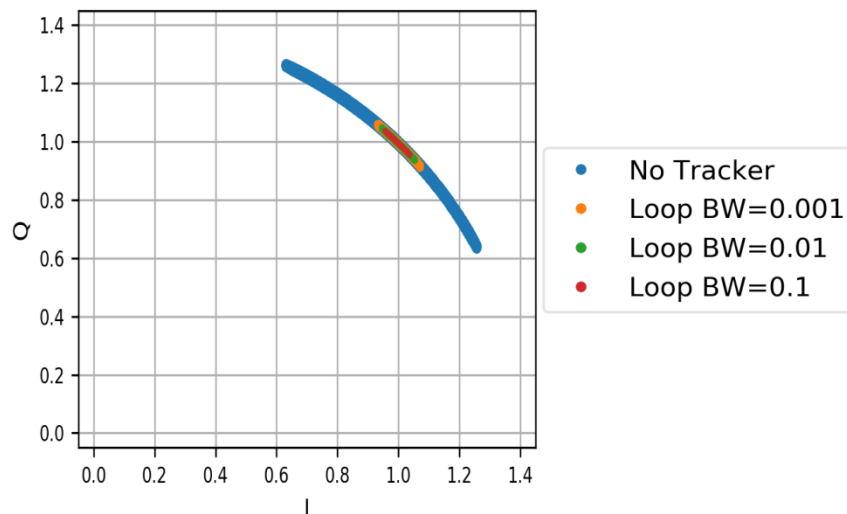
Figure 5.31: I/Q scatter plot of QPSK signal with VSAT P2 mask PN (f$_s$ = 400 kHz), B$_L$T values of 0.001 (orange), 0.01 (green), and 0.1 (red) compared to the untracked result (blue)

The spectral analysis analog to Section 5.2 can be performed to show which frequency ranges of PN impairment can be reduced using phase tracking. Figure 5.32 through Figure 5.35 show this for various $B_L T$ settings without AWGN influence for the four PN masks. The plots are in units of

dB with the QPSK carrier with a power of 3 dB (due to the internal simulation environment properties as explained above) at 0 Hz not being shown in a logarithmically scaled plot.
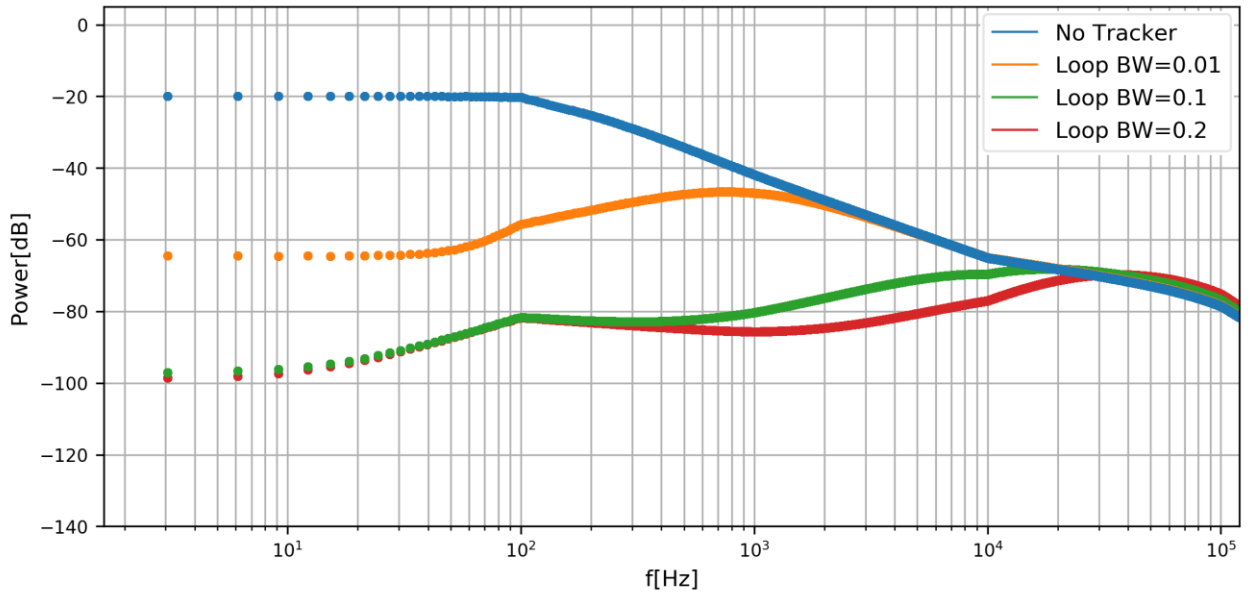
Figure 5.32: Spectrum of QPSK signal with critical mask PN (f_s = 400 kHz), B_LT values of 0.01 (orange), 0.1 (green), and 0.2 (red) compared to the untracked result (blue)
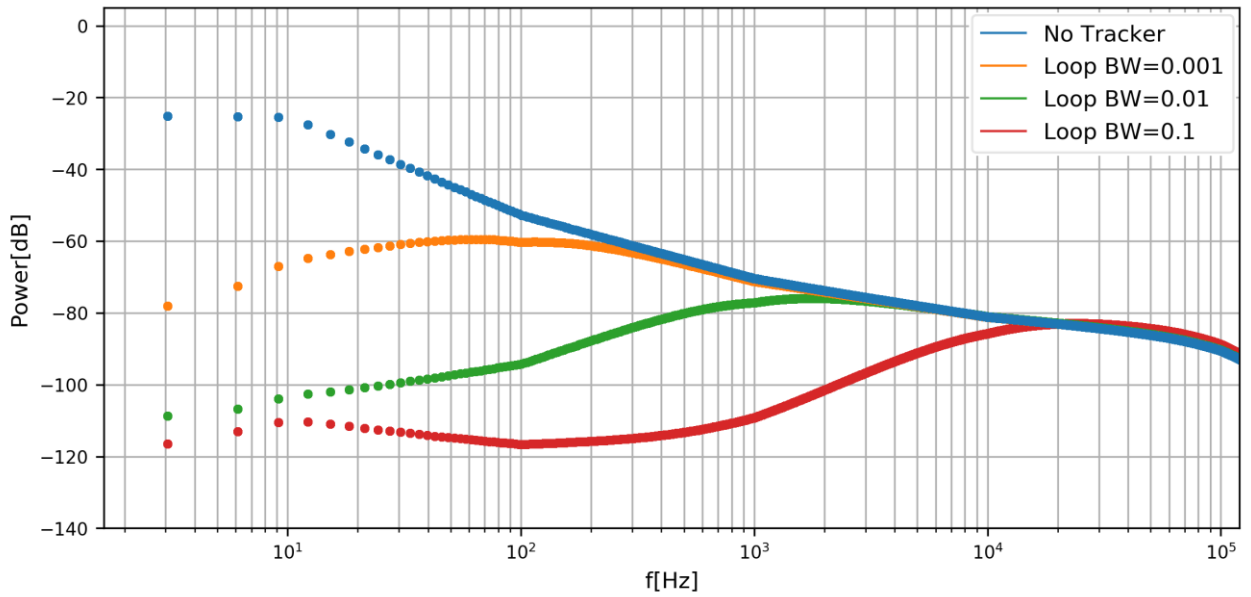
Figure 5.33: Spectrum of QPSK signal with VSAT P2 mask PN (f_s = 400 kHz), B_LT values of 0.001 (orange), 0.01 (green), and 0.1 (red) compared to the untracked result (blue)
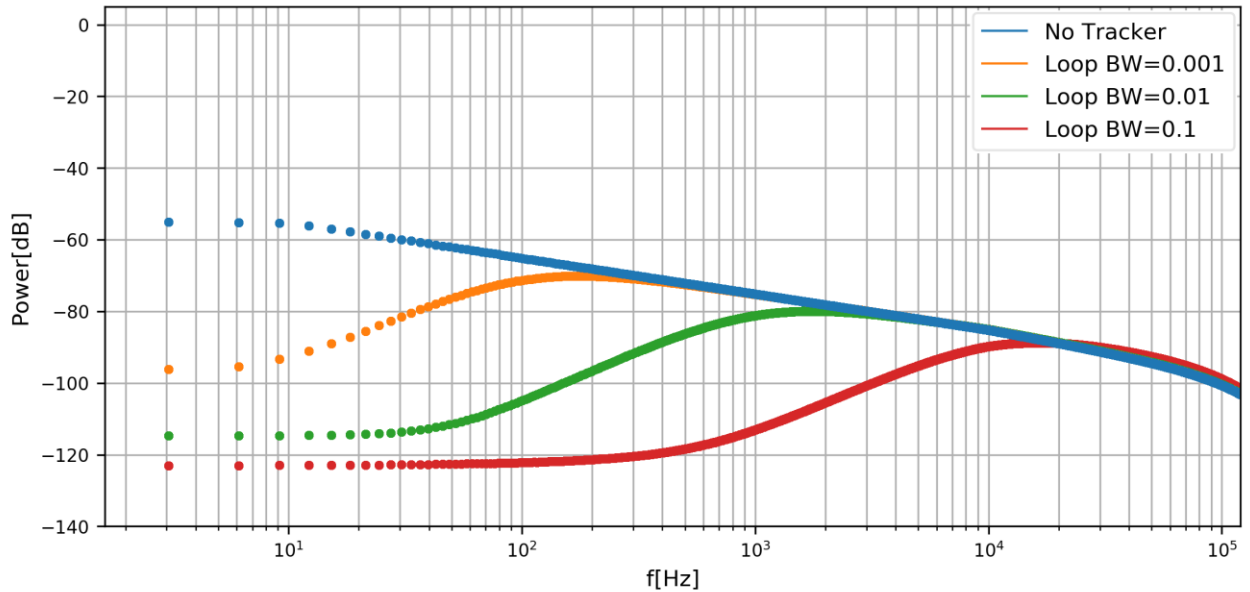
Figure 5.34: Spectrum of QPSK signal with transponder mask PN (f_s = 400 kHz), B_LT values of 0.001 (orange), 0.01 (green), and 0.1 (red) compared to the untracked result (blue)
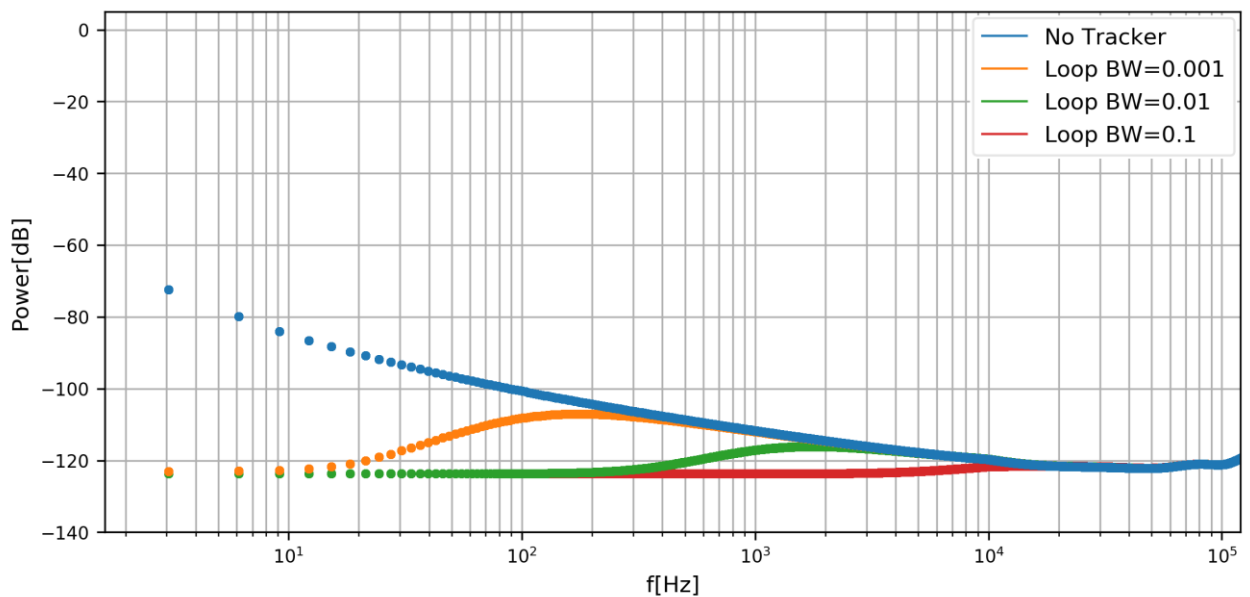
Figure 5.35: Spectrum of QPSK signal with differential mask PN (f_s = 400 kHz), B_LT values of 0.001 (orange), 0.01 (green), and 0.1 (red) compared to the untracked result (blue)

As these plots are meant to give a relative comparison between different settings of the loop bandwidth, they are given in units of dB. The matched filter has a cutoff frequency of 200 kHz with a roll-off factor of $\alpha = 0.25$, therefore the plots are only shown up to 120 kHz to minimize the displayed distortion. The results show that for increasing noise bandwidth, more PN impairment is removed due to the tracker being able to better follow the impaired signal. At higher frequencies the tracker does not achieve a gain compared to the untracked signal. It should further be noted that if AWGN is added to the signal, some of the parameter sets yield the system inoperable because the large loop bandwidth leading to a large quantity of AWGN noise

being picked up. Therefore, a balance was to be found between a small enough $B_L T$ that effectively reduces the impact of AWGN by averaging and a large enough $B_L T$ so that the PN-induced random-walk behavior of the samples can still be followed. This is more closely analyzed in the sequel when AWGN is introduced into the system.

Next, histograms of all samples of one burst are generated with and without phase tracking and compared, still without AWGN interference. For this purpose, a realistic value of $B_L T = 0.05$ has been selected for the comparison for all PN masks. In Section 5.1.1 the absolute values of the generated phase noise samples are plotted, therefore allowing the phase to range from $-\infty$ to $+\infty$. In comparison, the phase offset from the unimpaired value of $\varphi_m = 45°$ for the QPSK constellation point "00" is plotted. Since oversampled QPSK symbols are used for the generation of the histogram, the values are limited to ±180°. Even if the total phase noise impairment is higher than those values, they are wrapped around on the unit circle, e.g. a phase distortion of 210° will show up as -150° in the histogram. For this reason, the CDF/CCDF is only plotted to 10^{-4} for the case of the critical mask, where a phase offset of 180° is reached for that value already.

5 000 consecutive bursts have been analyzed, leading to a total of $2.6 \cdot 10^9$ samples for each case. The results are depicted in Figure 5.36 through Figure 5.39 for the four PN masks. The bin size for the critical and VSAT P2 masks is 0.5°, for the transponder mask 0.05° and for the differential mask 0.002°. The ranges of the x-axis differ from mask to mask in such a way as to portray the entirety of the phase offsets in full. Since the difference between the ranges is so large, a visualization that allows comparisons between masks more clearly is not possible.

(a) (b)
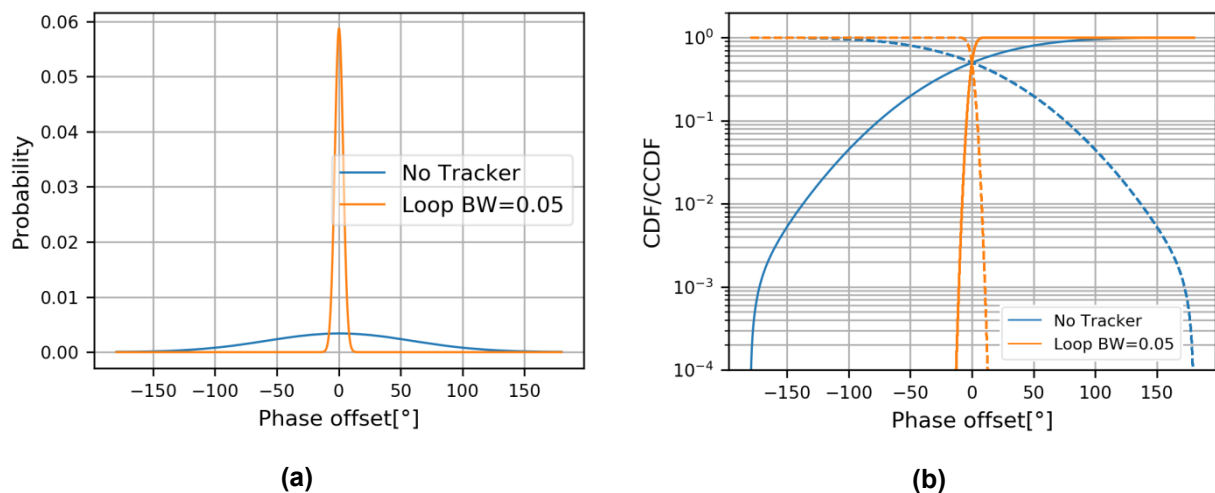
Figure 5.36: (a) PMF and (b) CDF/CCDF comparison (CDF solid line, CCDF dashed line) of phase offset with critical mask PN: no tracker vs V&V tracker with $B_L T = 0.05$ (2.6·10^9 samples)

(a)

(b)
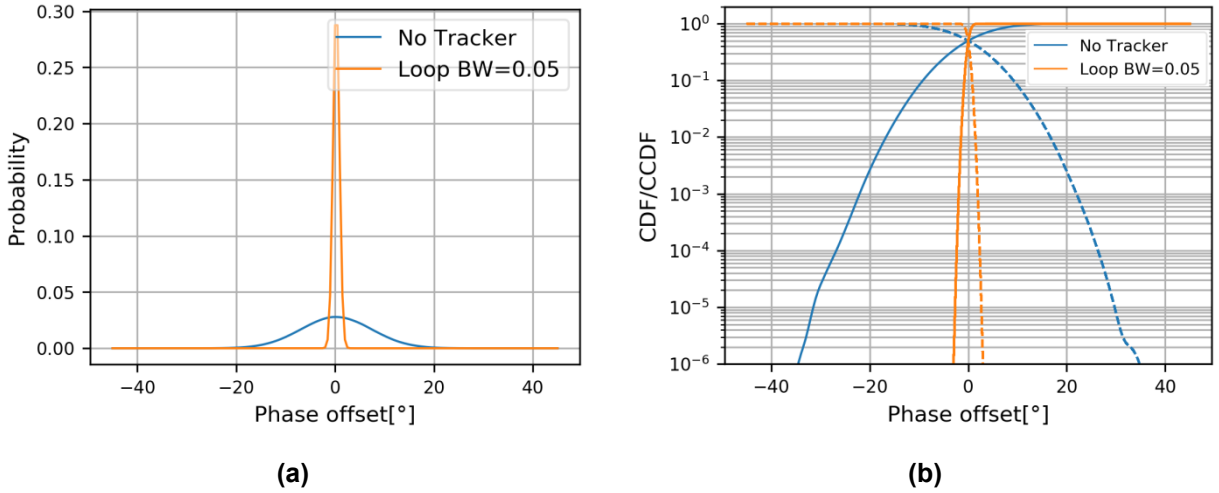
Figure 5.37: (a) PMF and (b) CDF/CCDF comparison (CDF solid line, CCDF dashed line) of phase offset with VSAT P2 mask PN: no tracker vs V&V tracker with $B_LT = 0.05$ ($2.6 \cdot 10^9$ samples)

(a)

(b)
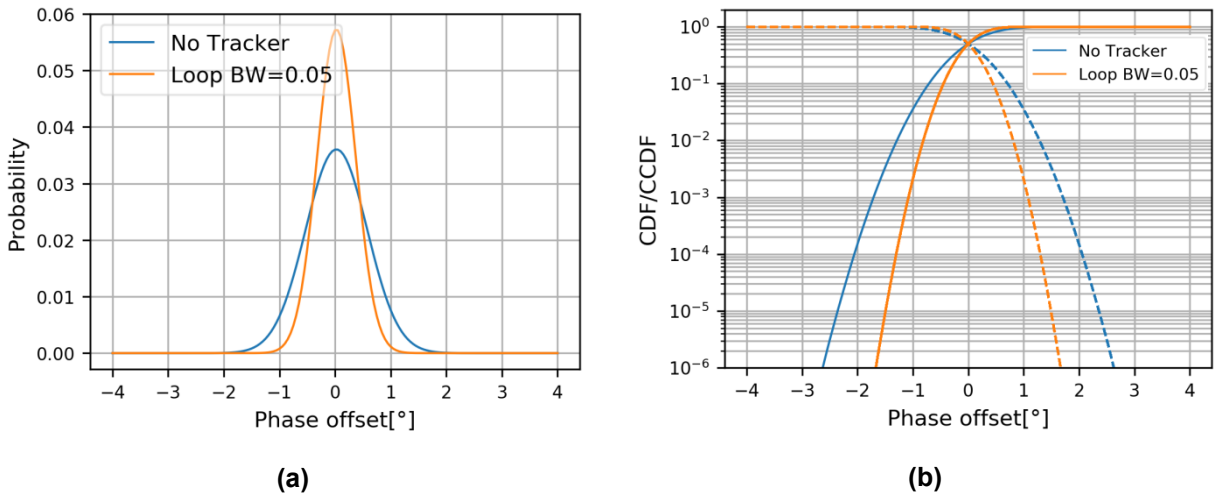
Figure 5.38: (a) PMF and (b) CDF/CCDF comparison (CDF solid line, CCDF dashed line) of phase offset with transponder mask PN: no tracker vs V&V tracker with $B_LT = 0.05$ ($2.6 \cdot 10^9$ samples)

(a)

(b)
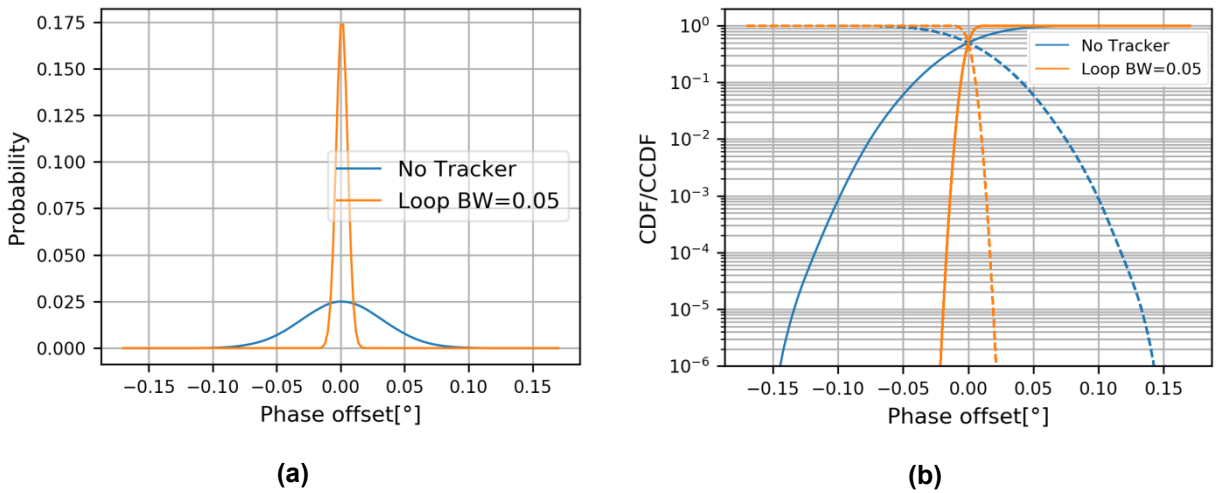
Figure 5.39: (a) PMF and (b) CDF/CCDF comparison (CDF solid line, CCDF dashed line) of phase offset with differential mask PN: no tracker vs V&V tracker with $B_LT = 0.05$ ($2.6 \cdot 10^9$ samples)

It can be seen from both the probability distribution of the PMF as well as the CDF and CCDF that for all masks the magnitude of the phase impairment is reduced significantly when tracking is employed. In the case of the transponder mask it seems that $B_L T = 0.05$ is not the ideal parameter selection as the tracked values show less improvement over the untracked ones compared to all other masks.

In the following, only the critical mask is regarded for simulations, as it can clearly be seen from Figure 5.37 that the VSAT P2 mask (and consequently the transponder and differential mask as well) leads to phase distortions of less than ±40°, which is smaller than the ±45° decision boundary region for QPSK mentioned at the beginning of this section. Consequently, phase noise generated from any of these masks will never lead to symbol errors on its own and only the critical mask can be utilized to measure meaningful symbol and burst error rates. Even if symbol errors occur for other masks if the SNR is lowered and the AWGN influence increases, the critical PN mask still constitutes a worst-case for the performance of the phase tracker and is therefore the most interesting case for analysis.

Now, AWGN is added as another form of impairment to the channel, as depicted by the dotted line in Figure 4.5. In order to determine a feasible $B_L T$ setting, the CSR has been measured over a wide range of $B_L T$ values with an SNR of 10 dB. To achieve that, a burst is considered to be erroneous if the SER after demodulation within said burst exceeds 0.5. This indicates that a cycle slip has likely occurred within the tracker, and since the tracker is NDA, no additional supporting points such as pilots exist to correct such an event until the start of the next burst. Therefore, all symbols after the cycle slip will be erroneous unless another cycle slip occurs that moves the tracker back to the global minimum as explained in Section 2.2.3.

The CSR is then calculated by dividing the number of erroneous bursts by the total number of bursts analyzed:

$$\text{CSR} = \frac{\text{number of bursts with SER} > 0.5}{\text{total bursts}}. \tag{5.5}$$

By varying the $B_L T$ parameter of the phase tracker, a feasible range of values can be identified where the tracker performance in terms of CSR is below 10^{-3}. This can be seen from Figure 5.40, where the CSR is plotted versus the $B_L T$ in a log-log plot. Based on these results, $B_L T = 0.05$ is used in the following as an example value where the tracker exhibits good performance.
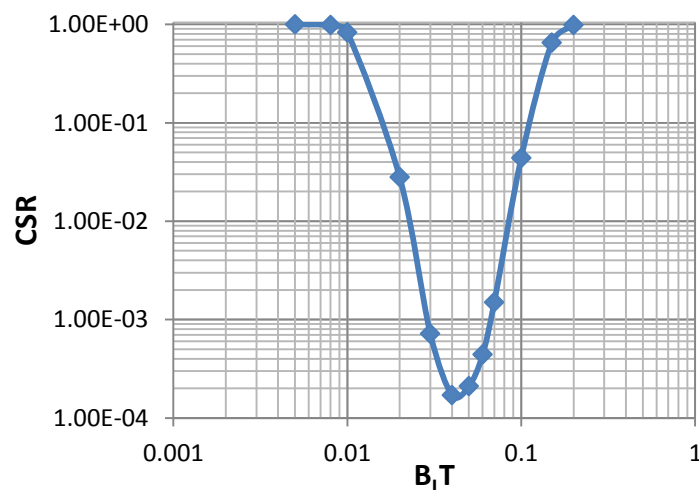
Figure 5.40: Log-Log plot of CSR over B$_L$T for critical mask PN and AWGN with SNR = 10 dB

Using this $B_L T$ value and an SNR of 10 dB, another scatter plot is created to show how the tracker performs in the presence of AWGN. Figure 5.41 shows that the parameter settings of the tracker lead to a good phase correction overall. However, the SER is in the order of $2.7 \cdot 10^{-3}$, meaning symbol errors still occur due to the levels of AWGN added to the signal. Nevertheless, when compared to $\mathrm{SER_{noPN}} = 2.1 \cdot 10^{-3}$ for the case of no PN impairment with the same simulation parameters, the SER increase due to tracked PN is only in the order of 10^{-4}. For the untracked blue points in Figure 5.41, $\mathrm{SER_{noTracker}} = 4.1 \cdot 10^{-1}$, showing that phase tracking in this case achieves a gain in the order of 10^2 in terms of SER.
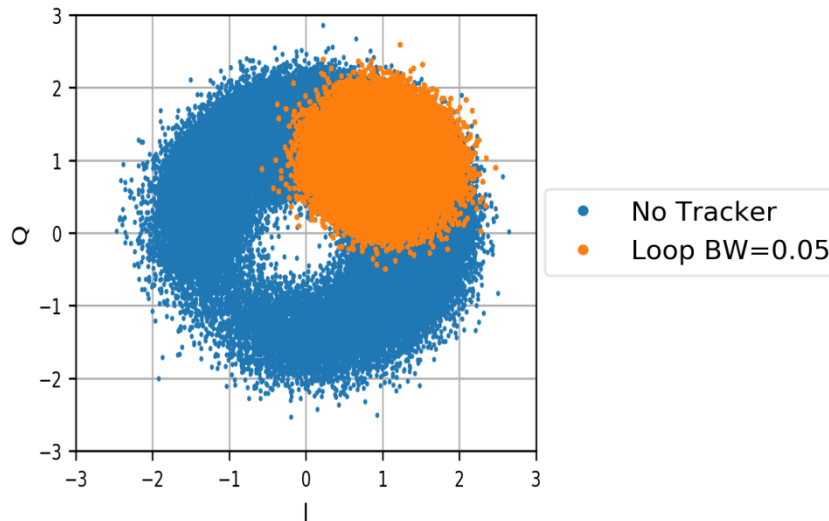
Figure 5.41: I/Q scatter plot of QPSK signal with VSAT P2 mask PN (f$_s$ = 400 kHz, SNR = 10 dB), B$_L$T = 0.05 (orange) compared to the untracked result (blue)

Finally, using the results obtained so far, a spectral representation of the QPSK signal impaired by both PN and AWGN is analyzed with the chosen tracker noise bandwidth $B_L T = 0.05$ for different SNR values of 10 dB, 20 dB, and 30 dB.

The results of this analysis are found in Figure 5.42, where, just like in the spectral analysis above, the values are not adjusted to 1 Hz bandwidth and not corrected for dBc. However, as this only introduces a constant offset, a qualitative comparison and analysis of the results can still be done. Once again the frequency axis is cut off at 120 kHz due to the characteristics of the matched filter at higher frequencies.

It can be seen that for SNR = 10 dB, a relatively high AWGN noise floor is introduced at -60 dB, and the tracker is able to reduce the influence of the phase noise at least close to that level for nearly all frequencies except the ones smaller than 30 Hz. For an SNR of 20 dB, the noise floor is obviously 10 dB lower, however it can be seen that the tracker performance between 1 kHz and 10 kHz is significantly worse, leading to a rise of the overall power in that region. This effect is even more pronounced for SNR = 30 dB and when looking at the tracker performance without additional AWGN (SNR $\rightarrow \infty$), where only the frequencies below 100 Hz and above 100 kHz are significantly differing from the 30 dB case.

This leads to the assumption that the tracker is able to follow the signal if the phase noise does not change too rapidly from one sample to the next because it is mainly affected by low frequencies in the generating mask. This shows that the region around 10 kHz is the most critical

for the tracker, because these frequencies are still fairly high in the PN mask (-73 dBc/Hz at 10 kHz for the critical mask as specified in Section 2.3) but cannot be properly tracked anymore due to their larger sample-to-sample variation. On the other hand, a larger noise bandwidth $B_L T$ would lead to a better damping of the PN at higher frequencies, but the increased AWGN picked up by the filter becomes problematic, leading to an increased SER and therefore CSR. This renders values such as $B_L T = 0.2$, which shows a significantly better performance up to 20 kHz as exemplified in Figure 5.32 unusable, however in this scenario is out of scope since its CSR approaches 1 as shown in Figure 5.40.
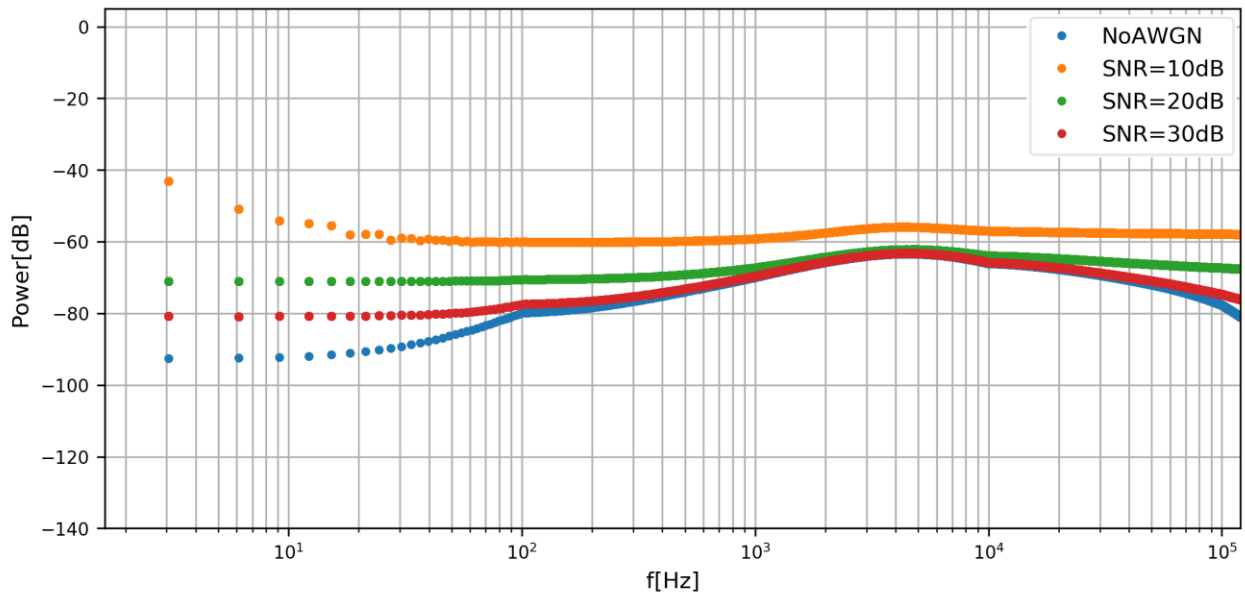
Figure 5.42: Spectrum of QPSK signal with critical mask PN and different SNR values (f$_s$ = 400 kHz, BLT = 0.05)

5.4.2. FER Analysis

The FER measurement follows the block diagram presented in Figure 4.6. One DVB-S2X *physical layer signaling* (PLS) code is selected to run the tests per *modulation-and-coding* (MODCOD) scheme. For modulation schemes, the results pertaining to QPSK as the best-case scenario in terms of robustness to phase noise impairment, as well as 32-ary APSK as a worst case scenario are presented. The code rates are chosen arbitrarily as they have no influence on the comparison between the system unaffected and affected by PN and merely shift the entire curves to lower or higher SNR regions. For QPSK, a code rate of ½ has been selected, whereas for 32-APSK, a code rate of ¾ is chosen. In terms of PN impairment, the critical mask is at first selected and analyzed. In accordance with the use case of the critical mask, which is supposed to represent older equipment in a DTH scenario, typical DTH parameters have been chosen for the simulation. The baud rate is set to 40 MSymbols, short (16 200 bits) frames with pilot symbols are used, and a roll-off factor of $\alpha = 0.25$ is selected.

In Figure 5.43, the FER curves for QPSK are plotted. The system unaffected by PN is displayed as a reference and compared to the PN affected system for both filter-based and IFFT-based PN generation method using the critical PN mask. It can be seen that while both curves are within 0.1 dB of the reference, the IFFT-based method yields significantly worse results compared to the filter-based method. Comparing with the methods in Section 5.3, Figure 5.26 shows there are

significant differences in the filter-based PN mask due to the characteristics of the filters themselves. Because creating masks is relatively easy for the IFFT-based method, a mask approximating the filter-based result from Figure 5.26 has been created. Using this IFFT comparison mask to simulate the FER, the results for both methods are nearly equal (purple curve in Figure 5.43). Furthermore, it can be conjectured that the frequencies at which differences between the methods occur in Figure 5.26, namely the regions around 40 kHz and 200 kHz have a significant impact on the overall performance degradation due to PN, as these are the main differences in the masks that lead to a degradation from the filter-based to the initial IFFT-based curve of roughly 0.5 dB.
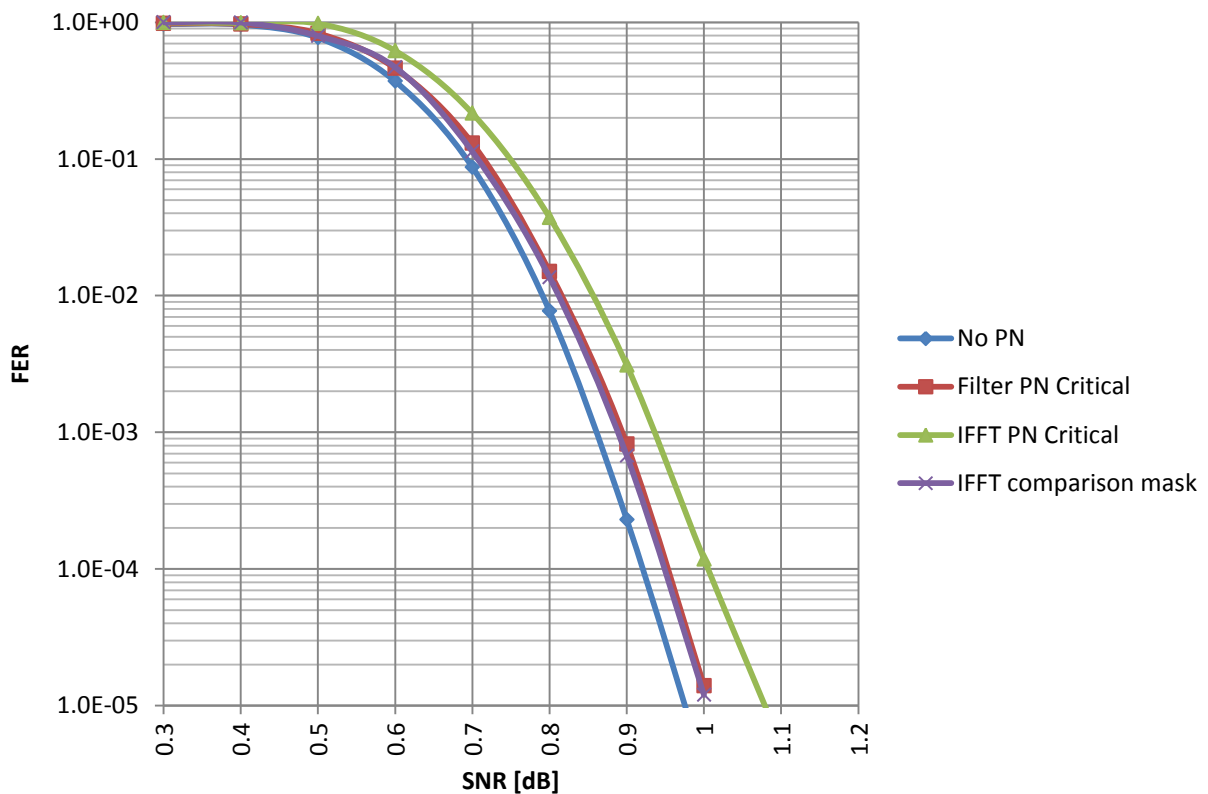
Figure 5.43: FER over SNR for QPSK ½, critical PN with different generation methods

For 32-APSK, these differences have an amplified effect, as can be seen from Figure 5.44. For the filter-based method, the critical mask remains within 2 dB of the reference curve unimpaired by PN due to the discrepancy between its definition and implementation. However, the IFFT-based method does not yield acceptable results anymore. It is therefore proposed to switch from the critical to the typical PN mask. The typical PN mask as defined in [1] only differs from the former in the value of the 100 kHz point, which moves from -83 dBc/Hz to -93 dBc/Hz. The entire definition of the mask taken from [1] can be found in Table 5.10.

Frequency	Mask Λ [dBc/Hz]
10 Hz	-25
100 Hz	-25
1 kHz	-50
10 kHz	-73
100 kHz	-93
1 MHz	-103
≥ 10 MHz	-114

Table 5.10: Typical mask
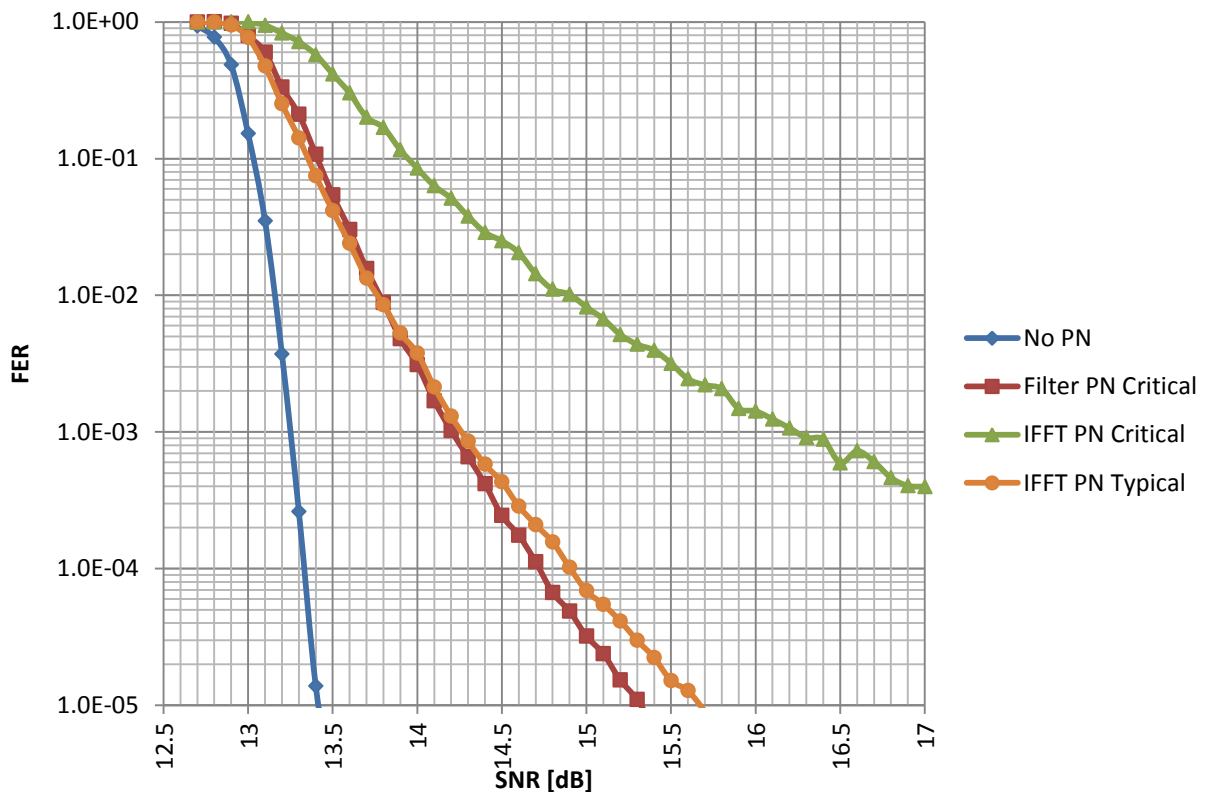
Figure 5.44: FER over SNR for 32-APSK ¾, critical/typical PN with different generation methods

This change by 10 dBc/Hz in one point of the mask definition leads to a significant improvement in the FER curve (orange curve vs green curve in Figure 5.44), which now is closer to the reference curve than the filter-based critical PN curve for high FER and within 0.5 dB of said curve for low FER. This leads to the assumption that the frequency region around 40 kHz, which has not been changed for the IFFT-based generation method in the switch from critical to typical PN mask, is responsible for this deviation to the filter-based method. As the results of the previous section have shown, this frequency region is also problematic for the phase tracker that

was utilized in the previous section. Further investigations are necessary to determine how to best deal with the issues caused by these frequencies.

It is however noteworthy that the low frequencies, despite having the highest specified dBc/Hz values in the mask definitions, do not lead to as many problems due to the ability to track slowly moving changes fairly well. Figure 5.45 shows a comparison of FER curves for masks adjusted in several frequency ranges originating from the critical PN mask, which verifies this assumption. The exact modifications of the critical PN mask are given in Table 5.11. When only the 10 Hz and 100 Hz point are adjusted downwards by 3 dB, no notable improvement over the original critical PN mask can be observed. The best results are obtained when the 10 kHz and 100 kHz points are lowered by 5 dBc/Hz, which allows the PN-affected curve to stay within 1 dB of the reference curve to an FER of 10^{-4}.
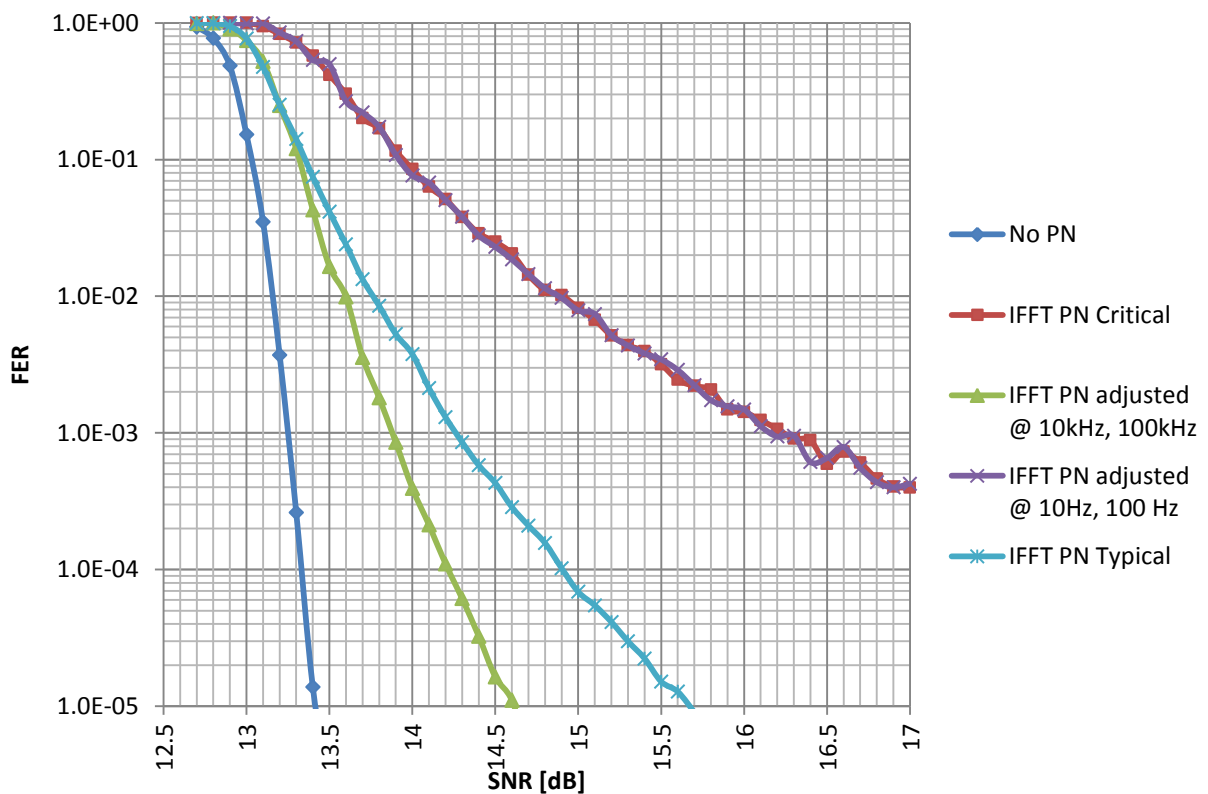
Figure 5.45: FER over SNR for 32-APSK ¾, critical PN with various adjustments for IFFT-based PN generation

Frequency	Critical Mask [dBc/Hz]	Adj. at 10 Hz, 100 Hz [dBc/Hz]	Adj. at 10 kHz, 100 kHz [dBc/Hz]	Typical Mask [dBc/Hz]
10 Hz	-25	-28	-25	-25
100 Hz	-25	-28	-25	-25
1 kHz	-50	-50	-50	-50
10 kHz	-73	-73	-78	-73
100 kHz	-83	-83	-83	-93
1 MHz	-103	-103	-103	-103
≥ 10 MHz	-114	-114	-114	-114

Table 5.11: Adjusted PN masks

Finally, a VSAT scenario is analyzed, where a lower baud rate of 1 MSymbol is assumed due to the fact that it is not a broadcast, but a return link application. The other parameters of the DVB-S2X system remain the same, but the VSAT P2 PN mask is utilized. Referring back to Section 2.3, it is apparent that the biggest differences between the critical and VSAT P2 PN masks lie in the frequency range from 100 Hz to 10 kHz.
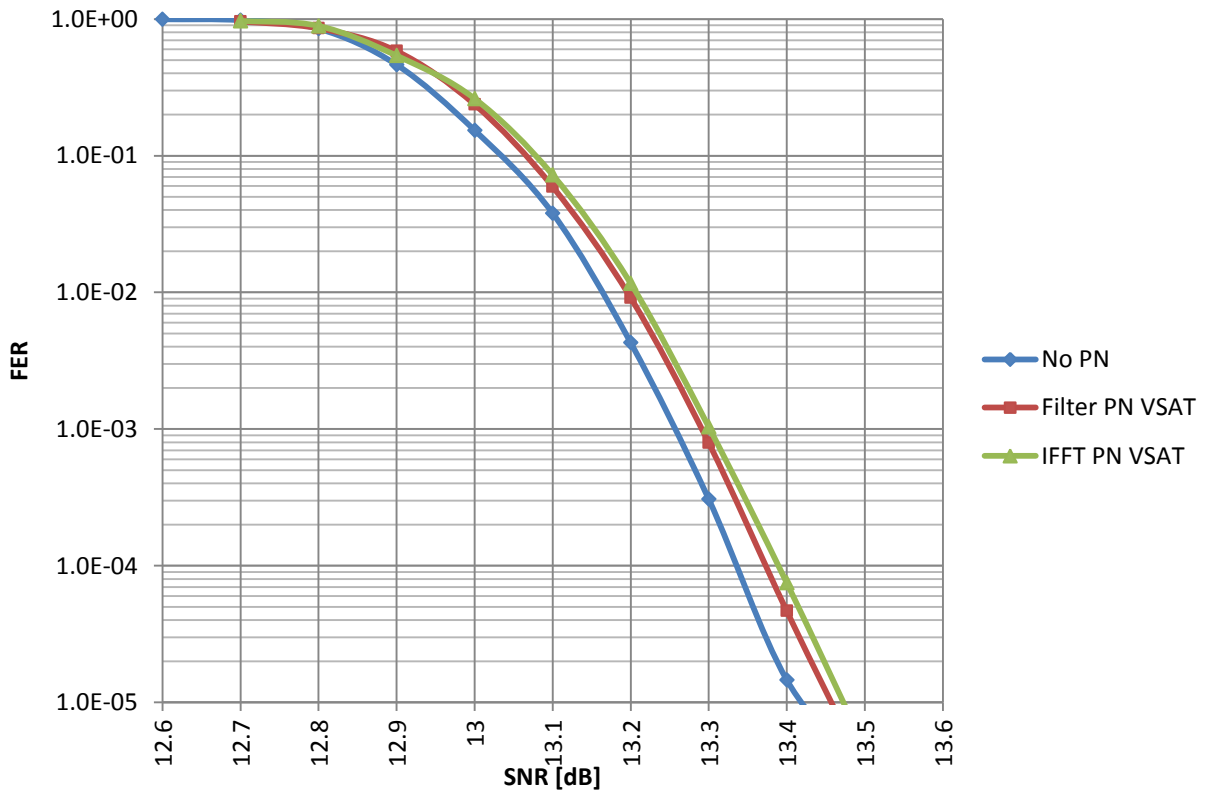
Figure 5.46: FER over SNR for 32-APSK ¾, VSAT P2 PN with different generation methods

Therefore, the significantly better performance of the VSAT P2 mask that can be deduced from Figure 5.46 can be explained by the lower specified phase noise power in those regions. It can be seen that the PN-affected curve is within 0.1 dB of the curve without impairment for all measured values down to an FER of $1 \cdot 10^{-5}$. Furthermore, the curves for the filter-based and the IFFT-based PN generation methods are virtually the same, with the IFFT-based curve being slightly closer to the reference for low SNR and slightly further away for higher SNR. The differences however are negligible especially in comparison to the previously measured values for the critical PN mask.

6.   Conclusion

Throughout the thesis, phase noise has been studied thoroughly. Two methods for the creation of phase noise samples in a digital simulation environment have been presented and the details of said simulation environment have been discussed. The IFFT-based phase noise method introduced in [5] has been extensively analyzed in the time- as well as frequency-domain for raw PN samples, a simple sine carrier waveform impaired by PN as well as DVB-S2X waveforms. The method has been shown to generate results of the desired quality, as well as to work with high throughput in conjunction with a proposed parallelization scheme.

In terms of the statistical analysis of raw PN samples, it has been verified that the resulting phase distribution is zero-mean Gaussian. It has also been shown that the PN process can be considered ergodic, as analyzing a sufficiently large number of samples from one realization of the process yields the same results as sampling a multitude of realizations of the PN process once and analyzing the statistical properties of those samples. This has however only been demonstrated based on the results from the analysis of multiple realizations of the process, so a more general conclusion towards the stationarity and ergodicity of the PN process cannot be drawn without further research.

The spectral analysis has been employed as a method to verify the integrity of the PN generation process, which has been shown to achieve the expected spectra for all analyzed PN masks. However, it could be verified that if PN affects the carrier frequency seriously, as was the case for the critical PN mask, a degeneration of performance has to be taken into account.

The IFFT-based PN generation method has then been compared in both computational complexity as well as result quality to the already implemented filter-based PN generation method. The results of said comparison have shown that the filter-based method works more efficiently by a factor of 2 if parallelization is disregarded. It allows for an efficient implementation in hardware such as a FPGA. However, it has been shown that the IFFT-based method offers an easier way to reproduce the PN mask accurately at the cost of additional computational complexity in terms of the FFT length. It has therefore been selected as the PN generation method for further analysis with modulated signals in the general framework of DVB-S2X, as computational complexity was shown to be not a major concern in the utilized simulation framework of the JOANNEUM RESEARCH simulator.

Using the same simulation framework, computationally more complex simulations were performed by taking into account modulated QPSK signals. Using a V&V phase tracker, the shape of the PN impairment after tracking has been presented in order to judge the influence of phase tracking and its performance. In the spectral domain, the lower frequencies up to a maximum frequency influenced by tracker noise bandwidth and sampling frequency have been shown to have their PN influence considerably reduced. Using additional AWGN impairment, a global optimum for the noise bandwidth has been identified in relation to the CSR, yielding the best performance operating point for the tracker. However, it has also been verified that the tracker cannot reliably reduce PN impairment for frequencies around 10 kHz and greater.

Furthermore, using a DVB-S2X simulation representing a DTH scenario, the FER rates of different modulation schemes and PN masks have been measured. It is shown that the critical PN mask leads to an approx. degradation of 0.1 dB for QPSK, but up to almost 2 dB for 32-APSK. Furthermore, due to the differences in the spectral analysis in the comparison between PN generation methods, it has been shown that the even worse performance of the IFFT-based method combined with the critical PN mask and 32-APSK is related to the unintentionally better

characteristics of the filter-based method due to filter cut-offs and up-sampling. Using an equivalent mask with the IFFT-based method produces to similar results, which leads to the introduction of the typical PN mask as a replacement for the critical one. Furthermore it has been shown that adjusting the mask in the 10 kHz to 100 kHz range yields the best performance improvements overall, which is consistent with the results from the phase tracker performance investigation.

Finally, a return link application using the VSAT P2 PN mask has been analyzed using the same simulation, where even for 32-APSK the results are much more promising, with a performance degradation due to phase noise of less than 0.1 dB.

Appendix: Additional Simulation Results

A.1 Statistical Analysis
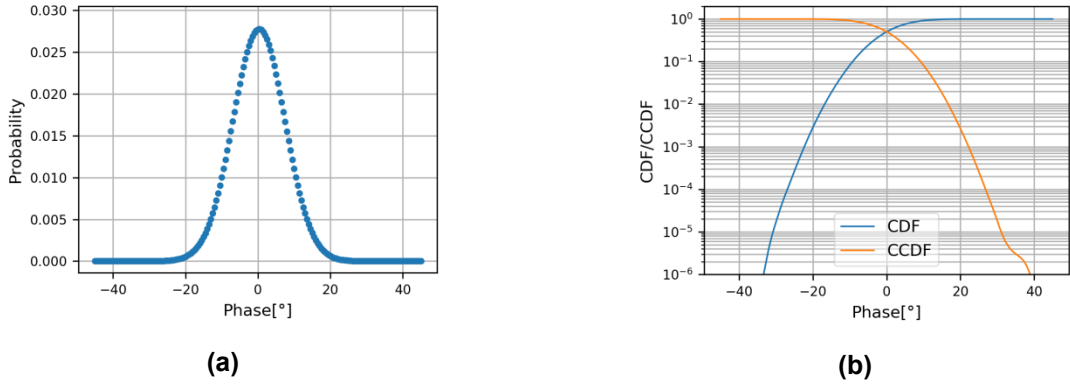
Figure A.1: (a) PMF and (b) CDF/CCDF of histogram analysis of VSAT P2 mask for f_s = 400 kHz ($2.6 \cdot 10^9$ samples)
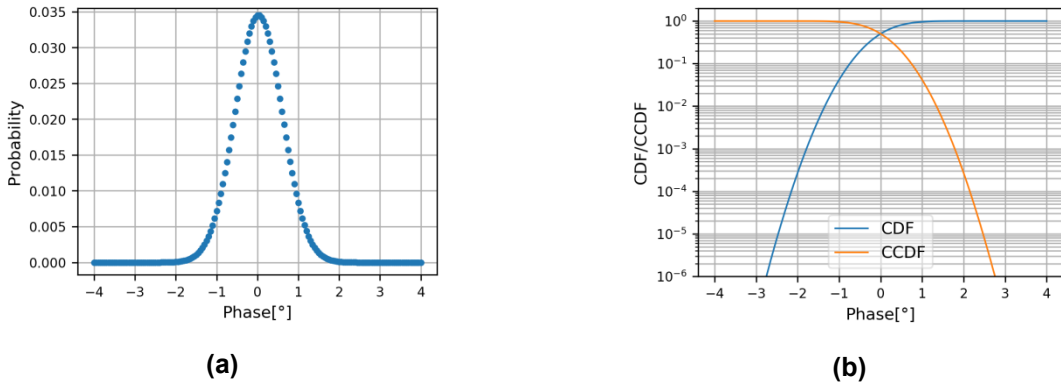
Figure A.2: (a) PMF and (b) CDF/CCDF of histogram analysis of transponder mask for f_s = 400 kHz ($2.6 \cdot 10^9$ samples)
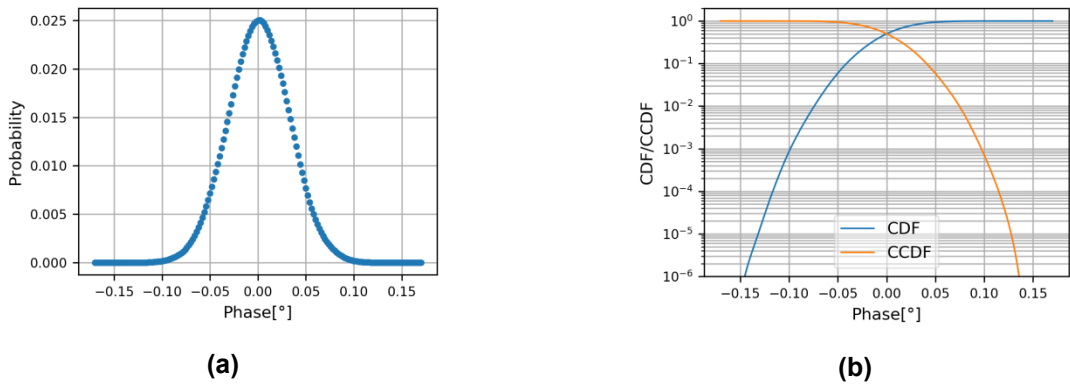
Figure A.3: (a) PMF and (b) CDF/CCDF of histogram analysis of differential mask for f_s = 400 kHz ($2.6 \cdot 10^9$ samples)

A.2 Random Walk

Transponder mask: $f_s = 400$ kHz: $\sigma = 0.58°$

(a)

(b)
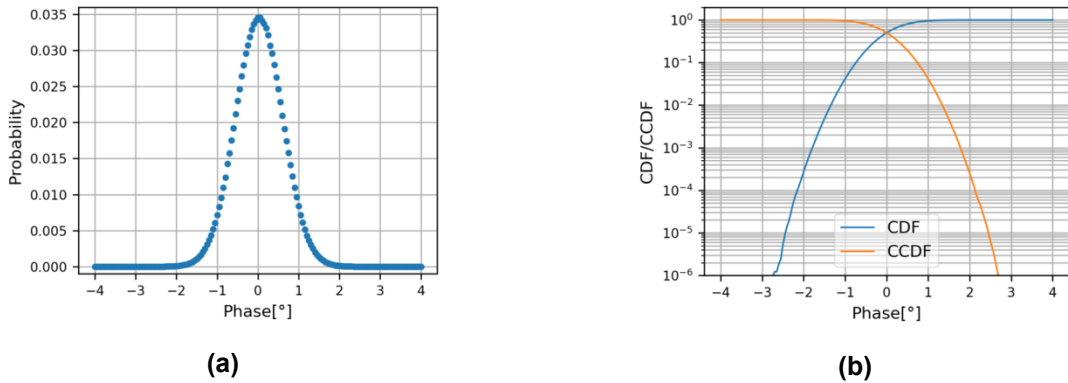
Figure A.4: (a) PMF and (b) CDF/CCDF of random walk analysis of transponder mask for f_s = 400 kHz (3.2·10^6 samples)

Transponder mask: $f_s = 40$ MHz: $\sigma = 0.61°$

(a)

(b)
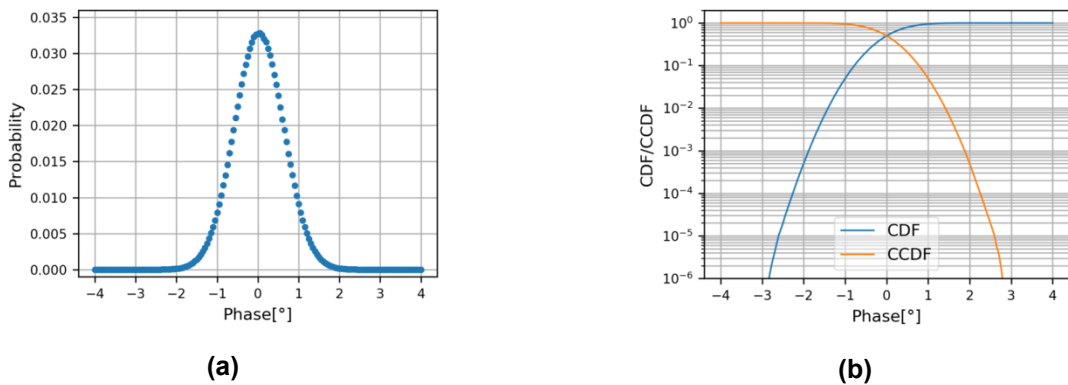
Figure A.5: (a) PMF and (b) CDF/CCDF of random walk analysis of transponder mask for f_s = 40 MHz (8.3·10^6 samples)

Differential mask: $f_s = 400$ kHz: $\sigma = 0.032°$

(a)

(b)
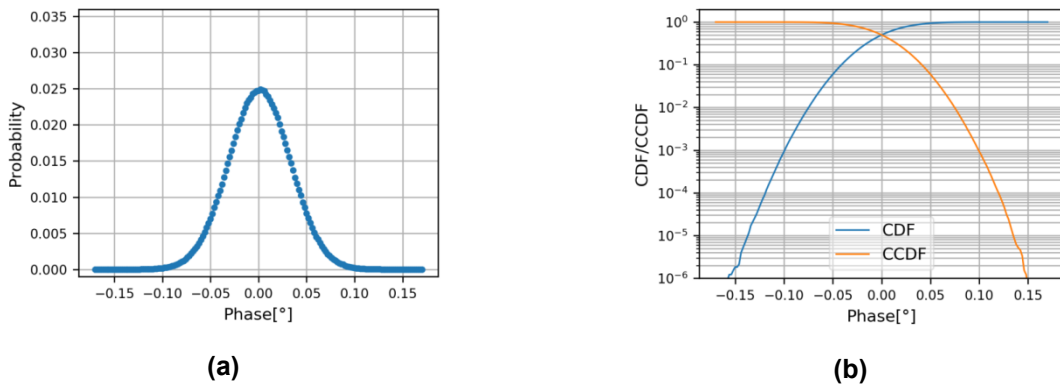
Figure A.6: (a) PMF and (b) CDF/CCDF of random walk analysis of differential mask for f_s = 400 kHz (3.2·10^6 samples)

Differential mask: $f_s = 4\,\mathrm{MHz}$: $\sigma = 0.033°$

(a)

(b)
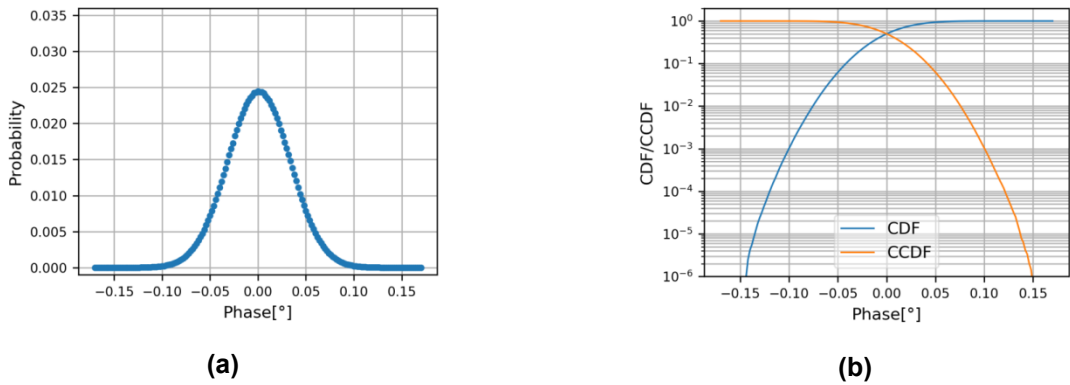
Figure A.7: (a) PMF and (b) CDF/CCDF of random walk analysis of differential mask for f_s = 4 MHz (8.3·10^6 samples)

A.3 Spectral Analysis
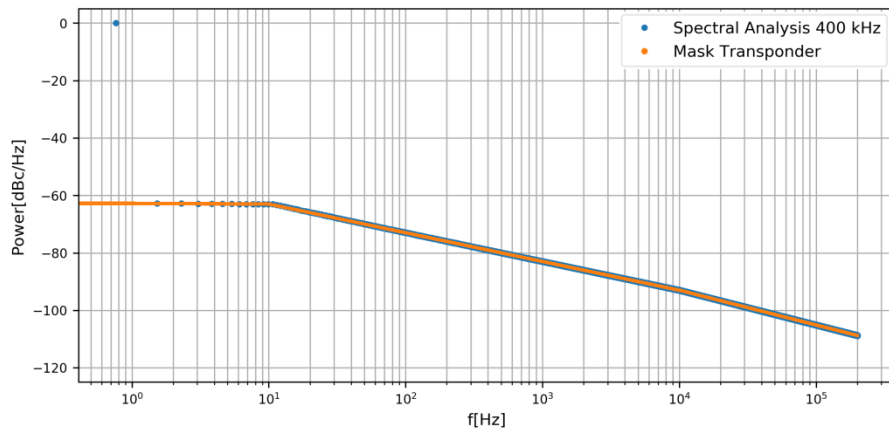
Figure A.8: Spectrum of PN-impaired sine wave for transponder mask, averaged over 50 000 iterations (blue), compared to the transponder PN mask (orange), f_s = 400 kHz, carrier bin at 0.76 Hz
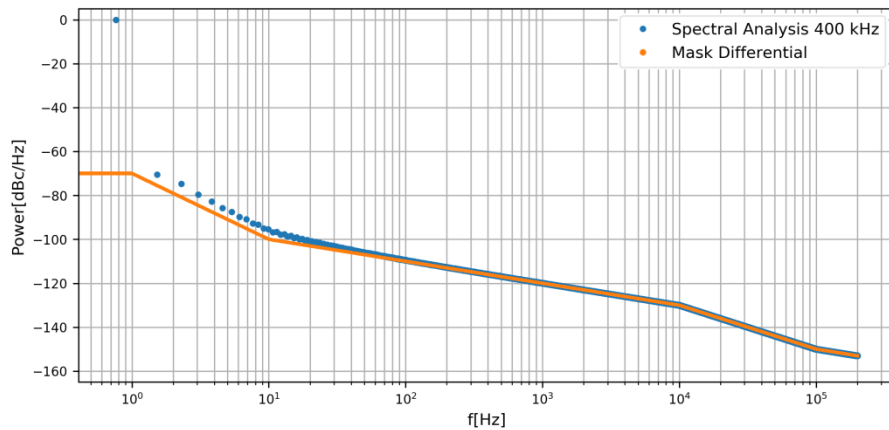
Figure A.9: Spectrum of PN-impaired sine wave for differential mask, averaged over 50 000 iterations (blue), compared to the differential PN mask (orange), f_s = 400 kHz, carrier bin at 0.76 Hz

VIII. References

[1] ETSI EN 302 307-2, "Digital Video Broadcasting (DVB); Second generation framing structure, channel coding and modulation systems for Broadcasting, Interactive Services, News Gathering and other broadband satellite applications; Part 2: DVB-S2 Extensions (DVB-S2X)," 2015.

[2] ETSI TR 102 376-2, "Digital Video Broadcasting (DVB); Implementation guidelines for the second generation system for Broadcasting, Interactive Services, News Gathering and other broadband satellite applications; Part 2: S2 Extensions (DVB-S2X)," 2015.

[3] A. L. Lance, W. D. Seal and F. Labaar, "Phase Noise and AM Noise Measurements in the Frequency Domain," *Infrared and Millimeter Waves,* vol. 11, pp. 239-289, 1984.

[4] A. Hajimiri and T. H. Lee, "A General Theory of Phase Noise in Electrical Oscillators," *IEEE Journal of Solid-State Circuits,* vol. 33, no. 2, pp. 179-194, 1998.

[5] A. Ginesi and S. Cioni, "Phase Noise Model in Computer Simulations," *ESA Technical Report,* 2013.

[6] D. Scherer, "Design Principles and Test Methods for Low Phase Noise RF and Microwave Sources," in *RF & Microwave Measurement Symposium and Exposition*, Hewlett Packard Seminar Notes: Radio Frequency And Microwave, 1978.

[7] G. Moschytz and M. Hofbauer, Adaptive Filter, Springer-Verlag Berlin Heidelberg, 2000.

[8] Intel®, "Integrated Performance Primitives: Developer Reference, Volume 1: Signal Processing," 2018.

[9] ETSI EN 302 307-1, "Digital Video Broadcasting (DVB); Second generation framing structure, channel coding and modulation systems for Broadcasting, Interactive Services, News Gathering and other broadband satellite applications; Part 1: DVB-S2," 2014.

[10] W. Gappmair, "Software Defined Radio; Part 2: Parameter Estimation and Synchronization in Digital Satellite Receivers," Lecture Manuscript, Graz University of Technology, 2017.

[11] E. Casini, R. De Gaudenzi and A. Ginesi, "DVB-S2 modem algorithms design and performance over typical satellite channels," *International Journal of Satellite Communications and Networking,* vol. 22, no. 3, pp. 281-318, 2004.

[12] H. Schlemmer and J. Ebert, "ARTES 8: Annex 1 to CCN1: Phase Noise," *JOANNEUM RESEARCH Internal Document,* 2014.

[13] E. Hogenauer, "An economical class of digital filters for decimation and interpolation," *IEEE Transactions on Acoustics Speech and Signal Processing,* vol. 29, no. 2, pp. 155 - 162, 1981.

[14] A. Ginesi, "DVB-S2X Channel Models," TM-S2 Channel Model Group, ESA, 2014.